Structure, Thermodynamics and Kinetics of Chemically Heterogeneous Interfaces

by

Jesus Pablo Palafox Hernandez

Submitted to the graduate degree program in Chemistry and the Graduate Faculty of the University of Kansas in partial fulfillment of the requirements for the degree of Doctor of Philosophy

Committee:

_____

Prof. Brian B. Laird, Chairperson

_____

Prof. Ward H. Thompson

_____

Prof. Krzysztof Kuczera

_____

Prof. Carey K. Johnson

_____

Prof. Aaron Scurto

Date defended: _____

The Dissertation Committee for Jesus Pablo Palafox Hernandez certifies that this is the approved version of the following dissertation:

Structure, Thermodynamics and Kinetics of Chemically Heterogeneous Interfaces

Committee:

Prof. Brian B. Laird, Chairperson

Prof. Ward H. Thompson

Prof. Krzysztof Kuczera

Prof. Carey K. Johnson

Prof. Aaron Scurto

Date approved: _____

Abstract

In this work we have used atomistic computer simulations to examine the structure, thermodynamics and transport properties, for two models of chemically heterogeneous interfaces: an ideal model (repulsive soft spheres against a potential wall), and a metal alloy interface (Cu-Pb). In both systems, interfacial prefreezing (crystal formation above the melting point of the fluid) was observed and this prefreezing was seen to promote heterogeneous nucleation, when the systems were cooled below the melting temperature.

In our study of inverse-power repulsive soft spheres, we found that the soft-sphere fluid exhibited prefreezing at the wall surface. Similar behavior was previously observed in hard-sphere fluids at hard wall [17, 18, 20], however, to our knowledge, this the first time that prefreezing is reported for soft spheres. The prediction of prefreezing is based on the calculation of interfacial free energies wall-crystal (γ_{wc}) and wall-fluid (γ_{wf}) using a variant of the cleaving wall method. With the calculated, γ_{wc} and γ_{wf} together with γ_{cf}, previously computed [79], the tendency to prefreeze was quantified by the wetting angle formed between the metastable crystal phase on the wall and the soft-sphere fluid. We found that all the closest packing orientations [(111) FCC and (110) BCC] developed prefreezing (complete wetting).

A detailed atomic-level characterization of the structure, energetics and transport properties of the planar Cu/Pb solid-liquid interface in equilibrium was performed at a several temperatures (625K and 750K) above the melting point of Pb and for two Cu crystal orientations [(111) and (100)]. Among the most relevant findings are that the Cu(100)/Pb interfaces presents surfaces alloying and the Cu(111)/Pb exhibits a prefreezing layer of Pb crystal. It was also observed that both interfaces have a nucleation

barrier that prevents heterogeneous nucleation and that the mechanisms by which each structure promotes heterogeneous nucleation are different.

Both models, the inverse-power soft spheres and the EAM Cu-Pb, showed the connection between atomistic behavior and prefreezing. The crystalline layer formed above the melting point of the fluids showed to be influential in heterogeneous nucleation in both cases. In this way, the study of basic properties shed new light on the atomistic underlying nature of macroscopic events, such as wetting and nucleation

To my family

Acknowledgments

This incredible journey has been possible due to my family and friends who have encouraged me. It all started at home with my parents, who always cared about my development as a person and as a productive human being. There is no way I can express my gratitude to my sister Caro and my brother Benjamin; I have some many great memories about our adventures.

There are many professors who believed in me, and without them I would not be here. I would like to thank especially to Professors Yolanda, Mike and Ogura, who started the interest of doing research during my undergraduate years. I am greatly thankful to the professors in "Celaya Tec." who taught me the wonders of hard work. I am especially grateful to Professor Mario Rivera who took me under his wing at KU. I have very special memories of time that I spent with professor Mark Asta and the CMSN crew, they really inspired me.

I have no words to express the gratitude that I have towards my doctoral advisor Professor Brian B. Laird. His incredible thirst of knowledge encouraged me to be a better researcher and overall a better person.

It is impossible not to thank all my friends who joined me in this journey. I am afraid to leave somebody out, so, I would only say: thanks for being there, I do sincerely appreciate your friendship and the great moments we spent together.

Finally, this dissertation has been possible due the love and care that my wife Josefina gave me. Thanks Josefina, these have been the best years of my life!.

Contents

List of Tables

List of Figures

Chapter 1

Introduction

Interfaces are part of our daily life, and interfacial processes govern such everyday phenomena as melting, crystallization and condensation. Reactions taking place at the interface are important in chemical and biological processes, such as heterogeneous catalysis and biochemical reactions at membranes, which are necessary for life. Despite our existing familiarity with them, the current understanding of interfaces is far from complete. Many of the atomistic details of the solid-liquid interface can be seen in a process as simple and useful as soldering, in which a low melting Sb/Pb alloy is used to bind a solid Cu, are still unknown. These are but just a few practical examples in which interfaces are present.

In this dissertation, a particular class of interface is studied: Chemically heterogeneous interfaces, which are defined as systems in which there is a sudden change in the composition at the interface formed by two phases in contact – a phase is region where the properties are homogeneous. The microscopic structure of chemically heterogeneous interfaces is important in a wide range of phenomena such as wetting, nucleation and crystal growth [1–5]. Experimental studies of interfaces between condensed phases

are rare and difficult [6–9] – most of them are descriptive in nature and provide few quantitative measurements. On the other hand, most computational efforts have been expended towards the understand of single component systems [10–16]. Studies on multicomponent systems have focused on nearly ideal models which form nearly ideal solutions, in which the compositional heterogeneity across the solid-liquid interface is not large or on systems in which the solid phase is modeled by a static wall. Examples include hard spheres against walls [17–20] [19], hard-sphere mixtures [21, 22], Lennard-Jones mixtures [23, 24] and nearly ideal metal alloys [25, 26].

An interesting feature of chemically heterogeneous systems are the structures formed at the interface, such as the surface alloying and prefreezing, which we report here. Prefreezing is the formation of an interfacial crystalline wetting layer above the melting point of the fluid. Many of such structures have been predicted only from simulation through the analysis of trajectories and density profiles, yielding qualitative statements on phenomena like wetting and heterogeneous nucleation [17, 18, 27]. Only a few simulation studies have focused on measuring thermodynamic properties that allowed a quantitative understanding of the energetics of prefreezing [19, 20, 28]. On the experimental side, this year, Kauffmann *et al.* [29] presented the first quantitative experimental studies measuring in-plane ordering (prefreezing) at an alumina-aluminum (Al_2O_3-Al) solid-liquid interface. Using high resolution transmission electron microscopy, Kauffmann *et al.* measured the position of the atoms in the region close to the interface, and they were able to see interfacial 2-d, see Fig. 1.1. Understanding the atomistic nature of this 2-d ordering at the interface is one of the primary themes of this dissertation.

In this work, we study the structure, thermodynamics and kinetics of two model classes of chemically heterogeneous interfaces using atomistic simulations: an inverse-

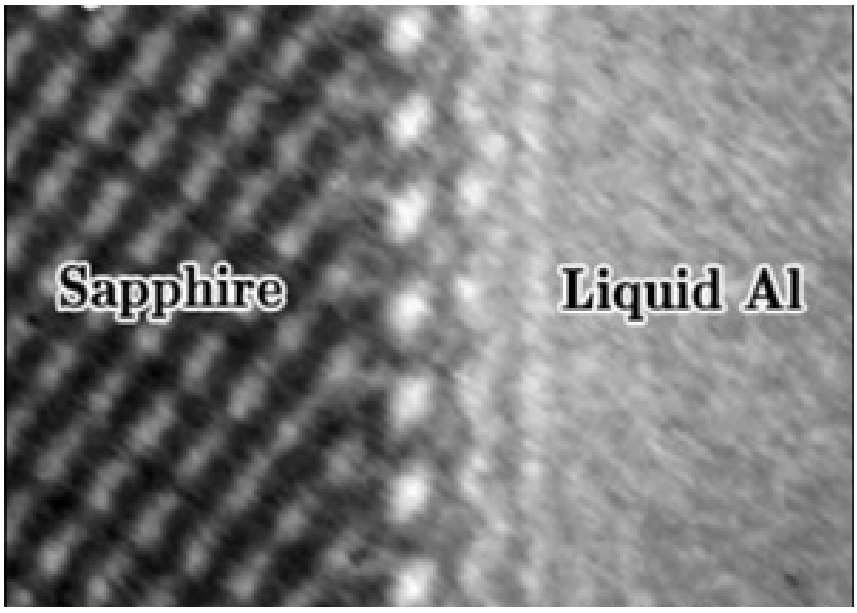

Figure 1.1: 2-d ordering of the Al_2O_3-Al solid-liquid interface, the darker atoms are the Al_2O_3 (sapphire) and the most clear atoms are the liquid Al. Figure reproduced from Reference [29].

power repulsive soft-sphere fluid at a wall and liquid Pb/crystal Cu interfaces. In the first case, using repulsive soft spheres against a structureless repulsive wall, the thermodynamics of formation of a prefreezing layer (crystalline structure above the melting point of a fluid) is studied. This work was motivated by the observation of prefreezing for a hard-sphere fluid at a flat structureless wall [17–20, 27, 28], in order to determine if prefreezing persists when the range of the potential is increased is unknown. Note that, this prefreezing layer could also be called a wetting layer, because a phase "a" (crystal for this case) stays in contact with phase "b" (wall) while another phase "c" (fluid) also tries stay on "b". In order to quantify of wetting, the interfacial energies (γ) involved – namely wall-fluid (γ_{wf}) and wall-crystal (γ_{wc}) –, are calculated to predict wetting angles. The cleaving-wall method (CWM) and the Gibbs-Cahn integration are used to determine the interfacial free energies. The interfacial free energies are then

used as inputs for Young's equation to calculated the wetting angle. This calculation is performed for several interactions ranges of the repulsion (softness of the sphere), to quantify the effect of repulsion in the wetting phenomena.

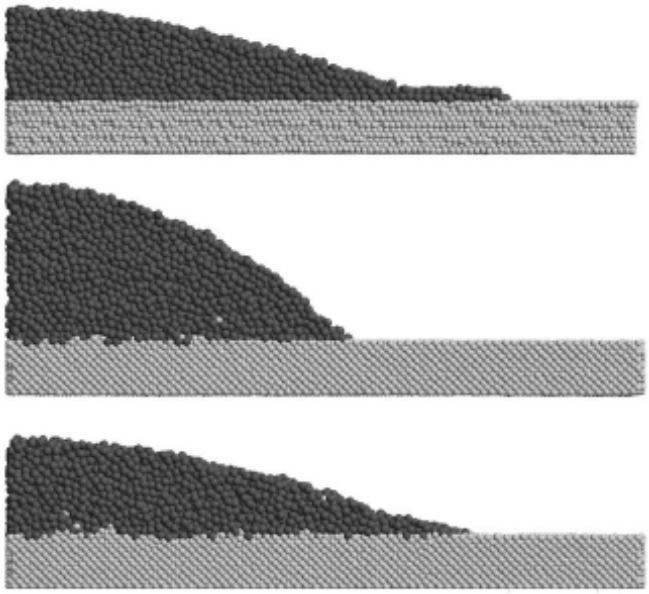

Figure 1.2: Configurations of Pb droplets spreading on a Cu substrate: Pb on (111) Cu after 0.5 ns (top), Pb on (100) Cu after 0.5 ns (medium) and 3.6 ns (bottom). A drastic difference on the spreading times is observed. Figure reproduced from Reference [30].

In the second part of this dissertation, the Cu-Pb crystal-solid interface is studied using an embedded atom method (EAM) to describe the interaction. This was motivated by a previous report by Webb *et al.* [30] describing anisotropic behavior in the spreading of Pb droplets on crystal Cu – (111) and (100) – substrates, see Fig.1.2. In this kinetic study, the times of the spreading of the droplets was reported, observing that the Pb droplet on Cu (111) substrate was well spread after 0.5 ns, whereas, the one on Cu (100) took almost 4.0 ns to achieve a similar extent of spreading. The authors commented little about the atomistic nature of the anisotropy reported, their comment

was a qualitative statement: the (111) spreading was promoted by a precursor film or "foot" [See Fig. 1.2 (top)], and this foot was not observed on the Cu (100) interface. The anisotropy reported by Webb *et al.* motived us to understand the role of the crystal orientation in the formation of interfacial structure and its consequences for crystal formation, which can give some understanding of the atomistic phenomena behind the orientational dependence of spreading. Here, we characterized the interface using density, stress and energy profiles in the direction normal to the interface. In this manner, the changes in these properties were analyzed, which shed new light on the interfacial structures encountered. Additionally, 2-d structure analysis, order parameter and dynamics are studied as well. To have a full picture of the events taking place at the interface, we also analyzed Pb nucleation and crystal growth on the two different Cu crystal orientation [(111) and (100)] using a series of cooling simulations.

In both reports Refs. [18] and [30], the presence of novel interfacial structures was observed. This motivated us to study the structure, thermodynamics and kinetics involved at the interface using atomistic simulations trying to connect these properties and give a quantitative atomistic explanation of prefreezing. Using a simple model potential such as the inverse power soft-sphere fluids, the thermodynamics of wetting are systematically analyzed varying the range of the repulsive interactions, and the Cu-Pb solid-liquid interface is used to characterize the structure, thermodynamics, and dynamics of a chemically heterogeneous interface.

The dissertation is divided into three parts: In the first part, an introduction to the methods of molecular simulations that are used in this work is presented. This part is divided into three chapters. In Chapter 2, the basic concepts of molecular simulations are discussed. Chapter 3 describes the methods for the calculation of multicomponent

phase diagrams, and Chapter 4 describes two methods for the calculation of interfacial free energy – the cleaving wall method (CWM) and the Gibbs-Cahn (GC) integration.

In Part II, the study of an inverse-power soft-sphere fluid against a repulsive wall is developed. In this part, Chapter 5 outlines the motivation and simulation details for these studies and in Chapter 6, the results are discussed. In Part III, the Cu-Pb solid-liquid interface is analyzed in two chapters: in Chapter 7, motivations, definitions and the system settings are presented, and in Chapter 8, the results for the Cu-Pb solid liquid interface are discussed. Finally, Chapter 9 summarizes the findings of this dissertation.

Part I

Computational methods

Chapter 2

Atomistic simulations

2.1 Introduction

Statistical thermodynamics connects the movement of atoms with macroscopic "measurable" quantities such as pressure, temperature or volume. A basic concept in statistical thermodynamics is that a probability function, called the partition function, can reproduce the distribution of atoms, and through mathematical manipulations, predict the physical properties of materials.

In the mid-twentieth century, scientists and engineers created the computer, arguably among the most useful inventions of this era. Since their arrival, computers have allowed humans to perform calculations that were previously impossible due to its length and complexity. With the advent of computers, the ideas of statistical mechanics took a completely new turn. Now the arduous and abstract concepts of atoms and space trajectories took the form of something more tangible – something that could be calculated accurately, plotted, and visualized. From the combination of computers and statical thermodynamics a new discipline emerged: molecular simulation. As a fur-

ther example, the work on this dissertation is possible due to this fusion of statistical thermodynamics and computers.

Currently, molecular simulation is a wide and burgeoning field that is used to study problems ranging from molecular transport phenomena in the human body [32] to complex theoretical calculations involving four dimensions [33]. Molecular simulations have the capacity to probe systems where experiments are difficult or inconvenient. This is mainly because in a computer the user can create conditions that in an experiment would be extremely costly or dangerous. For example, experimental studies of metals-melt interfaces are rare and they are mostly qualitative. Despite its strengths, simulations are not the solution to all problems: in fact, simulations must complement the experimental insight of the problem which is attempted to be solved.

Molecular simulations generally fall in two categories: molecular-dynamics (MD) simulations and Monte Carlo. MD is deterministic approach that solves the equations of motion describing ensemble distributions. The nature of MC is embedded in its name, it creates system distributions based on random numbers -at the time that the method was created, Monte Carlo was the biggest gambling center in the world. To have a better understanding of how these methods work, first we will introduce very basic concepts of statistical thermodynamics

2.2 Statistical averages

Here a brief conceptual review is presented, for a complete derivation of these concepts the reader referred to classic statistical mechanics textbooks [34–36]. The goal of a molecular simulation is to calculate the average of a measurable macroscopic property,

A, using a molecular system with N atoms, with three spatial coordinates q_i and three conjugate momenta p_i for each atom which form a $6N$-dimensional phase space. To calculate the property A, it is necessary to relate the time evolution of our space trajectories [$\Gamma(t)$] with A. In macroscopic terms, the property A_{obs} is measured experimentally by letting the system evolve for a period of time, with the time length determined by the property we want to measure. This A_{obs} is the time average of the quantity A, given mathematically by:

$$A_{obs} = \langle A \rangle_{time} = \langle A(\Gamma(t)) \rangle_{time} = \lim_{t_{obs} \to \infty} \frac{1}{t_{obs}} \int_0^{t_{obs}} A(\Gamma(t)) dt \tag{2.1}$$

From here, a way to proceed is to solve the equations of motion to get the time averages, which is what a MD simulation does. However, the averages can be taken out of configuration states rather than time, were the collection of all possible configurations is called ensemble. When the average is performed over configurations, this is called an ensemble average:

$$A_{obs} = \langle A \rangle_{ens} = \frac{1}{t_{obs}} \sum_{t=1}^{t_{obs}} A(\Gamma(t)) \tag{2.2}$$

Here the task is generate configurations distributed according to the appropiate distribution, which is the approach followed by a Monte Carlo simulation. These two kind of averages, time and ensemble, are equivalent if teh system is ergodic on the time scale of the experiment. A consequence of the ergodic hypothesis is that from a stationary random process, a large number of observations made on a single system at $\mathcal{N}$ arbitrary periods of time have the same statistical properties as observing $\mathcal{N}$ arbitrary chosen systems at the time from an ensemble of similar systems. The choice of how to do the average depends on the type of problem to be solved. If the problem is to

measure a property related to the time evolution of the system, for example diffusion constant, MD simulations are preferred. In cases were configurations are difficult to access because they are less probable, MC simulations with special sampling techniques (umbrella sampling [36]) are suggested.

It is necessary to impose some restrictions on the system under study, these restriction reflect the physical constraints upon the system. For example, if the total number of particles N, volume V and energy E constant are chosen to be constant, the configurations taken out of this kind of system are called microcanonical ensemble (NVE). Similarly, following the proper physical derivation several kind of ensembles can be constructed to study the conditions closer to the ones present in the phenomenon of interest. Thus we have the canonical ensemble NVT which has N, V and temperature T constant, the isothermal-isobaric NPT with N, pressure P and temperature constant. Once the particular ensemble is chosen, we can calculate the properties of interest using the machinery of statistical thermodynamics.

2.3 Molecular dynamics

Here, the fundamentals aspects of MD [37–39] are described. The first molecular dynamic simulation was performed by Alder and Wainwright [40]. This simulation was done using hard spheres, which is the simplest model to predict the behavior of a liquid. MD methods are particularly useful when we want to calculate trajectory dependent functions such as mean square displacements and time correlation functions. MD simulation use motions equations to describe the movement of the atoms or molecules, in the next subsection a brief introduction to Hamiltonian dynamics is presented.

2.3.1 Hamiltonian dynamics

At the core of the partition function lies the Hamiltonian, a function that states mathematically the energy relationships of the system [41]. The Hamiltonian is used to generated the equations of motion specific for the system. The equations of motion are extremely important because these equations generate the configurations in our system, and from the configuration averages the macroscopic properties are calculated. A classical Hamiltonian is expressed as:

$$H = K + U \tag{2.3}$$

The Hamiltonian H contains: K, the term containing the information regarding the kinetic energy, and U which describes the potential energy. Assuming that our system behaves classically (Newtonian), we can write K as a function only dependent of the momentum ($\vec{p}$) of the atoms or molecules and U as a potential energy, which is function only of the positions $\vec{q}$ of the N particles. Rewriting H, we have:

$$H = \sum_{i=1}^{N} \frac{p_i^2}{2m_i} + U(\vec{q}) \tag{2.4}$$

The Hamiltonian equations of motion are:

$$\frac{dq_i}{dt} = \frac{\partial H(\vec{p})}{\partial p_i} \tag{2.5}$$

$$\frac{dp_i}{dt} = -\frac{\partial H(\vec{q})}{\partial q_i} \tag{2.6}$$

For full derivation of the previous equations please see Ref. [41]. Substituting Eq. 2.15 in the previous equations, we obtain

$$\frac{dq_i}{dt} = \frac{p_i}{m_i} \tag{2.7}$$

$$\frac{dp_i}{dt} = -\nabla U = f_i \tag{2.8}$$

Once a function for the potential energy is specified, the equations of motion can be solved. Having the appropriate potential function is crucial to properly reproduce the physical situation of interest. A number of functions describing the interactions have been created, among the simplest cases are hard spheres, which behave similar to billiard balls with elastic collisions and no friction, the potential is infinity when they are in contact or zero otherwise, square-well potentials, soft spheres and more realistic ones like embedded atom model (EAM) trying to emulate the metal interactions. For example, the EAM is a pair-functionals potential [42], which contain a term describing pairwise interactions and a functional term describing the potential energy of the atoms in the surroundings. Pair-functional schemes have been very successful for metallic systems. For the EAM formalism the potential energy of the system as a function is:

$$U(q) = \sum_i (\rho_{h,i}) + \frac{1}{2} \sum_{i,j} \Phi(q_{ij}) \tag{2.9}$$

where q_{ij} is the interatomic distance between atoms i and j, Φ is a pair interaction, F_i is the energy required to embed atom i into the background electron density ρ. In equation 2.9 ρ_{hi} is the host electron density at atom i due to the remaining atoms of the systemm which is given by:

$$\rho_{h,i} = \sum_{j \neq i} \rho_i^a(q_{ij}) \tag{2.10}$$

where $\rho_j^a(q_{ij})$ is the electron density due to atom j. For details on the form of the functional and parameters, please see references [42–45]. The Cu-Pb potential used in this thesis is part of the standard potentials included in the code LAMMPS developed by Sandia laboratories (http://lammps.sandia.gov/). Additonal EAM can be found in the NIST interatomic potentials repository project database (http://www.ctcms.nist.gov/potentials).

Note that, the choice of the potential is extremely important because it specifies the equations of motion and from there the configurations are generated. In this work, two potential models are used, inverse-power soft spheres in Part II and an EAM for Cu/Pb in part III. In the next subsection, two kinds of MD methods are briefly discussed.

2.3.2 Constant energy molecular dynamics (NVE)

The main task in a MD simulation is to map the evolution of the trajectories of our system:

$$\{q_i(0), p_i(0)\} \xrightarrow{t} \{q_i(t), p_i(t)\} \tag{2.11}$$

In order to perform this operation, a model for the potential energy in the Hamiltonian is required:

$$U(\{q_i\}; i = i, ...N) \tag{2.12}$$

Using Hamilton's formalism the energy (E) of the system is preserved at constant number of particles (N) and volume (V). The equations of motion are derived from the Hamiltonian once the potential energy is specified. To integrate the equations of motion to determine the evolution of the system, one must calculate the forces (F_i) acting on each particule from the potential energy. So, the next step is to find a numerical integration scheme to solve these equations. For molecular simulations, the velocity Verlet [38] scheme is among the most common and efficient integrators. The integra-

tion scheme is as follows:

$$q_i(t+\Delta t) = q_i(t) + \Delta t v_i(t) + \frac{1}{2}\Delta t^2 \frac{F_i(t)}{m_i} \tag{2.13}$$

$$v_i(t+\Delta t) = v_i(t) + \frac{1}{2}\Delta t[\frac{F_i(t)}{m_i} + \frac{F_i(t+\Delta t)}{m_i}] \tag{2.14}$$

The Verlet algorithm is derived from a Taylor expansion rearranged in such a way that the positions $\{q_i\}$ and velocities $\{v_i\}$ can be predicted at a future time $t + \Delta t$. Here the time step Δt is extremely important because is has to be big enough to allow the simulation to run in a reasonable time but small enough to ensure that the simulation remains stable.

Summarizing, in a MD simulation one has to select a model for the potential energy, type of ensemble (thermodynamic constrains), find the equations of motion and then solve them numerically.

2.3.3 Constant temperature molecular dynamics (NVT)

In order to perform constant molecular dynamics (NVT), several methods have been developed [46–49]. Particularly useful methods are extended system methods based on the extended Hamiltonian of Nosé. In this scheme, the phase space is modified with the introduction of an auxiliary variable s and its conjugate momentum π (with "mass" Q). The original Nosé extended Hamiltonian is:

$$H_{Nosé} = \sum \frac{\tilde{p_i}^2}{2m_i s^2} + U(q_i) + \frac{\pi}{2Q} + g k_B T \ln s \tag{2.15}$$

where $\tilde{p}_i$ is the Nosé momentum conjugate to the position q_i which is related to the real momentum, p_i, by $p_i = \tilde{p}_i/s$. The parameter g is equal to $N_f + 1$, where N_f is the

number of degrees of freedom of the system. In this scheme, the generation of phase space configurations distributed in the canonical ensemble (NVT) is accomplished by a dynamical rescaling of time [49]. The real time t is realted to Nosé time τ by the transformation $\frac{d\tau}{dt} = s$. This transformation gives the following Nosé equations of motion:

$$\frac{dq}{d\tau} = \frac{\tilde{p}_i}{m_i s^2}, \ \frac{ds}{d\tau} = \frac{\pi}{Q} \tag{2.16}$$

$$\frac{d\tilde{p}_i}{d\tau} = -\frac{\partial U(q_i)}{\partial q_i}, \ \frac{d\pi}{d\tau} = \sum \frac{\tilde{p_i}^2}{2m_i s^3} - \frac{g k_B T}{s} \tag{2.17}$$

Because most integration methods utilize a fixed time step, this transformation will generate an uneven distribution of points in real time, which in cumbersome for the calculation of system averages. By applying time and coordinate transformations to Nosé equations of motion, Hoover [50], solved this issue. This modification gives the so-called the Nosé-Hoover (NH) method, and the transformations are

$$\eta = \ln s; \ \xi = \dot{\eta} \tag{2.18}$$

which yields the Nosé-Hoover the equations of motion:

$$\dot{q}_i = \frac{p_i}{m_i}, \ \dot{p} = -\frac{\partial U(q_i)}{\partial q_i} - p_i \xi \tag{2.19}$$

$$\dot{\eta} = \xi, \ \dot{\xi} = \frac{1}{Q}\left(\sum_i \frac{p_i^2}{m_i} - gkT\right) \tag{2.20}$$

These equations of motion can be shown to generate configurations distributed according a canonical distribution. Because the NH is non-Hamiltonian in structure, it prevents the use of symplectic integration schemes (they conserve the phase-space volume). It has been shown that symplectic methods have better long-term stability that

non-symplectic methods with higher local errors [51]. A modification done by Bond *et al.* [52] corrected this by modifying the Hamiltonian directly using a Poincaré time transformation, as follows:

$$H_{NP} = s(H_{Nosé} - H_0) \tag{2.21}$$

where H_0 is the value of $H_{Nosé}$ at $t = 0$. Combining Eq. 2.15 and 2.21, the Nosé-Poincaré (NP) Hamiltonian is obtained:

$$H_{NP} = s\left(\sum_i \frac{\tilde{p}_i^2}{2m_i s^2} + U(q) + \frac{\pi^2}{2Q} + gk_BT\ln s - H_0\right) \tag{2.22}$$

which gives the NP equations of motion:

$$\dot{q} = \frac{\tilde{p}}{m_i}s,\ \dot{s} = \frac{s\pi}{Q}, \tag{2.23}$$

$$\dot{\tilde{p}} = -s\frac{\partial U(q)}{\partial q_i},\ \dot{\pi} = \sum_i \frac{p_i^2}{m_i s^2} - \Delta H \tag{2.24}$$

$$\Delta H = \sum_i \frac{\tilde{p}_i^2}{2m_i s^2} + U(q) + \frac{\pi^2}{2Q} + gk_BT\ln s - H_0 \tag{2.25}$$

The NP equation of motion not only generate a correct canonical distribution but also preserve the phase space volume, this Hamiltonian is time reversible. Note that, the symplectic method are more stables than non-symplectic ones as described before.

For constant pressure molecular dynamics (NPT) simulation, a similar procedure is applied by further extending the phase space of the Hamiltonian to include the volume V and its conjugate momentum π_V. The reader is referred to Ref. [47] and [38] for the details of the derivation and implementation of NPT methods.

2.4 Monte Carlo simulations

Monte Carlo (MC) simulations were the first kind of molecular simulations performed [53]. The method uses random numbers to generate relevant properties, through sampling techniques. A simple example to understand MC is the calculation of π through a hit and miss experiment. Imagine a circle inscribed in a square, and darts are thrown randomly at them. The number of darts hitting inside the circle (x) and the total of darts thrown (y) are counted. Given that the ratio of the circle area to the square is $\pi/4$, π can be calculated by:

$$\frac{circle\ area}{square\ area} = \frac{\pi}{4} = \frac{x}{y} \tag{2.26}$$

To improve the sampling in this calculation, a mean sampling method that includes a probability density function can be used [37, 38]. Suppose that, we desire to integrate

$$F = \int_{x_1}^{x_2} dx \cdot f(x) \tag{2.27}$$

using probability density functions $\rho(x)$, Eq. 2.27 can be rewriten as:

$$F = \int_{x_1}^{x_2} dx \left(\frac{f(x)}{\rho(x)}\right) \rho(x) \tag{2.28}$$

rewriting these equations using the definition of average value:

$$F = \left\langle \frac{f(\xi)}{\rho(\xi)} \right\rangle = \frac{1}{N} \sum_{i=1}^{N} \frac{f(\xi_i)}{\rho(\xi_i)} \tag{2.29}$$

where ξ is a random number in between the range x_1 and x_2, N is the number of trials. This relatively simple procedure can be applied to calculate averages for a particular partition function of a given ensemble. The application of this methodology reduces significantly the time involved in calculating the averages. If these averages would be

calculated using standard numerical quadrature - like Simpson's rule - the number of integrals would be in the order on $(integration\ steps)^{3N}$. Suppose that we would like to integrate 100 bins for a hundred particles then the total of integrals would be 100^{300}, which is an impossible calculation.

The averages of interest have the form:

$$\langle A \rangle = \frac{\int dq \cdot e^{-\beta\Phi(q)} A(q)}{\int dq \cdot e^{-\beta\Phi(q)}} \tag{2.30}$$

This is averaging is a non trivial calculation. However, following a similar procedure like the one used in the previous paragraph, the average calculation could be reduced to a sum over N independent and uncorrelated configurations:

$$\langle A \rangle = \frac{1}{N} \sum_{k=1}^{M} A_k \tag{2.31}$$

The MC method should use proper sampling techniques that ensure the sampling over the regions of configuration space that are relevant to the problem of interest. To accomplish proper sampling, MC generally use a Markov chain which is a sequence of events that satisfies the following conditions: a) each successive configuration depends only upon the previous, and b) each configuration belongs to an ensemble representative of the distribution of interests. Metropolis *et al.* [53] applied these ideas to molecular simulation and the authors generated the Metropolis-Monte-Carlo methodology:

1. Compute the system energy E_n
2. Select at random a particle.
3. Displace by δx, this will move the atom a random generating a new configuration.
4. If the new configuration decreases the energy $E_{n+1}$of the system the movement

is accepted, otherwise compare the next probabilistic factor:

- if $e^{-\beta E_{n+1}} \leq$ random number, ξ, accept the movement
- if $e^{-\beta E_{n+1}} > \xi$ reject the movement

5. Repeat

Here we have oversimplified the sampling problem, for further details the reader is referred to Ref. [37, 38]. Using the Metropolis algorithm is possible to get accurate results, and it has been proven an excellent way to perform molecular simulations.

2.4.1 Semigrand MC

Due to its ability to explore phase equilibrium, MC simulations using the semigrand ensemble are used in this thesis. The semigrand ensemble was developed by Kofke and Grandt [54] to be used for phase diagram calculations as an alternative to the Gibbs ensemble [38,55]. The idea behind semigrand is to allow a particle change of type to facilitate chemical equilibrium. In the semigrand simulations the total number of particles is kept constant at constant pressure and temperature while the difference in chemical potential ($\Delta\mu = \mu_2 - \mu_1$) is constant, it can be seen as the "constant $Delta\mu PT$ ensemble". Thus, there are 3 types of displacements for the generation of configurations: position, changes in the volume of the simulation box and exchange of particle type. Kofke and Grant [54] proposed the following algorithm to perform the simulation:

1. Perform a perturbation; choose one or a combination of
   (a) Change the box volume.
   (b) Displace an atom selected at random.
   (c) Change the type of an atom selected at random.

2. Accept the new configuration if A increases the probability e^{-A}, where:

$$A = +\beta(U_{new} - U_{old}) + \beta P(V_{new} - V_{old}) - \beta(\Delta\mu_{new} - \Delta\mu_{old}) - N \ln \frac{V_{new}}{V_{old}}$$

3. Record the configurational properties and repeat

This is the numerical "recipe" to perform semigrand MC for the full derivation see Refs. [38, 54].

So far we have presented the very basic ideas behind molecular simulations. In the next chapter we will apply some of these methodologies while reviewing some methods used to calculate interfacial free energies.

Chapter 3

Calculation of multi-component phase-diagrams

3.1 Introduction

A phase diagram is a map of the thermodynamic space showing the conditions under which two or more phases coexist. A phase is a region where the properties of the system are homogeneous. Phase diagrams are important in studies of equilibrium interfaces because they give the equilibrium thermodynamic conditions for the system of interest. The task of generating phase diagrams for multicomponent systems, such those considered here, either experimentally or by simulation, is not trivial. In this chapter two molecular simulation methods for determining the phase diagram binary (two-component) systems are presented:

- The "common tangent construction" (CTC) [23, 26, 45]
- "Gibbs-Duhem integration" [56–60]

In Section 3, the application of these techniques to the study of the Cu-Pb crystal-liquid interface will be discussed.

3.2 Common tangent construction

The equilibrium conditions for a system containing multiple coexisting phases are *mechanical* (equal pressures in each phase), *thermal* (equal temperatures) and *chemical* (equal chemical potentials, $\Delta\mu$). The common tangent method directly uses these conditions to determine the phase diagram of multicomponent systems. The central idea of this methodology is to determine the Gibbs energies of the liquid and solid phase as a function of the mole fraction of one of the components using a thermodynamic integration of $\Delta\mu(x_2)$ at constant pressure (P) and temperature (T). A standard implementation of the CTC for a binary crystal-melt system involves the following steps:

1. Chose one component as a reference.
2. Calculate the melting point (T_m) for the pure reference species.
3. Compute the difference in Gibbs energy between the liquid and solid phases for the reference species as a function of temperature using NPT simulations, see Chapter 2, from T_m to the temperature under study.
4. Calculate the Gibbs energy of each phase as a function of the mole fraction of the reference species employing semi-grand Monte Carlo simulation ensemble, see Chapter 2.
5. Plot the obtained Gibbs energies of the binary system and trace a common tangent between the solid and liquid curve to find the equilibrium composition at a

that particular temperature. Alternatively, calculate the grand potential for both phases, plot them and find the intersection.

If steps 3 to 5 are repeated while changing the temperature, a phase diagram of temperature versus composition can be obtained. In the remainder of this section, a derivation of the required equations using the notation for Cu as the reference component for the melting point and Pb as the reference for $\Delta\mu(x_{Pb}, T)$ is presented.

The Gibbs energy values are based on a relative scale, this means that the energies are measured relative to a reference state, which must be specified in a manner that facilitates the calculation. A convenient choice for this is the melting point of the pure system of one of the components, because the Gibbs energies of the pure solid and pure liquid are equal at this point. In this way, the changes in Gibbs energies measured relative to this point.

The second step in the calculation requires the determination of the reference component for the melting point (T_m) Cu is chosen for this calculation. A general phenomenological method to calculate melting points for binary alloys is presented by Morris *et al.* [61]. This method consists of constructing a crystal-melt system and performing NPT simulations to measure the mobility of the interface [45, 62, 63] until equilibrium is reached whit stress-free bulk phases [61, 64, 65]. Alternatively, the melting point can be obtained by heating several bulk solids until they melt and vice versa cooling melts down until the solidify, these is done using NVT simulations. Because of superheating and supercooling, this method will give a large uncertainty in the equilibrium melting point. Note that, the knowledge of the Cu melting point, serves as a reference in the construction of the Gibbs energy curves. Once the melting point is known, the next step is to compute the Gibbs energy difference between the liquid and solid phase for the

pure reference component, Cu in this case, as a function of temperature. This difference will serve as a reference in the construction of the liquid and solid Gibbs curves for the mixture. The Gibbs-Helmholtz (GH) equation [23] is employed to calculate the difference in enthalpies because GH describes the change of Gibbs energy per particle with respect to temperature:

$$\left[\frac{\partial(G/NT)}{\partial T}\right]_P = \left[\frac{\partial(\mu/T)}{\partial T}\right]_P = -\frac{H}{T^2} \tag{3.1}$$

Here μ is the Gibbs energy for a particle single component ($\mu = G/N$) – or chemical potential of that species for mixtures – and H is enthalpy. By integrating Eq. 3.1 at fixed pressure, it is possible to obtain the difference between the Gibbs energy of the solid and liquid phases at a given temperature, if the melting point of Cu is known:

$$\frac{\mu^S - \mu^L}{T} = \int_T^{T_M} \frac{H^S(T') - H^L(T')}{T'^2} dT' \tag{3.2}$$

where superscripts S and L denote solid and liquid, respectively. In practice, all the quantities required in equation 3.2 are computed with a series of NPT simulations of pure Cu at several temperatures. The temperature is varied from the Cu melting point to the temperature where the composition is desired. In this calculation we set the difference of the Gibbs energies of pure copper at the melting point as the reference point in the construction of the Gibbs energy curves as a function of composition for the system.

The next step in the calculation is to construct Gibbs energy curves for the liquid and solid phases as a functions of composition using a series of semi-grand MC simulations, see Chapter 2. Defining the difference in chemical potentials as $\Delta\mu(x_{Pb}, T) = \mu_{Pb} -$

μ_{Cu}, the changes in Gibbs energy and phase composition are related by:

$$\left(\frac{\partial \Delta G}{\partial x_{Pb}}\right)_{P,T} = \Delta\mu(x_{Pb}, T) \tag{3.3}$$

This relationship requires knowledge of the chemical potential difference - in practice for a semi-grand MC simulation this is an input. It is convenient to express the difference in chemical potentials by two terms: an ideal part (which is known exactly) and an excess part:

$$\begin{aligned} \Delta\mu(x_{Pb}, T) &= \mu_{id} + \mu_{ex} & (3.4)\\ &= k_B T \ln\left(\frac{x_{Pb}}{1 - x_{Pb}}\right) + \mu_{ex}(x_{Pb,T}) & (3.5) \end{aligned}$$

One way to proceed is to fit the excess part to a polynomial with n terms and coefficients (A_i) [45]. Then, the difference in chemical potentials as a function of Pb mole fraction and temperature [$\Delta\mu(x_{Pb}, T)$] is

$$\Delta\mu(x_{Pb}, T) = k_B T \ln\left(\frac{x_{Pb}}{1 - x_{Pb}}\right) + \sum_{i=0}^{n} A_i(T) x_{Pb}^i \tag{3.6}$$

At this point, a series of semi-grand MC simulations are performed to obtain the Pb mole fraction corresponding set of $\Delta\mu(x_{Pb})$, T, P per each phase. The excess part is obtained from subtracting the ideal term from $\Delta\mu$. An example of the contributions to $\Delta\mu$, separated into the ideal and excess components for a binary Lennard-Jones [23] system, can be seen in Fig. 3.1. Integrating Eq 3.6 and 3.3, the Gibbs energy for the solid or the liquid can be obtained using:

$$\begin{aligned} G(T, x_{Pb}) = G(T, x_{Pb} = 0) + k_b T[x_{Pb} \ln x_{Pb} + \\ (1 - x_{Pb}) \ln(1 - x_{Pb})] + \textstyle\sum_{i=0}^{n} \frac{A_i x_{Pb}^i}{i+1} \end{aligned} \tag{3.7}$$

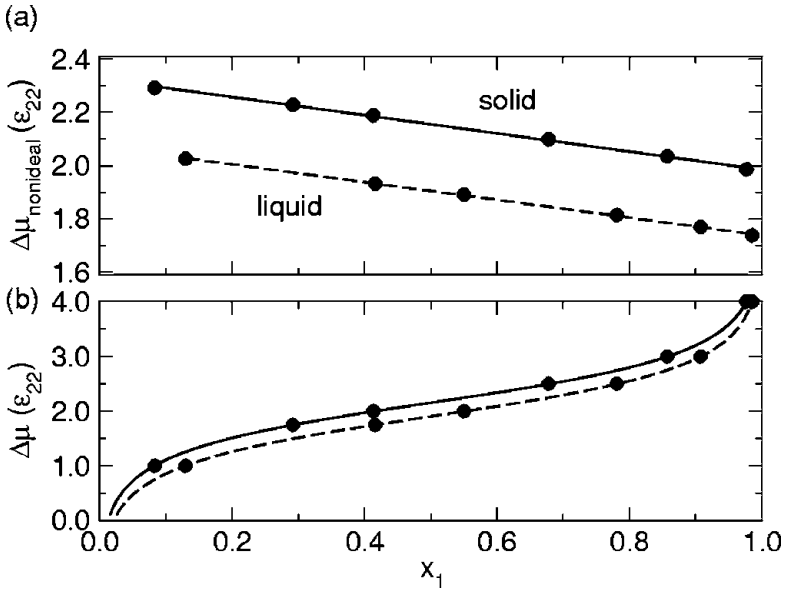

Figure 3.1: Difference in chemical potential contributions for an ideal Lennard Jones system, Chemical potential: a) excess part, b) ideal contribution. Figure reprinted from reference [23].

The Gibbs energies in Eq. 3.2 are measured with respect to $G(T, x_{Pb} = 0)$, which has a reference point the difference in free energies computed in Eq. 3.2. In practice, $G(T, x_{Pb} = 0)$ is set to zero for the liquid phase and $G(T, x_{Pb} = 0)$ for the solid is equal to the Gibbs energy difference (computed using equation 3.2). Once the Gibbs energy curves for the liquid and solid are plotted, a common tangent is traced between the two curves to fulfill the equilibrium requirement of equal $\Delta\mu$ at fix T and P, and the equilibrium compositions are given by intercept of the tangent and the correspondent Gibbs curve, see Fig 3.2. Instead of doing the fitting of the energies, equation 3.6 can be integrated numerically using trapezoid or Simpson's quadrature. Using a numerical quadrature facilitates the error propagation to the final composition at this conditions.

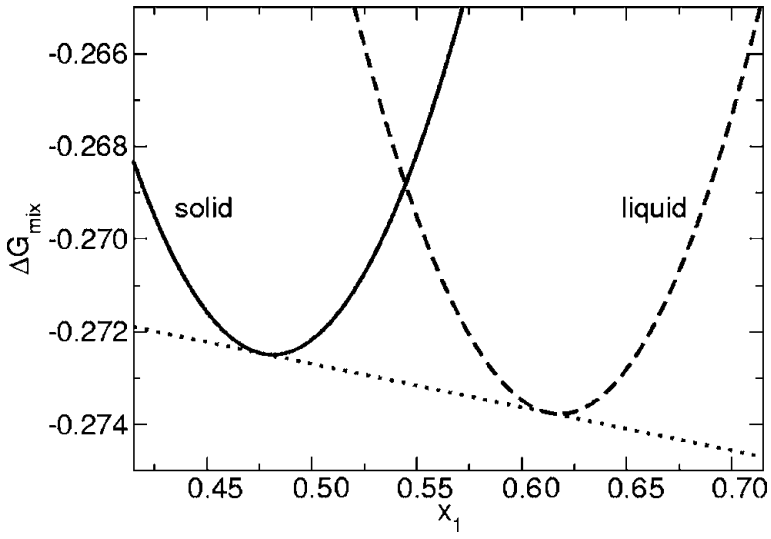

Figure 3.2: Gibbs energies for the solid and liquid versus composition of an ideal Lennard Jones system. Figure reprinted from reference [23].

Another way to directly determine the equilibrium compositions is by computing the semigrand potential, Ω [23],:

$$\Omega = G(T, x_{Pb}) - x_{Pb}\Delta\mu \tag{3.8}$$

If Ω versus $\delta\mu$ fraction for each phase in graphed, the equilibrium composition is the intersection of the two Ω curves. In practice a set of equation is set up for Ω liquid and solid and the compositions is found by solving the equations. By repeating this procedure at several temperatures, a phase diagram of temperature versus composition can be constructed.

3.3 Gibbs-Duhem integration

The Gibbs-Duhem (GD) integration strategy for the calculation of phase equilibria was first proposed by Kofke [56, 57] and applied to a single-component Lennard Jones sys-

tem. Later extensions allowed the technique to be applied to binary Lennard-Jones mixtures in order to generate P versus x_2^l (mole fraction of the liquid component) [58], and T versus x_2^l [59] phase diagrams. The GD integration technique has been successfully employed to analyze 29 binary Lennard Jones mixtures [66], as well as EAM alloys [60], and ternary mixtures [67], among others. This methodology determines the derivate of the phase boundary with respect to the thermodynamic conditions; therefore, the phase boundary is determined only relative to a reference point, which must be determined by other means. The key point of this technique is to write the GD equation in terms of thermodynamic quantities that are easy measurable in simulations. In this case, for each phase in a binary mixture the GD equation is written [58]

$$x_1 d\ln(f_1) = h d\beta + Z d\ln(P) - x_2 d\ln(f_2) \tag{3.9}$$

Here x_i is the mole fraction of component i, f_i is the fugacity ($f = e^{\beta\mu}$) for component i, h the molar enthalpy, $\beta = 1/RT$ R is the ideal gas constant, T is temperature, Z is the compressibility factor, $Z = PV/RT$, and P is pressure. The incorporation of the fugacity fraction, ξ_i, a parameter that varies from 0 to 1 during the integration as opposed to f that change from 0 to ∞, facilities the application of the GD equation [54, 58, 69]:

$$\xi_2 = \frac{f_2}{f_1 + f_2} \tag{3.10}$$

Changing variables from f_2 to ξ_2 the GD equation for binary system becomes

$$d\ln(f_1 + f_2) = h d\beta + Z d\ln(P) - \frac{x_2 - \xi_2}{\xi_2(1 - \xi_2)} d\xi_2 \tag{3.11}$$

The equation 3.11 is valid for both the liquid and solid phases; therefore, it is possible to follow a procedure that is analogous to the derivation of the Clapeyron equation.

Because the fugacity of each component in each phase must be the same to guarantee chemical equilibrium, the corresponding differential form of the Clapeyron equation for a binary system, assuming constant pressure, is

$$\frac{d\beta}{d\xi_2} = \frac{(x_2^L - x_2^S)}{\xi_2(1-\xi_2)(h^L - h^S)} \tag{3.12}$$

Equation 3.12 is integrated numerically, using known conditions that will serve as an input to predict new values of β and ξ_2. The obtained values are used to perform additional semi-grand simulations and refine the calculation. This is a iterative process in which the integration and simulations are used to refine the outcome. Predictor-corrector algorithms have been suggested to integrate Eq. 3.12 [57,59]. Table 3.1 shows some predictor-corrector strategies. Using the trapezoid-rule predictor-corrector, which requires the knowledge of only one previous step, the integration is described by:

$$\beta_{i+1}^{(P)} = \beta_i + [(\xi_2)_{i+1} - (\xi_2)_i]F(\beta_i, (\xi_2)_i) \tag{3.13}$$

$$\beta_{i+1}^{(C)} = \beta_i + \frac{[(\xi_2)_{i+1} - (\xi_2)_i]}{2}[F_{i+1}^{(P)}(\beta_{i+1}^{(P)}(\xi_2)_1) + F_i(\beta_i, (\xi_2)_i)] \tag{3.14}$$

where the super-indexes P, C stands for predictor and corrector respectively, i is the integrator step, and $F(\beta_i, (\xi_2)_i)$ is the integrand from equation 3.12. The predictor-corrector works by selecting a value for $(\xi_2)_{i+1}$, then calculate β. Once this results is obtained, use the new β to perform semigrand MC simulations, which output will be used as an input in equation 3.14 to correct the prediction. The predictor-corrector iteration is repeated until the value of $\beta_{i+1}^{(C)}$ has converged to the desired level of agreement.

The techniques presented in this chapter will be employed in Part III to calculate equilibrium conditions for the Cu-Pb system.

Table 3.1: Predictor corrector methods; n represent the number of previous points required, y_i is the function of step i, h the integration increment (step), and f_i is the integrand of step i.

Name	n	Step type	Formula
Trapezoid	1	Predictor	$y_{i+1} = y_i + hf_i$
	1	Corrector	$y_{i+1} = y_i + \frac{h}{2}(f_{i+1} + f_i)$
Midpoint	2	Predictor	$y_{i+1} = y_{i-1} + 2hf_i$
	2	Corrector	$y_{i+1} = y_{i-1} + \frac{h}{3}(f_{i+1} + 4f_i + f_{i-1})$
Adams	4	Predictor	$y_{i+1} = y_i + \frac{h}{24}(55f_i - 59f_{i-1} + 37f_{i-2} - 9f_{i-3})$
	3	Corrector	$y_{i+1} = y_i + \frac{h}{24}(9f_{i+1} + 19f_i - 5f_{i-1} + f_{i-2})$

Chapter 4

Calculation of interfacial free energies

4.1 Introduction

In this chapter several methods to calculate solid-liquid free energies are reviewed. The solid-liquid interfacial free energy, γ_{sl}, is defined as the reversible work required to form a unit area of interface. This interfacial free energy is a key parameter in solidification and is necessary to understand wetting phenomena [18, 27, 28], nucleation [2, 70, 71] and crystal growth [72, 73]. Over the last 45 years there have been numerous experimental [1–3, 74, 75] and computational [13, 25, 76–81] efforts to accurately estimate its value. Among the most successful computational schemes to calculate the crystal-fluid interfacial free energy (γ_{cf}) for model systems are the capillary fluctuation method (CFM) [13], thermodynamic integration (TI) techniques [16,78,82], and, more recently, the application of the Gibbs-Cahn (GC) formulation [83–86]. Part of the work in this thesis is oriented towards the calculation of γ for fluids and crystals at a static wall. Note that in such cases, the capillary fluctuation method is not applicable because, like faceted interfaces, the interfacial position does not fluctuate. The two suitable approaches for this task are thermodynamic integration techniques: CWM and GC, both

of which are described in the following sections and applied in Part II.

4.2 Thermodinamic integration: The cleaving wall method

The first successful determination of the interfacial free energy for a crystal-melt interface by simulation was performed by Broughton and Gilmer (BG) in 1983 [76]. BG created a thermodynamic integration path that allowed them to calculate the value of the crystal-fluid interfacial free energy (γ_{cf}) for a modified Lennard-Jones system at the triple point. The method employed a series of "cleaving potentials" to perform the separation of the bulk fluid and crystal, which then were rearranged to form the interface. These cleaving potentials need careful tune to create a reversible path (hysteresis free) to ensure that the work measured could be equated to γ_{sl}. Despite the advance in this calculation of γ, the BG implementation was time consuming, requiring a careful analysis as well as large computational resources. Another issue with the BG method was that the statistical and systematic uncertainty was not sufficient to resolve the anisotropy in the values of γ_{cf}, which is crucial in determining the morphology of dentritic growth. For these reasons [16] – specially the time required, the application of the method to other systems was not attempted for several years. Described in the following subsection is an extension of the BG TI approach that allowed for a more efficient and precise calculation of γ.

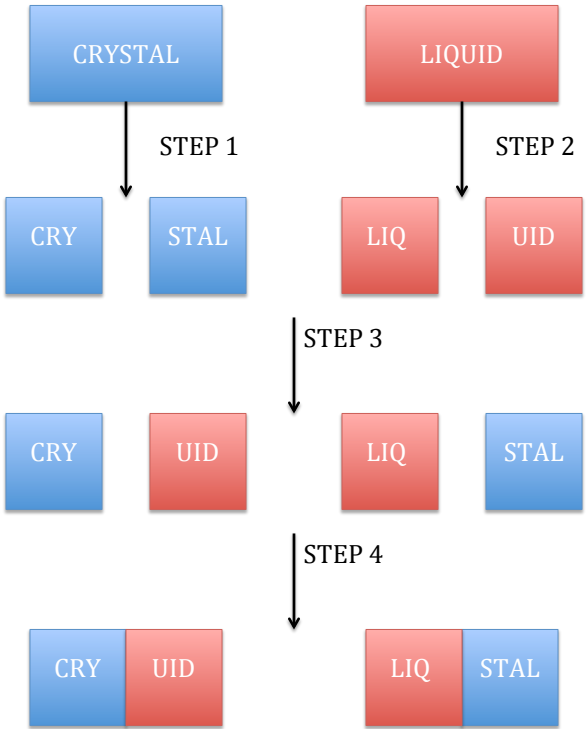

Figure 4.1: Schematic diagram of the cleaving procedure

4.2.1 Cleaving-wall method for the crystal-fluid interfacial free energy

In 2000, Davidchack and Laird [78] improved the cleaving-potential methodology introducing the concept of cleaving walls. In the cleaving-wall method (CWM) the work associated to create an interfacial system from bulk solid and liquid is measured in four steps:

1. Cleave the liquid by inserting a potential wall at a predefined dividing surface.
2. Cleave the crystal in a similar manner.
3. Once the cleaving walls are inserted into the bulk systems, the periodic boundary conditions of each system are rearranged as shown in Fig. 4.1

4. Remove the cleaving walls, resulting in a system in which the crystal and the liquid coexist across and interface.

The interfacial free energy for this method is determined by summing up the work done in each step per area of the interface:

$$\gamma = \frac{1}{A}\sum_{i=1}^{4} w_i$$

Where w_i is the work done in step i. As shown in Fig. 4.2, the reference dividing surface (or cleaving plane) is perpendicular to the z axis, which is chosen as the interface normal. To cleave the bulk at the cleaving plane, the spheres are assigned types 1 or 2 based on their position relative to the plane. During the cleaving of the bulk phases, step one and two, the potential walls, labeled 1 and 2, are inserted on opposite sides of the cleaving plane. The right wall W1 only interacts with the atoms type 1, and similarly, the left wall W2 interacts only with atoms type 2. The position of the wall is defined in terms of z_w; the distance from the walls to the cleaving plane. These walls are moved in small increments, δz, towards the cleaving plane from the starting position z_s, which is sufficiently far from the dividing surface so that the wall-particle potential is zero. The walls are moved until they reach z_f, a position in which the particles in each side of the cleaving plane no longer cross the cleaving plane. The potential associated with the wall $\phi(z_i; z_w)$ is a function of the position of the wall z_w (z_w varies from z_s to z_f) with respect the cleaving plane, and the wall-particle distance (z_i). The wall potential can have any mathematical form as long as the resulting process can be made sufficiently reversible. For the calculations in this thesis, a structureless wall represented by a Week-Chandler-Anderson (WCA) [37, 87, 88] potential is used

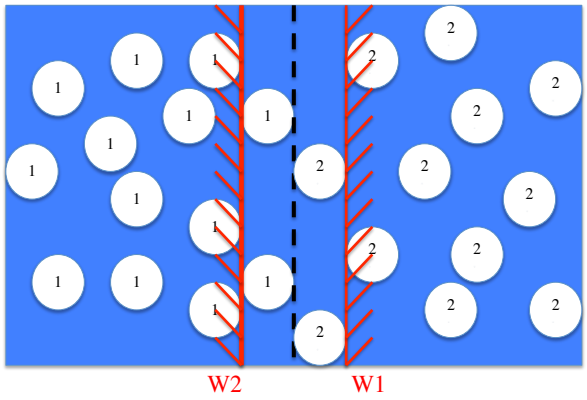

Figure 4.2: Schematic diagram of the cleaving plane, the dashed line in the middle is the cleaving plane, the spheres at the left side are label number one and they only interact with the wall at the right side from the cleaving plane (W1). In the same manner the spheres on the right only interact with the wall on the left W2

$$\phi(z_i; z_w) = \begin{cases} 4\epsilon \left[\left(\frac{\sigma}{z_i}\right)^{12} - \left(\frac{\sigma}{z_i}\right)^{6} \right] + \epsilon, & z_i \leq 2^{1/6}\sigma \\ 0, & z_i > 2^{1/6} \end{cases} \tag{4.1}$$

The work associated with steps 1 and 2 of the cleaving process is then determined by measuring the average value of $\langle \partial\Phi/\partial z_w \rangle$, as the walls move from z_s towards z_f. Mathematically, this is expressed by [16, 80] :

$$w_{1,2} = -\int_{z_s}^{z_f} \left\langle \frac{\partial \Phi}{\partial z_w} \right\rangle dz_w \tag{4.2}$$

Note that, Φ in Eq.4.2 is the sum over all of the particles interacting with the wall and is given by:

$$\Phi(z_w) = \sum_i \phi(z_i; z_w) \tag{4.3}$$

The insertion of the walls cleaves the bulk phases and is depicted schematically in Fig. 4.1. Once the bulk phases are cleaved, the next step is to rearrange the boundary conditions as shown in Fig. 4.1. To perform this step a new potential $U(\lambda)$ is required

that switches the periodic boundary conditions of each bulk phase to form a system where the crystal and the fluid are interacting across an interface. In this work, a linear form for the λ-dependent potential is

$$U(\lambda) = (1-\lambda) \sum_{i<j,AA} u(r_{ij}) + \lambda \sum_{i<j,AB} u(r_{ij}) + \Phi(z_w) \tag{4.4}$$

In Eq. 4.4, the potential $U(\lambda)$ changes from an initial state AA (with the thermodynamic parameter $\lambda = 0$) to a final state AB, ($\lambda = 1$). The state AA corresponds to a system in which the interactions across the cleaving plane are either fluid-fluid or crystal-crystal, while in system AB the interactions are crystal-fluid across the cleaving plane. The work in this step is calculated using

$$w_3 = \int_0^1 \left\langle \frac{\partial U}{\partial \lambda} \right\rangle d\lambda = \int_0^1 \left\langle \sum_{i<j,AB} u(r_{ij}) - \sum_{i<j,AA} u(r_{ij}) \right\rangle_\lambda d\lambda \tag{4.5}$$

The final step consists in the removal of the walls, in a similar manner to step one. The work associated with the final step is:

$$w_4 = -\int_{z_f}^{z_s} \left\langle \frac{\partial \Phi}{\partial z_w} \right\rangle dz_w \tag{4.6}$$

Then, by definition γ_{cf}, is the sum of all the work in arising in each step divided by the interfacial area A:

$$\gamma_{cf} = \frac{w_1 + w_2 + w_3 + w_4}{A} \tag{4.7}$$

Note that, because of periodic boundary conditions there are two individual solid-liquid interfaces created, so that, the area A is twice the cross sectional area of the simulation box. For a more detailed explanation of the cleaving-wall method see References [16, 78, 80].

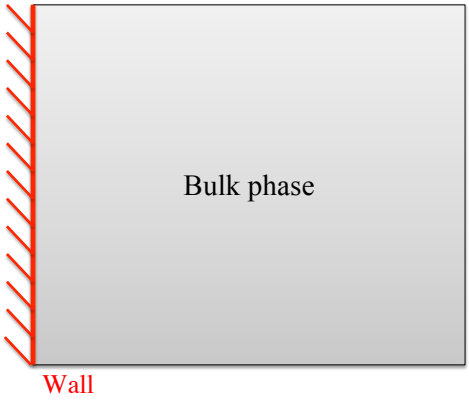

Figure 4.3: Schematic representation of a bulk phase –this could be crystal or fluid– in contact with a potential wall

4.2.2 The cleaving wall method applied to static walls

In this section, a modification to the cleaving wall method for the calculation of the interfacial free energies for systems against a static wall is presented (see Fig 4.3). These wall-bulk systems represent simple models of heterogeneous systems, in which a dynamic solid is replaced with a static wall generated by an external field. The full motivation for this study and results will be presented in Part II, in this section a description of the CWM specifically for wall-fluid and wall-crystal systems is shown.

Comparing Fig. 4.3 with the first two steps of the cleaving procedure for the crystal-fluid case, Fig. 4.1, in both cases there is a bulk phase interacting with a wall simulated by an external field. From this comparison, it is deduced that the first step to calculate γ_{wf} or γ_{wc} is equivalent to the cleaving step; therefore, the work of this step is equal to the work described by Eq. 4.2. Note that, in steps 1 and 2 of the regular CWM, the bulk phases in opposite sides of the walls are still interacting, as shown in the top scheme in Fig. 4.4. Therefore, to obtain γ_{wf} and γ_{wc}, an additional step is required to turn off the interactions across the cleaving plane. This step is a thermodynamic integration

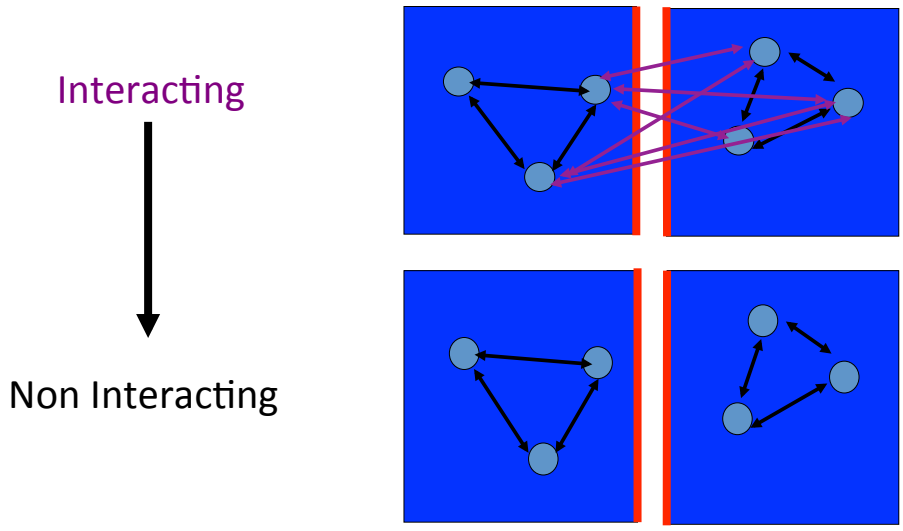

Figure 4.4: Schematic representation of the interactions in the wall-bulk system after the cleaving. In the top the system still has interactions across the cleaving wall (ACP), and the bottom is there are not interaction across the wall ($NACP$)

similar to the one performed in Step 3 for the regular CWM. In this case, the system is converted from a system in which interactions across the cleaving plane (ACP) exist, to a final state where there are no interactions across the cleaving plane($NACP$), see Fig 4.4. The thermodynamic integration potential for the second step is

$$U(\lambda) = (1-\lambda) \sum_{i<j,ACP} u(r_{ij}) + \sum_{i<j,NACP} u(r_{ij}) + \Phi(z; z_w) \tag{4.8}$$

and the work for this step is given by $w_{w2} = \int_0^1 \left\langle \frac{\partial U}{\partial \lambda} \right\rangle d\lambda$. The interfacial free energy between the wall and the bulk is the cleaving work plus the work associated with the dimming the interactions divided by the interfacial area:$\gamma_{wX} = (w_1 + w_{w2})/A$. Where X is either the crystal (c) or fluid (f). Summarizing, the calculation of γ_{wX} consists of two steps:

1. Insert a wall in the bulk phase of interest, as it is done in the steps 1 and 2 of the

regular CWM.

2. Turn off the interactions across the wall.

For additional information on the CMW for systems with static walls the reader is refered to the work of Laird and Davidchack [20] for the hard-sphere fluid at a hard wall. In Part II of this dissertation, this variation of the CWM is applied to soft sphere systems to systematically measure the effect of the range of repulsive interactions in prefreezing phenomena.

4.3 Gibbs-Cahn integration

In this final section, an alternate method for the calculation for the interfacial free energy for a fluid at a static wall is presented. The application of the Gibbs-Cahn (GC) [89,90] formalism has the advantage that it saves significant computational time and resources in comparison with the cleaving wall method without loss of accuracy [83–86]. The Gibbs energy for a liquid with n components in contact with a static surface is given by:

$$G = E - TS + PV \tag{4.9}$$

where E, T, S, P and V are internal energy, temperature, entropy, pressure, and volume, respectively. Meanwhile, for a homogeneous (bulk) system with n components without the surface, the Gibbs energy is given by:

$$G_b = \sum_{i=1}^{n} \mu_i N_i \tag{4.10}$$

The difference between total and bulk Gibbs energies is the interfacial free energy γ times the area:

$$\gamma A = G - G_b = E - TS + PV - \sum_{i=1}^{n} N_i d\mu_i \tag{4.11}$$

Differentiating the previous expression and introducing the Euler equation:

$$dE = TdS - PdV + \sum_{i=1}^{n} \mu_i dN_i \tag{4.12}$$

γ is reduced to:

$$d(\gamma A) = -SdT + VdP - \sum_{i=1}^{n} N_i d\mu_i \tag{4.13}$$

Similarly, the expression for the Gibbs-Duhem equation for a bulk fluid is:

$$-S^f dT + V^f dP - \sum_{i=1}^{n} N_i^f d\mu_i^f = 0 \tag{4.14}$$

These two simultaneous equations can be simplified using Cramer's rule to eliminate one of the variables, as Cahn demonstrated [90]

$$Ad\gamma = -[S/X]dT + [V/X]dP - \sum_{i=1}^{n} [N_i/X]\mu_i \tag{4.15}$$

For a fluid against a wall, the area A is constant and the notation $[Y/X]$ refers to a determinant defined in term of the conjugates variables used in the Cramer's rule:

$$[Y/X] \equiv \frac{1}{X^f} \begin{vmatrix} Y & X \\ Y^f & X^f \end{vmatrix} \tag{4.16}$$

In our system the fluid is a single component liquid, and, the choice of $X = N$ is convenient, yielding

$$Ad\gamma = -[S/N]dT + [V/N]dP \tag{4.17}$$

For this case, the excess volume v_N and entropy η_N per unit of area are defined as:

$$v_N = \frac{1}{A}[V/N] = \frac{1}{A}\left(V - V^f \frac{N}{N^f}\right) \tag{4.18}$$

$$\eta_N = \frac{1}{A}[S/N] = \frac{1}{A}\left(S - S^f \frac{N}{N^f}\right) \tag{4.19}$$

substituting the definitions in the equation for γ, it is found:

$$d\gamma = -\eta_N dT + v_N dP \tag{4.20}$$

which if only isothermal changes are considered γ reduces

$$d\gamma = v_N dP \tag{4.21}$$

Eq. 4.21 is useful, because it simplifies the calculation of γ_{wf} to an integral of the excess volume with respect the change in pressure:

$$\gamma = \gamma(P_i) + \int_{Pi}^{Pf} v_N(P)dP \tag{4.22}$$

The implementation of the G-C integration is simpler than performing the cleaving wall method. However, because the GC method is a first-order differential equation, knowledge of γ at the initial pressure is required. For the inverse power potentials considered here, γ goes to zero in the limit of zero density ($P = 0$), $\lim_{P\to 0}(\gamma) = 0$.

So Eq. 4.22 becomes

$$\gamma = \int_0^{Pf} v_N(P) dP \tag{4.23}$$

Both methods will be applied in Part II for the calculation of γ_{wf} for inverse power potentials (soft spheres).

Part II

Soft-sphere fluid at a structureless soft wall

Chapter 5

Soft spheres against a structureless wall I: Prefreezing phenomena

5.1 Introduction

Recent simulation studies have examined the effect of fluid confinement by external potential fields [17, 18, 20, 27, 91–93]. Notable among these efforts, Courtemanche and Van Swol [17, 27] studied the hard-sphere fluid at a planar wall using MC simulations. The principal finding was the observation of the formation of a thin layer of crystal at the walls at densities below the freezing density for hard spheres. This phenomena was termed prefreezing and was postulated to be a wetting phenomenon. However, Kegel [92], examining the same hard sphere fluid at a hard wall (slit pore geometry), determined that the onset densities for prefreezing could also be explained by capillary freezing.

Recently, the question of the effect of the wall was answered in two studies: The first study, by Dijsktra [18], followed a phenomenological approach; Dijsktra used slit

pore geometry but with multiple sizes systems to rule out capillary freezing. Note that, previous thermodynamic studies by Heni and Lowen [28, 94] were not precise enough in their prediction of interfacial free energies to definitely predict prefreezing . Later, Davidchack and Laird [20, 86] used a thermodynamic approach to predict interfacial free energies and wetting angles with enough accuracy to show that prefreezing was thermodynamically favorable, this treatment will be fully discussed later in this chapter. Both of these studies showed the formation of a crystalline layer at the walls, and clarified the previous reports.

Currently, it is clear that a hard-sphere fluid, at densities close to the coexistence, will form a metastable crystalline layer when in contact with a structureless hard wall. However, it is unknown whether softer interaction potentials would exhibit the same behavior. To this end, we have embarked on a systematic study of the effect of the pairwise interaction in prefreezing using inverse power repulsive soft spheres [95, 96], in order to understand the role of this interactions on the interfacial free energy, which controls the wetting phenomena. The study will be separated in two chapters. In the current chapter the thermodynamics involved are discussed, as well as an introduction to the study systems to be studied, and in the following chapter the results are presented.

5.2 Wetting thermodynamics

Following the approach used by Laird and Davidchack [20] to understand the formation of a crystal layer, it is required to know the conditions under which a substance will ”wet” a substrate. Note that, wetting is defined as the ability of phase “a” to remain in contact with a given substrate when this is in competition with another phase “b”. The

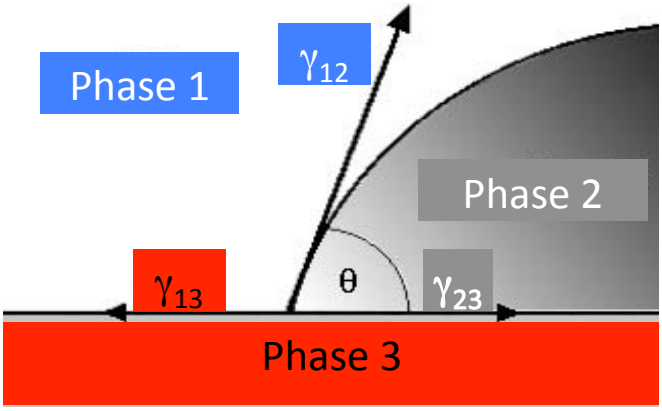

Figure 5.1: Schematic representation of the free energies and wetting angle.

degree of wetting is measured by the wetting angle. As shown in Fig. 5.1, when three phases are in contact due to the equilibrium of the system an angle is formed, this angle is the wetting angle. In the present study, the phase 1 is the fluid, the phase 2 is the possible crystalline structure, and phase 3 is the wall, see Fig. 5.1. The wetting angle is determined from interfacial free energies thorugh Young's equation. The Young's equation [97] for our system is written as:

$$\cos\theta = \frac{\gamma_{wf} - \gamma_{wc}}{\gamma_{cf}} \tag{5.1}$$

where θ is the wetting angle, γ_{wf} is the interfacial free energy (IFE) between the wall and the fluid, γ_{wc} is the wall-crystal IFE and γ_{cf}. According to Young's equation:

- if $\cos\theta \leqslant -1$, phase 2 will not wet phase 3.
- if $-1 < \cos\theta < 1$, phase 2 will partially wet phase 3.
- if $\cos\theta \geqslant 1$, the phase 2 will completely wet phase 3.

By analyzing Eq. 5.1, one sees out that the formation of the wetting layer is a competition between γ_{wf} and γ_{wc} in the numerator. The possible scenarios are illustrated in

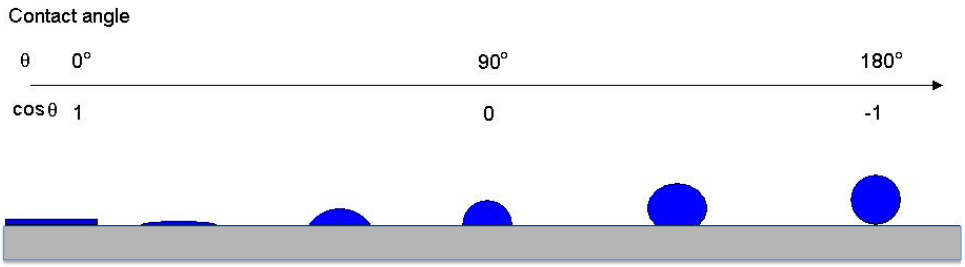

Figure 5.2: Schematic representation of wetting angle values

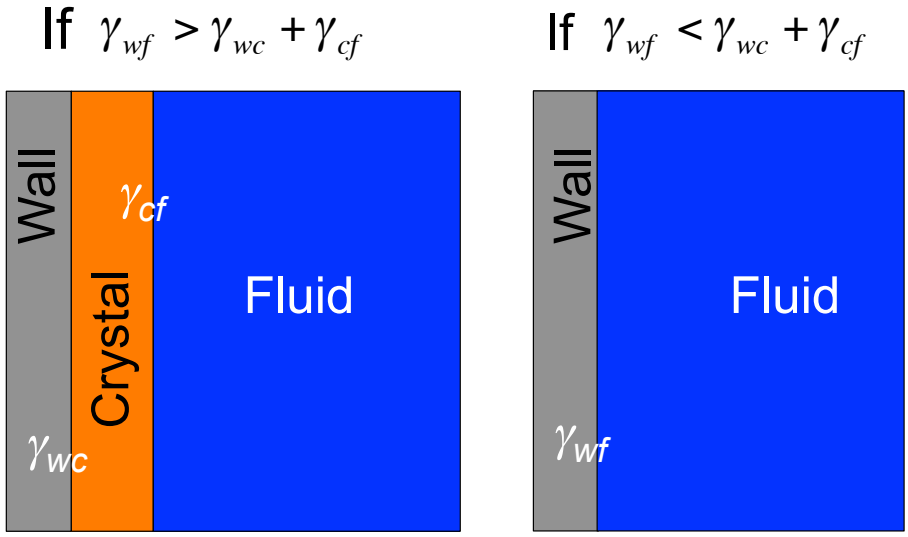

Figure 5.3: Schematic representation of interfacial energies and phases involved in the wetting phenomena in the two extremes of wetting

Fig. 5.3. If $\gamma_{wf} > \gamma_{wc} + \gamma_{cf}$ holds then a crystalline phase will intervene between the wall and the fluid. On the other hand, if $\gamma_{wf} < \gamma_{wc} + \gamma_{cf}$, partial wetting or no wetting will be observed. In order to accurately predict wetting phenomena, we calculated the wall-fluid and wall crystal interfacial free energies for inverse-power soft spheres. A brief description of the inverse power soft-sphere potentials is given in the next section, and it is followed by the simulation details used to calculate these free energies.

5.3 Inverse-power repulsive soft spheres

Inverse-power soft spheres (IPSS) are a standard model for fluid behavior [37]. IPSS have been used to study phase transitions [98, 99] and thermodynamic of fluids [37, 95, 96, 99]. This is because, despite its simple mathematical form, inverse-power soft spheres are able to reproduce macroscopic behavior such as freezing. The mathematical expression for the inverse-power soft-sphere model is:

$$u(r) = \epsilon \left(\frac{\sigma}{r}\right)^n \tag{5.2}$$

Here $u(r)$ is the interatomic potential, ϵ and σ are the energy and length scales, respectively. The range of the interaction is inversely proportional to n (as n increases the range of the interaction decreases) and as $n \to \infty$ they behave as hard spheres. Thus, at high n values, the spheres are "harder", having short-range repulsive interactions, and at low n values the spheres are "softer" presenting longer range interactions, see Fig. 5.4. Thus, by changing n the effect of the extent of the repulsive interaction can be studied systematically. Defining reduced units is useful for these kind of systems, because it facilitates calculations and eases comparisons with real systems. The reduced temperature T^*, pressure P^*, density ρ^* and γ^* are defined [37] by:

$$T^* = k_B T/\epsilon \tag{5.3}$$

$$P^* = P\sigma^3/\epsilon \tag{5.4}$$

$$\rho^* = \rho\sigma^3 \tag{5.5}$$

$$\gamma^* = \gamma\sigma^2/\epsilon \tag{5.6}$$

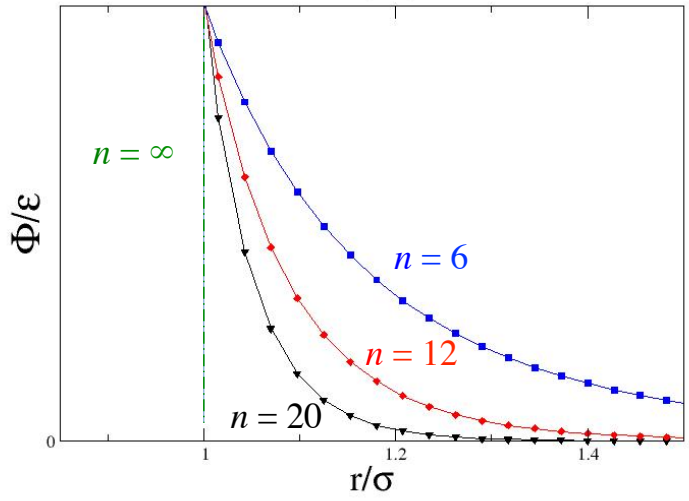

Figure 5.4: Schematic representation of soft spheres; the softness (long range interaction) is inversely proportional to n, meanwhile, the hardness (short range interactions) is directly proportional to n.

Here T, P, ρ and γ are expressed physics units; k_B is Boltzmann's constant. Additionally, the inverse power potentials posses several properties that facilitates their use as general reference. One of IPSS characteristics is that it there is only one independent parameter, $\epsilon\sigma^n$. Because the energy and length scales are not independent the density and temperature are not independent from each other, and any excess thermodynamic property depends only on the quanty [79, 99]:

$$\Gamma_n = \rho\sigma^3 \left(\frac{k_B T}{\epsilon}\right)^{1+3/n} = \rho^* T^{*1+3/n} \tag{5.7}$$

Therefore, the IPSS have a one-dimensional phase diagram, with coexistence fully specified by Γ_n. Given these properties, this potential class is appropiated for a systematic study of the effect of the repulsive interactions on prefreezing was proposed. Systems with $n = 20, 12, 8$ are investigated. The $n = 20$ (short-range interaction) system is expected to behave more like the HS systems reported in Refs. [18,20], while the

effect of the long range interactions will be more clear with $n = 12, 8$ as the potential gets softer. Note that, the $n = 8$ system is thermodynamically stable in the FCC crystalform , but it also possess a BCC phase that, although thermodynamically metastable, is mechanically stable enough to simulate. The interfacial free energies for the crystal-wall γ_{wc} and wall-fluid γ_{wf} are calculated using the CWM – the simulation details are specified in the next section. Additionally, the GC formalism is used to verify the results for γ_{wf} for $n = 8$, the results of these simulations are presented in Chapter 6.

Table 5.1: Coexistence conditions computed using Γ_n taken from Ref. [79], c and f stand for the crystal and fluid respectively, ρ is density, and n is the inverse power of the IPSS (Eq. 5.2).

n	Crystal type	Γ_n^c	Γ_n^f	T^*	ρ_c^*	ρ_f^*
20	FCC	1.052(1)	0.991(1)	0.713(5)	1.000	0.942(1)
12	FCC	1.206(1)	1.163(1)	0.473(2)	1.000	0.964(1)
8	FCC	1.604(2)	1.571(2)	0.284(1)	1.000	0.979(2)
	BCC	1.607(2)	1.578(2)	0.284(1)	1.002(2)	0.982(2)

5.4 Cleaving-Wall Method (CWM) simulation details

The Cleaving-Wall Method (CWM), described in Chapter 4, was used to calculate γ_{wc}, γ_{wf} for several IPSS systems. As described in the previous section, IPSS systems with $n = 20, 12$ and 8 are used. The crystal density, ρ_c^*, was set equal to 1 without loss of generality, and using Eq. 5.7 the coexistence temperatures were calculated for the crystal phase using the coexistence values for Γ_n^c and Γ_n^f reported in Ref. [79].

Once the coexistence temperatures were obtained, the densities for the fluid phase were calculated using these temperatures. The obtained values are shown in Table 5.1. To specify the system size, crystals with $\rho_c^* = 1.000$ were used as a reference, and the number of units cells are shown in Table 5.2. The xy area for each orientation was kept constant for all the simulations and different simulation lengths in the z direction (perpendicular to the walls) were employed to ensure the convergence of the results. The number of spheres (N) for each system were calculated according the coexistence conditions and dimensions previously specified, and ranged from $N = 4860$ to 14580. The box dimensions for the fluid phase were obtained by melting a hypothetical crystal that had the fluid coexistence density; the melt had the same number of units cells used in the (100) crystal.

A Nosé-Poincaré (NP) thermostat [52] (see Chapter 2) was used to perform the NVT MD simulations. The thermostat parameter Q was set to equal to 100, and the initial conditions of the NP extended variables were $s_0 = 1$ and $\pi_0 = 0$ (all the values are in reduced units [37]). The simulations had a radial cut-off for the potential $r_c^* = 2.5$ and a time step $t^* = 0.002$ [$t^* = (\epsilon/m\sigma^5)^{1/2}t$], and a WCA potential (see Chapter 4) was used as a cleaving wall. With these parameters, we calculated γ_{wc} and γ_{wf} for all the described cases. The results of these calculations are discussed in Chapter 6.

5.5 Gibbs-Cahn integration of soft spheres

To confirm the accuracy of the results obtained for γ_{wf} using the CWM, Gibbs-Cahn (CG) integrations (see Chapter 4) were performed for the IPSS $n = 8$ for confirmation. As discussed in Chapter 4, the GC integration can be applied to the calculation of the wall-fluid interfacial free energy γ_{wf}. Given that the GC integration involves

Table 5.2: Numbers of unit cells used for the simulations in the x, y, and z directions, respectively

Crystal type	Crystal orientation	x	y	z
FCC	(100)	9	9	20
	(100)	9	9	30
	(100)	9	9	45
FCC	(111)	12	7	12
	(111)	12	7	18
	(111)	12	7	26
BCC	(100)	9	9	60
	(100)	9	9	90
BCC	(110)	8	5	44
	(110)	9	9	65

computing the excess volume at several densities (see Eqs. 4.21 and 4.22), a simulation box with fixed dimension was employed and particles were extracted randomly to obtain the desired densities. The cross-section dimension of the simulation box were $L_x = L_y = 20\sigma$ and $L_z = 30\sigma$ and WCA repulsive walls were placed at $z = 0$ and $z = 30$, respectively. The number of particles ranged from 754 to 11784. To compute the density profiles, $\rho(z)$, the box length in the z direction, L_z, was divided in 3000 bins of width $\delta z = 0.01\sigma$ and the average $\rho(z)$ was recorded every 1000 time steps. Based on the equilibrium conditions [79], NVT simulations were performed at $T^* = 0.7132, 0.4727, 0.2840$ for $n = 20, 12, 8$, respectively, see Table 5.1. These sim-

ulations employed the NP thermostat parameters described in the CWM. The results from the implementation of CWM and the GC integration are shown in the following chapter, and the implications for the wetting thermodynamics of confined soft-sphere fluids are discussed.

Chapter 6

Soft-sphere fluid at a structureless soft wall II: Results

In Chapter 4 and 5, methods to calculate γ for a fluid at a static wall were introduced. In this chapter, the results from the calculation of γ for a series of model soft-sphere fluids at a structureless wall are presented. In addition, implications with respect to prefreezing are discussed. This chapter is divided in two sections, the first presents the calculation of γ using the cleaving wall method (CWM), and the other section shows, for comparison, the results of the Gibbs-Cahn (GC) integrations.

6.1 Results for γ using the cleaving wall method (CWM)

Using the inverse-power systems described in Eq. 5.2 , the CWM was used to calculate wall-crystal (γ_{wc}) and wall-fluid (γ_{wf}) interfacial energies for these repulsive soft spheres against a soft repulsive structureless wall. The effect of the softness of the sphere, see Chapter 5, is explored by varing the range of the potential. Here we use values of $n = 20$ (short range), $n = 12$ (medium range), and $n = 8$ (long range) in-

teractions. The γ_{wc} for the (111) and (100) FCC crystal orientations, as well as (110) and (100) BCC for $n = 8$, is calculated. Note that, for $n = 8$, FCC is the thermodynamically stable crystal phase, but BCC, although thermodynamic metastable, is mechanically stable enough the over simulation time to allow the study of BCC phases in this system. Similarly, γ_{wf} is calculated for all systems studied ($n = 20, 12$, and 8).

The CWM (modified for wall-bulk systems) discussed in Chapter 4, involves two steps:

1. Insert a the wall to the bulk system.

2. Turn off the interatomic interactions across the cleaving walls.

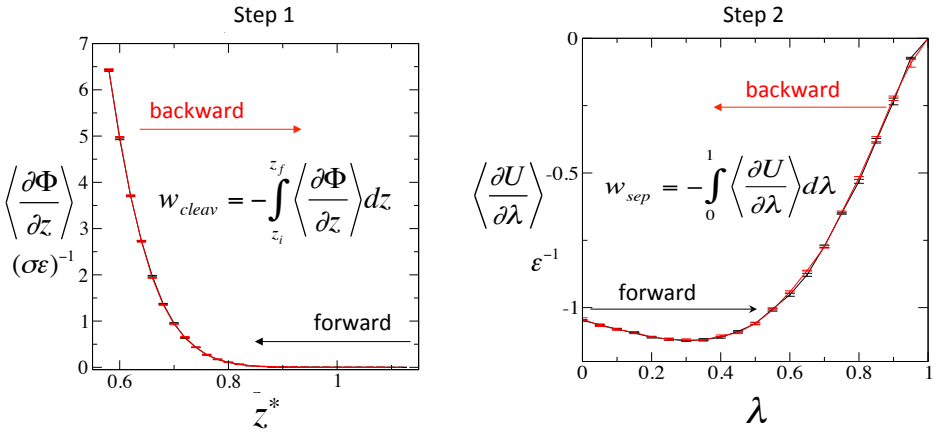

Figure 6.1: CWM results for wall-crystal ($n = 20$ system): left: step 1, right: step 2. The black and red curves represent the forward and backward processes, respectively

For step 1, the cleaving wall was inserted at $z_s^* = 2^{1/6}$, which is the cut-off of potential wall Eq.4.1, and it was moved in increments of $dz_w^* = 0.02$, to a final position $z_f^* = 0.58$ (in reduced units, see Chapter 5). At z_f^* full cleaving was achieved; that is, the particles in the system no longer cross the cleaving plane. The simulation was run for each wall position for 20000 steps –2000 steps were used for equilibration and

18000 were used for block averaging– and statistics were taken from the changes in the wall potential due to the wall movement ($\partial\Phi/\partial z$). To ensure the reversibility of the integration path, the cleaving process was monitored by performing the cleaving process in both forward (from z_s^* to z_f^*) and backward (from z_f^* to z_s^*) directions. As shown in Fig. 6.1, hysteresis in the cleaving process was negligible, indicating that the cleaving process was reversible, within the desired precision.

Our initial attempt to turn off the interactions across the wall used Eq. 4.4, however, a discontinuity was observed at $\lambda = 1$ (the point at which the interactions across the wall were completely switched off). For this reason, Eq. 4.4 was modified in order eliminate the discontinuity:

$$U(\lambda) = (1-\lambda)^2 \sum_{i<j,\, i,j \in ACP} u(r_{ij}) + \sum_{i<j,\, i,j \in NACP} u(r_{ij}) + \Phi(z; z_w) \tag{6.1}$$

Here ACP mean the set of particles interacting across the wall, and NACP is the set of particles that are not interacting across the wall, see Chapter 4. This modification was sufficient to eliminate the discontinuity and define a thermodynamic path sufficiently free of hysteresis – see Fig. 6.1.

With protocols in place to construct reversible thermodynamic paths for both step 1 and 3, we proceeded to calculate and analyze the work in each step and for each system, see Chapter 4. For each γ, three system sizes were simulated, and each integration was performed in both the forward and backward directions (see Fig. 6.1). An example of these results ($N = 4860.9720$ and 14580) is shown in Table 6.1. This analysis showed that the values of γ for the largest two system sizes were identical within the error bars indicating concergence in the results with system size. Tables 6.2 and 6.3 summarize

the values obtained for γ_{wf}, γ_{wc} and the wetting angle (θ) – Eq. 5.1. The values for γ_{cf} were taken from Ref. [79]).

Table 6.1: Sample of the results obtained for the calculation of γ_{wc} for the wall/(111) FCC crystal, $n = 12$, $T^* = 0.473(2)$

L_z	N	Step	Work/A, $\epsilon\sigma^{-2}$ (forward)	Work/A, $\epsilon\sigma^{-2}$ (backward)
23.81	4860	1	0.188(1)	0.186(1)
47.62	9720	1	0.187(1)	0.189(1)
71.43	14580	1	0.186(1)	0.187(1)
23.81	4860	2	–0.523(1)	–0.523(1)
47.62	9720	2	–0.525(1)	–0.526(1)
71.43	14580	2	–0.528(1)	–0.528(1)

The values for γ_{wf} showed more statistical error than those for γ_{wc}. Primarily because the formation of a prefreezing crystal was observed during the insertion of the wall into the fluid, see Fig. 6.2. This metastable layer generated hysteresis because the pressure of the phase transition was reached. To minimize the hysteresis, the increments in λ were made shorter trying to perturb as little as possible the fluid phase. This approach yielded sufficiently precise results for $n = 20$ and 12; however, the extent (measured by the contact angle) of the crystal layer grew as n was decreased and prevented us from obtaining directly γ_{wl} for $n = 8$. To calculate this value, we performed the wall insertion for several fluids with lower densities, and extrapolated linearly using the lower densities to the coexistence density. The final results for γ_{wf} are shown in Table 6.2.

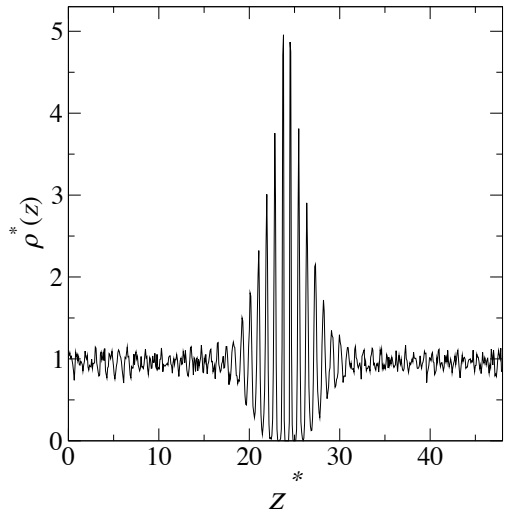

Figure 6.2: Density profile, $\rho(Z)$, for $n = 12$ after cleaving. A prefreezing layer was detected.

Table 6.2: Summary of the CWM results for the fluid phase.

n	γ^*_{wf}
20	0.182(7)
12	-0.071(5)
8	-0.307(6)

In comparison to γ_{wf}, the calculation of γ_{wc} was less difficult, because in all the cases, no phase transition was observed and, therefore, minimal hysteresis was observed. An overall trend was observed that γ_{wc} decreased (become more negative) as the range of the potential increased (decreasing n), see Fig. 6.3. The extent of wetting increased with low n for the closest packing orientations, FCC (111) and BCC(110). Meanwhile, for the FCC (100) the extent of wetting decreased towards a non-wetting state, see Table 6.3.

These findings are in agreement with previous reports on hard-sphere/hard-wall system [18–20,28,86], which reported partial wetting in the (100) orientation and complete wetting in (111). In summary, our primary conclusion in this section is that the propen-

sity for prefreezing (wetting of the wall by a thin crystalline layer) in these systems increases with the increasing range of the potential.

Table 6.3: Summary of the results for the inverse-power crystals at a soft wall.

Crystal	Orientation	n	γ^*_{wc}	$\cos\theta$	Wetting
FCC	(100)	20	0.153(3)	0.08(2)	Partial
		12	0.065(3)	–0.56(2)	Partial
		8	–0.224(3)	–0.65(2)	Partial
FCC	(111)	20	–0.215(4)	1.13(2)	Complete
		12	–0.341(4)	1.22(3)	Complete
		8	–0.514(3)	1.77(9)	Complete
BCC	(100)	8	–0.362(6)	–0.58(14)	Partial
	(110)	8	–0.447(3)	1.60(16)	Complete

6.2 Gibbs-Cahn integration

To obtain an independent verification of our γ_{wf} calculated with the CWM, we have repeated the calcualtion of γ_{wf} using the Gibbs-Cahn (GC) procedure. As described in Chapter 5, GC integration has the following steps:

1. Calculate the excess volume v_n for the wall-fluid system at several bulk fluid densities.

2. Correlate these bulk densities with their corresponding pressure

3. Calcualte γ_{wf} using the associated GC adsorption equation:

$$\gamma(P) = \gamma(P=0) + \int_0^P v_n(P)dP = \int_0^P v_n(P)dP \tag{6.2}$$

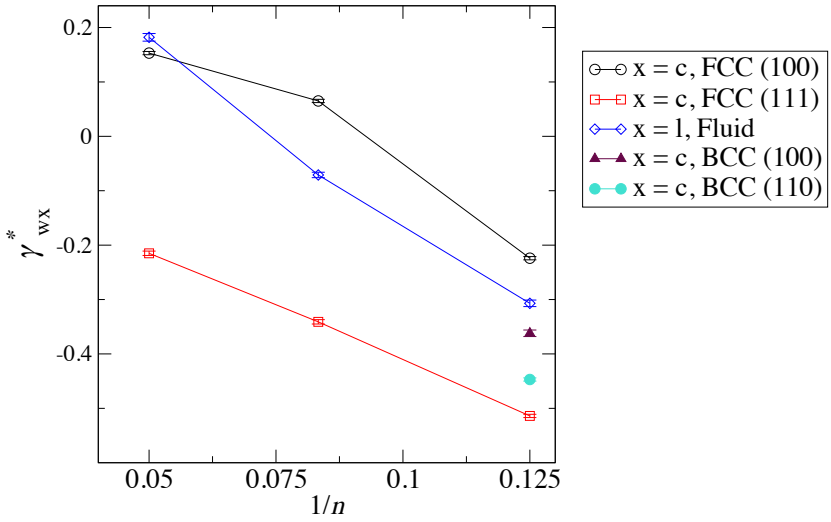

Figure 6.3: Interfacial free energies obtained versus $1/n$

As an example, consider the results for $n = 8$, which was the most difficult calculation in the CWM due to prefreezing. Several simulations, using the conditions described in Chapter 5, were used to calculate the excess volume (v_n^*) of the system at several pressures ranging from 0 to P^*_{coex}. At zero pressure, γ^*_{wf} is equal to zero; this provides a starting point for the integration. However, the excess volume at $P = 0$ is required, which is difficult to calculate accurately from a simulation; nevertheless, $v_n^*(P = 0)$ can be determined exactly using statistical mechanics. In the limit of zero density, the density profile will approach that of the ideal gas in an external field $\rho^*(z) = \rho^*_f e^{-\beta\phi}$. Substituting into the definition of v_n^* gives

$$v_n^* = \int_0^\infty (1 - e^{-\beta\phi(z)} dz) \tag{6.3}$$

here $\phi(z)$ is the Week-Chandler-Anderson (WCA) potential, which is used to describe the repulsive wall and v_n is the excess volume. The limits of the integral in Eq. 6.3

are for the case where the WCA is fully interacting with the system. However, in our case the lower limit is replaced for $z_f = 0.58$, because this position is the stopping point of the cleaving walls. Using z_f as a lower limit, Eq. 6.3 the excess volume at zero pressure. Once the limiting conditions were found, the GC integration was performed. Note that, the value of γ_{wf} and γ_{wc} is dependent of the position of the wall. To take this into account follow a procedure similar to the one described by DeMiguel [68]. In this report the values of γ obtained by Heni and Lowen [94] are rescaled using $\gamma^*_{\text{scaled}} = \gamma^* + P^*_{\text{coex}} z_f$ to have the walls fully interacting at $z = 0$ and $z = L_z$. However, this does not affect the conclusions regarding wetting because the additional term $P^*_{\text{coex}} z_f$ is a constant so $\gamma_{wf} - \gamma_{wc}$ is independent of the defined wall position and Young's equation for the wetting angle only depends upon $\gamma_{wf} - \gamma_{wc}$ (the difference between this values is constant).

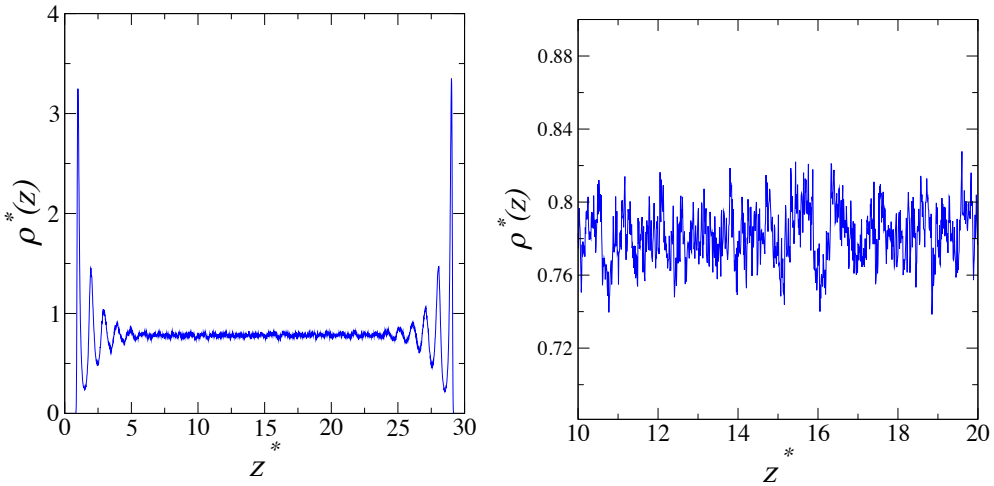

(a) (b)

Figure 6.4: Sample of $\rho^*(z)$ and bulk calculation for $n = 8$, and bulk $\rho^* = 0.7832(3)$. (a) entire density profile, (b) window used to calculated the bulk density

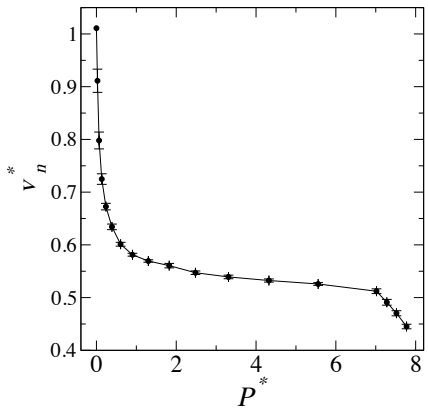

Figure 6.5: Excess volume (v_n^*) versus Pressure (P^*), for the fluid $n = 8$

In order to find the excess volumes, NVT simulations were carried out using the conditions described in Chapter 5. From these simulations the bulk density, excess volume, and bulk pressure were obtained. To refine the precision of the results the simulations had to be run from 5×10^6 to 1×10^7 in this way the statistical error in v_n^* reached the desired values. In order to compute the bulk density, we focused on a region sufficiently far from the wall to not be influenced by it, see Fig 6.4. The range of z over which the bulk density was calculated, chosen for each simulation, the range varied from $10 < z^* < 20$ to $7 < z^* < 23$. With the obtained bulk liquid densities, the bulk pressures were computed doing NVT using a simulation box without potential wall. The excess volumes with its corresponding pressure is shown in Fig. 6.5 .

Next, γ_{wf} is computed from the calculation of $v_n(P)$ Eq. 3. The trapezoid rule was used to perform the integration, because the use of a numerical quadrature facilitates the error propagation, see Fig. 6.6. The value obtained for $1/r^8$ $\gamma_{wf} = -0.302(9)$, which is in agreement, within the error barns, with the value found in the CWM: $\gamma_{wf} = -0.307(6)$. Both values agree within the error bars. This agreement gives us confidence in the values obtained using the CWM.

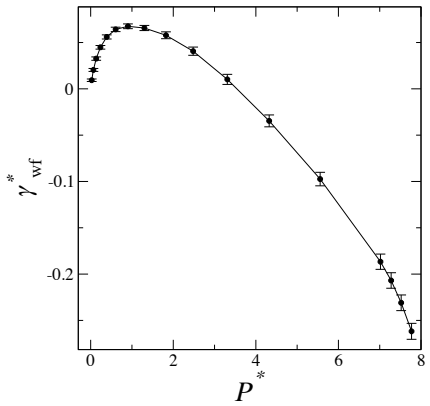

Figure 6.6: Wall-fluid interfacial free energy versus pressure, $P^* = P\sigma^3/\epsilon$, for $n = 8$

Summarizing the results, a prefreezing layer of the closet packed crystal [(111) FCC and (110) BCC] was predicted for the inverse-power soft-sphere fluid at structureless soft wall for all the values of n studied ($n = 20, 12, 8$). The prefreezing layer (predicted by the wetting angle) was more favorable with long range interactions potential than with short range interaction. An independent calculation of γ_{wf} for $n = 8$ using the Gibbs-Cahn (GC) integration was performed to compare the value of γ_{wf}obtained using the cleaving-wall method (CWM), both methods yielded the same value within the error bars. This comparison enhances our confidence in the observations made.

Part III

The Cu-Pb crystal-liquid interface

Chapter 7

The Cu-Pb crystal-liquid interface I: Introduction and methods

7.1 Introduction

In this part of the dissertation, molecular-dynamics (MD) and Monte-Carlo (MC) computer simulations are used to characterize the atomistic structure, energetics and transport properties of the chemically heterogeneous solid-liquid interface between solid Cu and molten Pb, as a function of temperature. As defined earlier in this thesis, chemically heterogeneous solid-liquid interfaces are systems in which a sudden change in the composition takes place at the interface. This part of the thesis is divided in two chapters. In the present chapter the basic concepts, simulation details and analysis definitions are presented, and in the Chapter 8 the obtained results are discussed.

The thermodynamic and structural properties of chemically heterogeneous solid-liquid interfaces are controlling parameters for a number of technologically relevant phenomena, such as heterogeneous nucleation, wetting and casting [4]. However, our

current understanding of such interfaces is far from complete. Because experimental studies [6–9, 100] on such interfaces are difficult and rare, much of our current phenomenological understanding of solid-liquid interfaces has been guided by atomistic simulation studies.

In recent years, fully atomistic simulations, focused on the characterization of solid-liquid interfaces in simple multi-component systems, have been focused mainly on binary mixtures close to ideality - systems in which the chemical heterogeneity across the solid-liquid interface is not large. Examples include hard-sphere mixtures [22, 101], LJ mixtures [23, 24] and nearly ideal metal alloys, such as Cu/Ni [25, 26]. Simulations on systems with much larger composition differences between solid and liquid have been rarer. One example is the work of Geysermans, *et al.*, [102], which examined the interface between solid Cu and liquid Al. In Ref. [102], both the (100) and (111) interfaces were characterized at T = 1000K through the calculation of changes in density and diffusion constants as the interface is traversed from solid to liquid. As expected from previous simulations on model systems, the presence of the solid Cu wall induces significant structure in the liquid Al density profiles near the interface. Both the diffusion profiles and the interfacial structure of the liquid were observed this system to be largely independent of interfacial orientation.

The present study was motivated by recent simulations by Webb, *et al*, [30], which examined the spreading of liquid Pb droplets on Cu surfaces, and reported a strong dependence of the spreading kinetics on Cu crystal orientation, see Fig. 1.2 . Webb, *et al*, found that the (111) Cu-crystal orientation exhibited significantly faster spreading than the (100). They also observed Cu-Pb interfacial alloying in the (100) orientation, which was absent in (111). One possible origin of this anisotropy in spreading kinetics

could be the orientation dependence of the atomic structure and kinetics of the Cu/Pb interface, which would be in contrast to the weak anisotropy seen in Cu/Al [102]. In this chapter, the structure and transport kinetics of the Cu/Pb solid-liquid interface are defined as a function of interface orientation - specifically the (100) and (111) interface orientations of the Cu crystal - and the obtained results, presented in the next chapter, helped to understand, on an atomic level, the strong anisotropy in spreading kinetics. The Cu/Pb interface is characterized by the calculation, via MD simulation, of profiles showing the changes in energy, density, stress and diffusion constant across the interface. In addition, 2-d structure factors and density maps are calculated to show the structure of the interface in atomic detail.

7.2 System and simulation details

In this work, an embedded atom method (EAM) potential for Cu-Pb developed by Hoyt, *et al.*, [45] is used to model the interatomic interactions –see Chapter 2 for more details about the EAM potential. This EAM potential was developed from existing EAM models of pure Pb and Cu by fitting the cross interactions to reproduce the experimental enthalpy of mixing as a function of composition. This potential has been previously used to simulate the spreading of Pb droplets on a Cu substrate [30] (discussed previously), as well as to study the dynamics of Cu-Pb nanodroplets [103]. The predicted melting temperatures (T_m) for pure Cu and Pb within this model are 1279 K [45] and 618 K [104], respectively. (The experimental values are 1357.8 K and 600.6 K for Cu and Pb, respectively [111].) The melting points were calculated using the techniques described in Chapter 3, and the T_m for Pb was recalculated using a series of cooling and heating simulations and was in agreement with previous reports. Given that the purpose

of this study is to understand the general behavior of the interface and not to reproduce the exact features of the phase diagram, the discrepancy between the experimental and theoretical melting points is acceptable.

The MD simulations were performed using the program LAMMPS [105] distributed by Sandia National Laboratory, LAMMPS was chosen due its ability for parallelization for MD calculations. For a more detailed description of MD simulation techniques and definitions, see Chapter 2. A time step of 1.0 fs was used in all simulations. All simulations were performed using a Nosé-Hoover thermostat [50] at temperatures of 625 K and 750 K and a thermostat relaxation time of 0.1 ps. In addition to the constant-volume simulations (NVT) used in the calculation and analysis of density profiles, two types of constant-pressure simulations were performed: NPT simulations, with isotropic volume fluctuations, and NP_zAT simulations, in which the box length in the direction of the interface normal (denoted by z) is allowed to fluctuate at fixed xy cross-sectional area (A). In the constant pressure simulations, an Anderson piston barostat is employed with a relaxation time constant of 1.0 ps. In all simulations, periodic boundary conditions are applied in all Cartesian directions.

At 625 K and zero pressure, Cu and Pb are effectively immiscible in bulk, so the simulations begin with the equilibration of separate pure Cu (crystal) and pure Pb (liquid) samples at constant pressure and temperature. For the simulations at 750 K the equilibrium concentration for the liquid phase was found using the techniques described in previous chapters, a full discussion of how the concentration was obtained will be presented in the next chapter. The systems used in the simulations at both temperatures had the same total number of atoms but some of the Pb atoms were exchanged for Cu to meet required equilibrium concentration. In the next paragraphs the 625 K interfaces assembly and analysis is discussed, and the same principles apply to 750K at the equilibrium concentration. For the (100) interface simulation, a sample of bulk

Cu crystal was prepared with 15360 atoms ($32 \times 32 \times 15$ standard FCC unit cells). This sample was equilibrated using isotropic NPT MD simulation to determine the dimensions of the equilibrium unit cell. A configuration from this equilibrium run that had an instantaneous unit cell length that matched the average equilibrium unit cell distance was chosen as the starting crystal for interface construction. A similar procedure was performed for the (111)-oriented crystal, which contained 18144 atoms. ($24 \times 14 \times 9$ unit cells using a unit cell containing 6 basis atoms with dimensions $\frac{\sqrt{2}a}{2} \times \sqrt{\frac{3}{2}}a \times \sqrt{3}a$ constructed with a z axis normal to the (111) orientation.) After equilibration of the crystal samples, separate samples of liquid Pb containing 12000 particles each were equilibrated using NP_zAT MD, fixing the xy cross-sectional dimensions to match the cross-section for (100) or (111) crystals. The cross-section dimensions were $L_x = L_y = 58.44$Å for (100) and $L_x = 62.00$Å $L_y = 62.65$Å for (111). To assess the dependence of our results on cross-sectional area, we performed simulations on systems with cross-sectional areas that were one-fourth and four times that of our production runs, respectively. While the smaller system showed some significant differences from the results presented here, the properties of the larger system were identical to those of our production system within the error bars indicating the convergence of our results with respect to system size.

The interface was assembled by conjoining the crystal Cu and liquid Pb samples at their common cross-sections and applying periodic boundary conditions to the conglomerate. An initial gap of 1.55Å between the crystal and liquid was used to mitigate the effect of high-energy interactions generated by the broken symmetry. The assembled interfaces are shown in Fig 7.2. After assembling the interface, the following equilibration procedure was employed. First, the liquid Pb is equilibrated at a static Cu surface using an NP_zAT MD run of length 4.5 ps - this is done by freezing the Cu atomic positions during this run. The subsequent configuration is then equilibrated

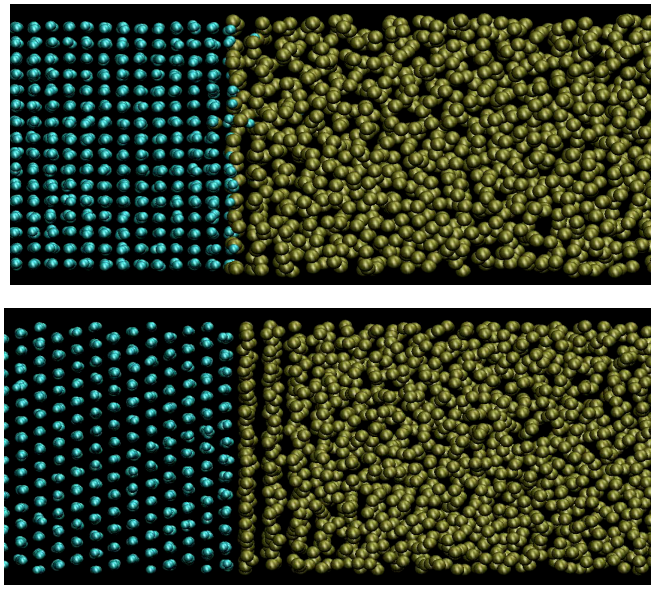

Figure 7.1: Cu-Pb solid liquid interfaces, Cu-Pb (100) interface (top), Cu-(111) interface (bottom).

using NP_zAT MD for all atoms of the system for 2.5 ns (2.5×10^6 steps). During this run the total energy, temperature and volume were monitored to verify the approach to equilibrium. After 200 ps, these quantities exhibited no observable drift.

To characterize the interface, a variety of z-dependent profiles (e.g. energy, density, etc.) were calculated, where the z direction is the direction normal to the interfacial plane, the formal definition are presented in the following section. These profiles are produced by binning the simulation box along the z direction. The use of NP_zAT MD simulation for such binning is problematic because of fluctuations in the length of the box in the z direction, L_z, which causes the volume of the individual bins to be time dependent. Because of this NVT MD simulation are used for the calculation of interfacial profiles. To do this, we use the final 2.0 ns of the NP_zAT equilibration run to compute the average L_z for this system. The NVT simulation is started from a configuration chosen from the NP_zAT with an instantaneous L_z that closely matches

the average. For the NVT simulations, we also hold fixed the atoms in the innermost layer of the Cu crystal. This layer is held static to avoid Brownian motion of the Cu crystal slab - a result of the fact that the MD simulations conserve linear momentum, but not linear velocity, due to the difference in the masses between the Cu and the Pb. Results for the profiles with or without the static inner were statistically identical layer, but fixing the inner layer improved the quality and ease of measurement of the 2d interfacial structure.

7.3 Interface characterization

The interface is characterized primarily through the calculation of profiles, which measure changes in a given quantity as the interface is traversed along the interface normal (here defined as the z axis). In this study, we report two types of profiles: fine-scale profiles and filtered coarse-grained profiles. The fine-scale profiles are determined by binning the z direction and averaging the quantity of interest within each bin over the xy plane. The bin size for these profiles was chosen to be 1/25th of the interplane spacing in the Cu crystal corresponding to a bin size (Δ_z) of 0.084Å for the (111) interface and 0.073Å for (100).

To generate the coarse-grained profiles we apply a finite response filter (FIR) [106, 107] in which the value of the profile at a given value of z is given by a weighted average over neighboring values. The FIR is defined as:

$$\bar{f}_n = \sum_{k=-N}^{N} w_k f_{n+k} \tag{7.1}$$

The weighting coefficients (w_k) are defined by

$$w_k = Ae^{-(k/\epsilon)^2} \tag{7.2}$$

The w_k values are determined by minimizing the quantity:

$$\sigma = \sum_k (\delta^2 \bar{f}_k)^2 \tag{7.3}$$

where $\delta^2 \bar{f}_k$ is the second central difference defined as: $\delta^2 \bar{f}_k = \bar{f}_{k+1} + \bar{f}_{k-1} - 2\bar{f}_k$. The quantity A is determined from the normalization condition $\sum w_k = 1$. Conditions for optimization of the parameter ϵ were described by Buta *et al.*, [108] For our simulations, the optimized value for ϵ is 28 with N=150.

The specific interfacial parameter profiles are defined as follows:

(a) *Density profiles:* The density profile $\rho_i(z)$ (i = Cu or Pb) for each atom type is defined by

$$\rho_i(z) = \frac{\langle N_z^i \rangle}{A_{xy}\Delta_z} \tag{7.4}$$

where Δ_z is the bin spacing, $\langle N_z^i) \rangle$ is the average number of atoms of type i in the bin defined by $z - \Delta_z/2 < z < z + \Delta_z/2$ and A_{xy} is the interfacial area. Because of periodic boundary conditions there are two solid-liquid interfaces in the simulation. To improve the statistics, the density profiles (and all parameter profiles in this work) reported here are averaged over the density profiles for each two independent interfaces.

(b) *Potential energy profile*: The potential energy profile, $U(z)$, is computed by averaging the potential energy ($\langle U_z \rangle$) contained in each bin and dividing by the volume of the bin:

$$U(z) = \frac{\langle U_z \rangle}{A_{xy}\Delta z} \tag{7.5}$$

where $\langle U_z \rangle$ is the average total potential energy of the atoms in the bin, as defined above for the density profile.

(c) *Stress profile*: Another profile of interest is the stress profile, $S(z)$, which is determined from the components of the pressure tensor, P_{ij}:

$$S(z) = P_{zz} - \frac{1}{2}[P_{xx}(z) + P_{yy}(z)] \tag{7.6}$$

$S(z)$ measures the difference between the longitudinal and transversal average pressures. For a solid-liquid interface under hydrostatic stress, $S(z)$ should be zero away from the interfacial region. This is especially critical to monitor in the bulk solid, as residual stress in this region is an indication of a faulty interface equilibration protocol.

(d) *Diffusion-Coefficient profile*: To calculate the diffusion profile, we utilize bins along the z direction defined as the regions between the minima of the density profile. For each of these bins, we calculate the average mean-square displacement (MSD) per particle, $\langle |\mathbf{r}_j(t) - \mathbf{r}_j(t_0)|^2 \rangle_z$, for particles initially in the bin centered at z at time $t = 0$. In addition to averaging over all atoms in each bin, we also average over 50 time origins separated by 0.5 ps (500 time steps). Once the MSD is calculated as a function of time, the diffusion constant is determined from the limiting slope of the MSD versus time plot:

$$D(z) = \frac{1}{6}\frac{d}{dt}\langle [\mathbf{r}_j(t) - \mathbf{r}_j(t_0)]^2 \rangle_z \tag{7.7}$$

In addition to the profiles, we also determine the excess interfacial energy, e, and stress, τ. The interfacial excess of any thermodynamic quantity is determined by defining a Gibbs dividing surface [2] that divides the two phases separated by the interface (here, solid and liquid). Such excesses are useful in determining the dependence of γ_{sl} on temperature [85, 109]. Because our system is under hydrostatic conditions, the ex-

cess stress in the bulk phases is zero and the excess interfacial stress, τ, is independent of the dividing surface. This is not true for the excess energy, so a dividing surface must be specified in this case. In these calculations, we use a planar dividing surface constructed by setting the interfacial excess number of Cu atoms to zero ($\Gamma_{\mathrm{Cu}} = 0$). The position of this dividing surface can be determined by solving the equation:

$$\Gamma_{Cu} = \frac{N^{\mathrm{Cu}}}{A_{xy}} - L_{\mathrm{sol}} \cdot \rho_{\mathrm{sol}}^{\mathrm{Cu}} - (L - L_{\mathrm{sol}}) \cdot \rho_{\mathrm{liq}}^{\mathrm{Cu}} = 0 \tag{7.8}$$

where N^{Cu} is the total number of particles of Cu, L is the total length of the simulation box, L_{sol} is the length of the solid in the z direction, and $\rho_{\mathrm{sol}}^{\mathrm{Cu}}$ and $\rho_{\mathrm{liq}}^{\mathrm{Cu}}$ are the density of Cu in the solid and liquid, respectively. Because we are working in a region of the phase diagram where there is no solubility of the Cu in the liquid Pb, $\rho_{\mathrm{Cu}} = 0$ and we can solve to obtain L_{sol}:

$$L_{sol} = \frac{N^{\mathrm{Cu}}}{A_{xy} \cdot \rho_{\mathrm{sol}}^{\mathrm{Cu}}} \tag{7.9}$$

The dividing surfaces for the two interfaces in the simulation are then fixed symmetrically (relative to the center of the solid) a distance L_{sol} apart. For simplicity, the dividing surface is defined as $z = 0$ in the parameter profiles . With these lengths defined we can now express the excess stress and energy as follows:

$$\tau = \int_{L_z} S(z) dz \tag{7.10}$$

where the integral is taken over the entire length of the cell, and

$$e = \frac{E_{\mathrm{sys}}}{2A_{xy}} - [\rho_e(\mathrm{sol}) \cdot L_{\mathrm{sol}} + \rho_e(\mathrm{liq}) \cdot L_{\mathrm{liq}}] \tag{7.11}$$

where E_{sys} is the total energy of the system and $\rho_e(\mathrm{sol})$ and $\rho_e(\mathrm{liq})$ are the bulk solid

(Cu) and liquid (Pb) potential energy densities, respectively.

Finally, to study the interfacial structure in atomic detail, we calculate 2-dimensional densities $\langle \rho_{xy}(\vec{r}) \rangle$ for the first two Cu layers and first two Pb layers at the interface, as well as Cu and Pb layers in the bulk solid and liquid (i.e., far from the interface), respectively. These calculations were performed for (111) interface orientations. Each plane was divided in 225 bins in the x direction and 384 bins in the y, and the average position of the atoms involved is calculated over 2 ns from the recorded positions taken every 1 ps. In addition, to better visualize periodic structures in the inteface layers, we calculate the 2-d structure factor [110], defined as

$$F_{xy}(\vec{k}) = \langle |\rho_{xy}(\vec{k})|^2 \rangle \tag{7.12}$$

where $\rho_{xy}(\vec{k})$ is the Fourier transform of the 2-d instantaneous particle density $\rho_{xy}(\vec{r})$. To calculate $F_{xy}(\vec{k})$ instantaneous structure factors were calculated from configurations recorded every 1 ps (1000 time steps) and averaged over the final 2 ns of the simulation run. The results obtained from the application of this methodology are presented in the next chapter.

Chapter 8

The Cu-Pb crystal liquid interface II: Results and discussion

In this chapter, our the results for the Cu-Pb interface are presented. In the first section we discuss the determination of the equilibrium composition of crystalline Cu and liquid Pb at the temperatures of interest. Next, we describe a detailed characterization of the Cu(100)/Pb and Cu(111)/Pb interfaces at $T = 625$ K and $T = 750$ K using the methods described in Chapter 7. Through this study we are able to understande the anisotropic behavior of the system. In the final section, a study of the effect of surface alloying and prefreezing on heterogeneous nucleation is discussed.

8.1 Equilibrium compositions

The first step to characterize the Cu-Pb interface is to determine the equilibrium compositions at the temperatures of interest: 625 K and 750 K. For the system at 625 K (just above the melting point for this model, 618 K), we assumed that the crystal Cu and liquid Pb are completely segregated is very reasonable, see Fig. 8.1. The assump-

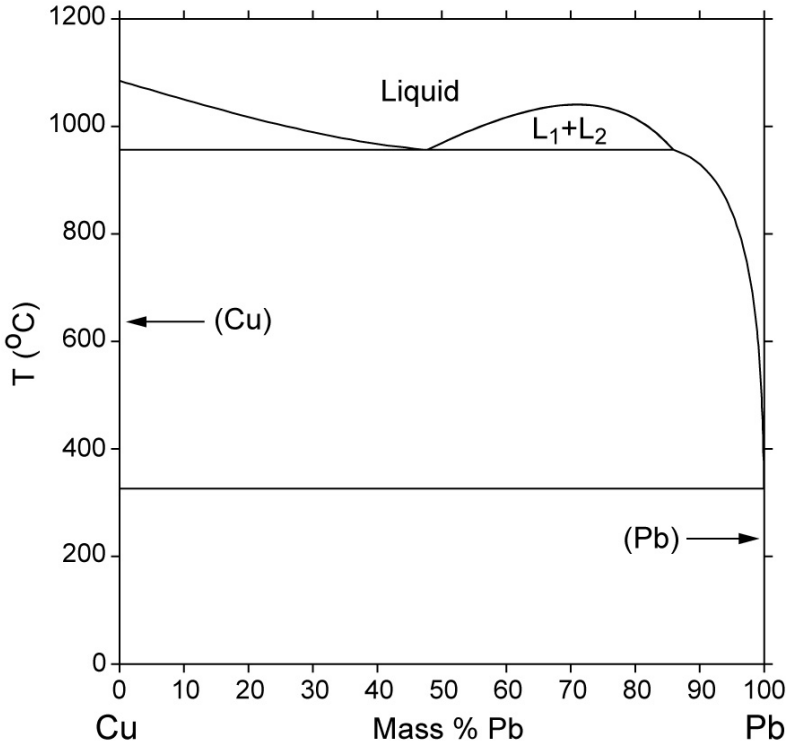

Figure 8.1: Cu-Pb experimental phase diagram [111] .

tion is based on the experimental phase diagram, which shows only traces of Cu in the liquid Pb and no Pb in the solid Cu. This assumption was validated by the fact that the complete segregation was stable to a high degree over very long MD runs. However, this was not the case for 750K. In simulations performed assuming complete immiscibility, the composition was unstable over the course of the simulation and a significant number of Cu atoms were dissolved into the liquid Pb phase, see Fig. 8.2. Several approaches were applied to determine the correct equilibrium composition as discussed in the following subsections.

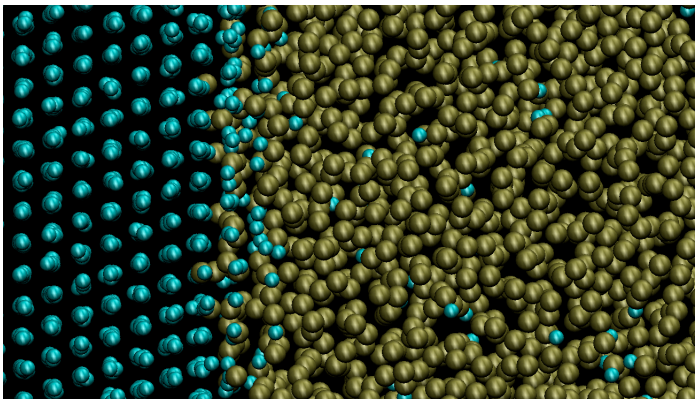

Figure 8.2: (111) Cu-Pb disolved after 38ns at 750 K, the first two Cu layers disappeared at this time.

8.1.1 Gibb-Duhem integration

The first method applied to determine the equilibrium mole fractions was the Gibbs-Duhem (GD) integration, – see Chapter 3 for details. Our initial attempt used the same parametrization of the GD equation discussed by Hitchcook and Hall [59]. However, after analyzing the results it was observed that the parameter ξ_2, see Eq. 3.9, changed rapidly from 0 to almost 1 (at the upper temperatures 1279K to 1150K). This effect was due to the extreme non ideality of the system, in which the liquid and solid phase are severely segregated, see Fig. 8.1. Because of this problem Eq. 3.9 was re-formulated in terms of temperature T and chemical potential $\Delta\mu$, instead β and ξ, respectively. Starting with the Gibbs-Duhem equation for mixtures:

$$-S\,dT + V\,dP - \sum_{i=1}^{r} N_i\,d\mu_i = 0 \tag{8.1}$$

For the binary systems considerd here, we set $r = 2$ with $N = N_1 + N_2$, Eq. 8.1 becomes

$$-s\,dT + v\,dP - x_1\,d\mu_1 - x_2\,d\mu_2 = 0 \tag{8.2}$$

Using the fact that $x_1 + x_2 = 1$ and defining $\Delta\mu = \mu_2 - \mu_1$, gives

$$\begin{aligned} -s\,dT + v\,dP - (1-x_2)\,d\mu_1 - x_2\,d\mu_2 &= 0 \\ -s\,dT + v\,dP - d\mu_1 - x_2(d\mu_2 - d\mu_1) &= 0 \\ -s\,dT + v\,dP - d\mu_1 - x_2 d(\Delta\mu) &= 0 \end{aligned} \tag{8.3}$$

Rearranging and setting $dP = 0$ (constant pressure) gives

$$d\mu_1 = -s\,dT - x_2 d(\Delta\mu) \tag{8.4}$$

Now we pick two infinitessimally separated points (1) and (2) along the $T - \Delta\mu$ coexistence diagram separating two phases α and β. The coexistence condition gives

$$d\mu_1^{\alpha}[(1) \to (2)] = d\mu_1^{\beta}[(1) \to (2)] \tag{8.5}$$

Applying Eq. 8.4 to both sides of Eq. 8.5 gives

$$-s^{\alpha}dT - x_2^{\alpha}d(\Delta\mu) = -s^{\beta}dT - x_2^{\beta}d(\Delta\mu) \tag{8.6}$$

Rearranging gives

$$\frac{dT}{d(\Delta\mu)} = -\frac{x_2^{\beta} - x_2^{\alpha}}{s^{\beta} - s^{\alpha}} \tag{8.7}$$

Using the fact that $\Delta H = T\Delta S$ at coexistence gives

$$\frac{dT}{d(\Delta\mu)} = -\frac{T(x_2^{\beta} - x_2^{\alpha})}{h^{\beta} - h^{\alpha}} \tag{8.8}$$

The implementation of this equation was done using semi-grand MC simulations (see Chapter 2) to compute the mole fractions and enthalpies in Eq. 8.8. Using semi-grand

MC to find the enthalpies and mole fractions for Eq. 8.8, the output values for $\frac{dT}{d\mu}$ were -457.4 K/eV to -470 K/eV for 1100 K and 1050 K respectively. However, from previously compositions at 1100 K and 1050 K [45], the slope predicted was $\frac{\Delta T}{\Delta \mu} = -833.3$ K/eV. The reason for discrepancy still unsolved, all the input files and programs were re-examinated carefully and no error was found. Given this drawback, it was decided to apply the common tangent construction as described below.

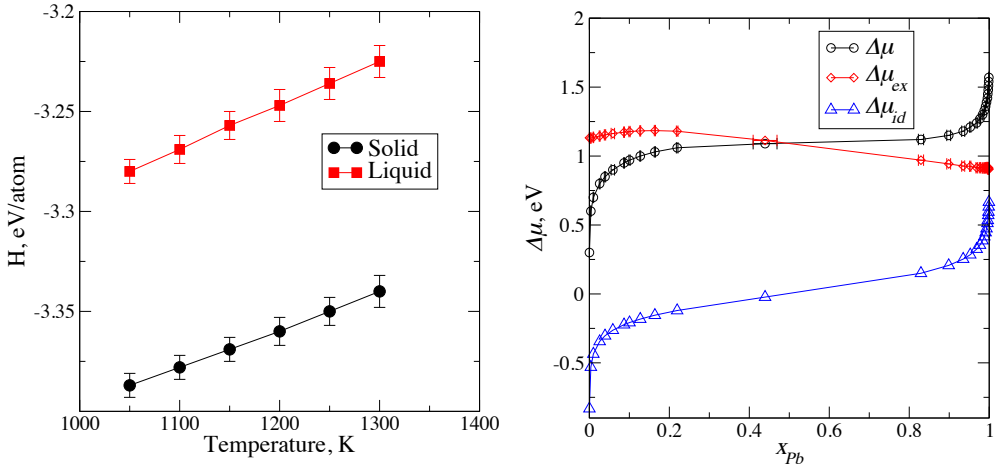

(a) (b)

Figure 8.3: (a) Enthalpies for pure Cu, liquid and solid phases, (b) chemical potentials versus composition for the liquid phase.

8.1.2 Common tangent construction

Using the common tangent construction (CTC) described in Chapter 3, the equilibrium compositions at 1100 K and 1050 K were calculated to ensure that the implementation of the method was correct. Following the description in Chapter 3, the enthalpies for pure Cu obtained from using NPT simulations are show in Fig. 8.3(a). The next step in the calculation consisted in the determination of $\Delta\mu(x_{Pb})$ for both solid and the liquid phases, as shown on Fig. 8.3(b). The process continued with the calculation of ΔG for

the liquid and solid phases, see Fig. 8.4(a) and concluded with the computation of the semigrand potential, as shown in Fig. 8.4(b). From these calculations the Pb equilibrium concentrations at 1100 K are $x_{Pb}^{L} = 0.130(2)$ and $x_{Pb}^{S} = 0.0076(1)$, for the liquid and solid respectively, and for 1050 K, $x_{Pb}^{L} = 0.177(2)$ and $x_{Pb}^{S} = 0.0085(1)$. Note that, these values were obtained without the assumption used by Hoyt *et al* [45] that the solid Cu was pure. Ref. [45] reported only the liquid phases: $x_{Pb}^{L} = 0.126$ at 1100 K and $x_{Pb}^{L} = 0.180$ (the last value was extrapolated from plot). Because the trapezoid rule was used to integrate the curves, our numbers also included the error propagation which was reported in Ref. [45]. Given the agreement obtained, we proceeded to calculate the composition at 750 K.

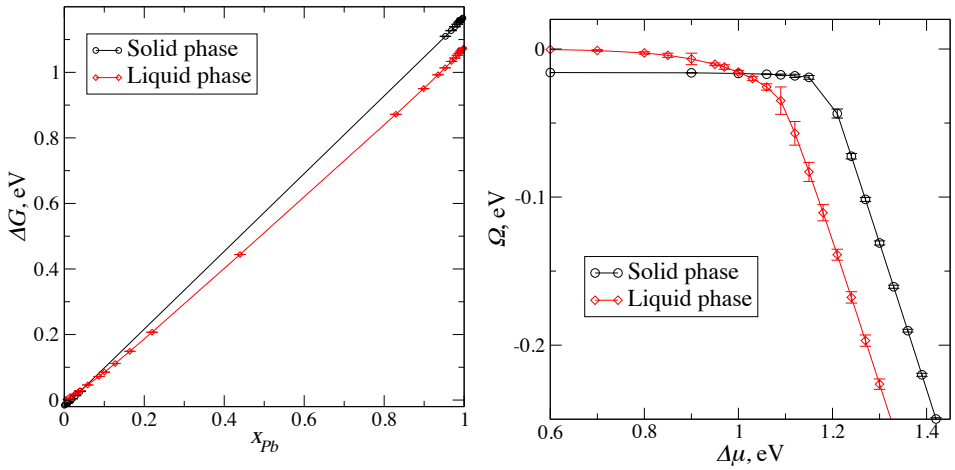

Figure 8.4: (a) Free energies of the system and (b) semigrand potential liquid and solid phases.

Several problems were found when the CTC was applied at lower temperatures. The first issue found was that around 1100 K, it was not possible to have Cu as a supercooled liquid, the Cu was fully crystallized. This fact leaded to propose a new integration scheme to calculate the reference Gibbs free energies as shown in Fig. 8.5. This

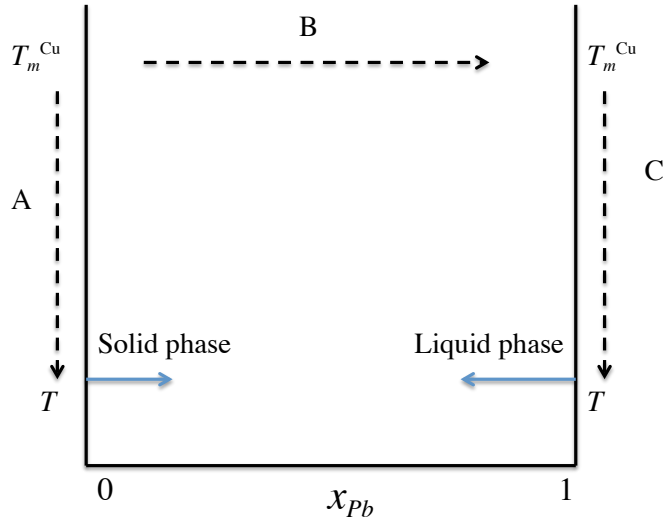

Figure 8.5: Thermodynamic scheme to calculate the references Gibbs energies for the solid and liquid in the ΔG versus x_{Pb} plot.

scheme to calculate the Gibbs energies of the solid and liquid of the pure components is as follows:

A) Calculate the Gibbs energy of Pure Cu solid at the desired temperature T, from Gibbs-Helmholtz: $G^S_{Cu}/T = \int_{T_{mCu}}^{T} H^S_{Cu}/T^2 dT$. This point served as a reference to the solid phase.

B) At the melting point of Cu, calculate the change in Gibbs energy associate when x_{Pb} changes from 0 (pure Cu) to 1 (pure Pb) in the liquid phase: $G^L_{Pb} = G^o_{Pb} + \int_0^1 \Delta\mu dx_{Pb}$

C) From the previous state at integrate to T to obtain the Gibbs energy for the liquid:$G^{oL}/T = G^L_{Pb} + \int_{T_{mCu}}^{T} H^L_{Pb}/T^2 dT$. This point was used as a reference for the liquid phase.

These reference points were expected to facilitate the integration of the Gibbs energy curves at 750 K when integrating the changes in composition. However, it was extremely unfavorable to make insertions of Pb atoms in the crystal Cu at 750 K, therefore

the assumption of pure Cu in the solid phase was taken. Nevertheless, the liquid phase became severely segregates when the chemical potential changed, see Fig. 8.6, and the integration of $\Delta G(x_{Pb})$ was not possible. After all these efforts, we concluded that the CTC was not sufficiently precise to predict the equilibrium composition at 750 K as the CTC was predicting pure crystal Cu and pure liquid Pb, albeit with large errors.

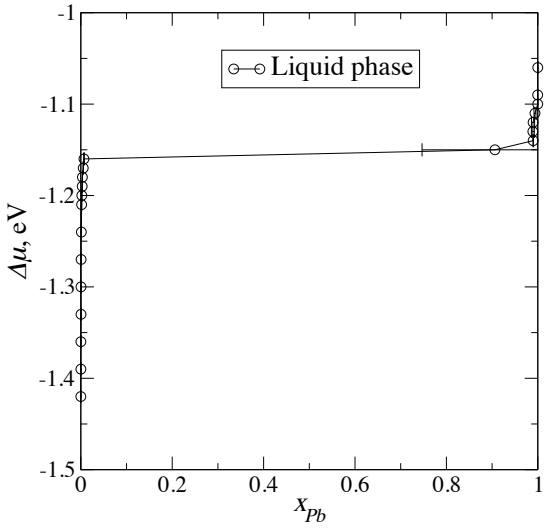

Figure 8.6: $\Delta\mu \; vs \; x_{Pb}$ liquid at 750K as this plot illustrated the severe segregation in the system; the liquid was either almost pure Cu or Pb.

8.1.3 MD equilibrium

Because of the difficulties encoutered in Sections 8.1.1 and 8.1.2 , yet another method was applied. Using and MD NPT, the Cu(111)/Pb interface at 625 K was heated to 750 K and the interface was equilibrated. The system reached equilibrium after 34.5 ns, and it was run for additional 4.5 ns to collect averages. The last 4.5 ns were used to get average Cu concentration in the bulk liquid, thus the $x^L_{Cu} = 0.027(1)$ was obtained. In the following section, this equilibrium composition are used characterize the interface at 750 K. At 625 K , as discussed earlier, we assume complete segregation.

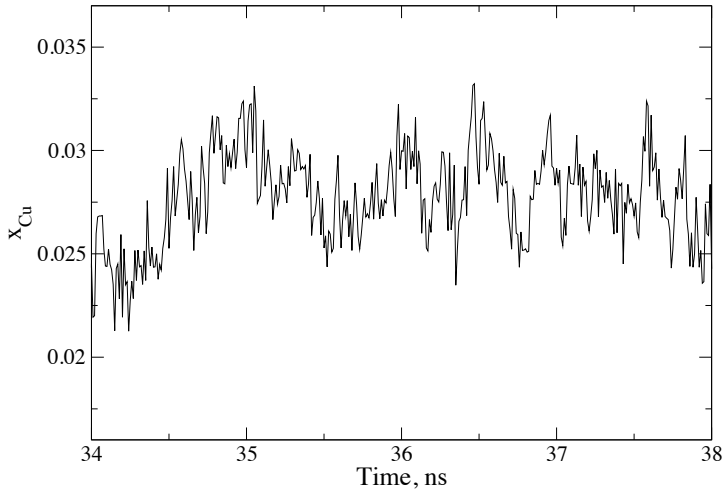

Figure 8.7: Final nanoseconds of the MD simulation at 750K used to collect block averages, to obtain $x_{Cu} = 0.027(1)$.

8.2 Interface characterization at 625 K

Using the definitions presented in Chapter 7, we characterized the Cu-Pb crystal liquid interface using Cu in (111) and (100). Fine-scale density profiles as well as filtered coarse-grained profiles of stress and energy are shown in Figs. 8.8(a) and 8.8(b), for the Cu(111)/Pb and Cu(100)/Pb interfaces, respectively. The density profiles, $\rho_{\mathrm{Cu}}(z)$ and $\rho_{\mathrm{Pb}}(z)$, for both interfacial orientations show periodic oscillations in the bulk Cu crystal, corresponding to the (111) or (100) lattice planes an FCC crystal, as well as the characteristic ordering of the liquid (Pb) structure at the interfacial plane, which rapidly decays to the bulk liquid Pb density. Beyond these commonalities, the density profiles show significant orientation dependence. For the (100) interface [Fig. 8.8(b)] the copper and lead density peaks at the interface overlap in the first layer of the solid, indicating significant alloying in the interface. The composition of this first layer is found to average 47$\pm$1% Pb. No interfacial alloying is seen in the (111) interface. This interfacial alloying for the Cu(100)/Pb interface was also observed previously in simulations of

the spreading kinetics of liquid Pb on a crystalline Cu surface at at 700 K [30]. Interfacial alloying has been previously reported experimentally for submonolayer coverages of Pb on both (100) and (111) Cu surfaces [112, 113]. In these experimental studies, which involve the vapor deposition of Pb at temperatures below the melting point of Pb, the interfacial alloying was seen only at low surface coverage. At higher coverages [>37.5% for (100) and >20% for (111)], a non-alloyed ordered Pb surface layer is observed. The higher threshold coverage for the Cu(100) surface is an indication that the driving force for interfacial alloying is greater for (100) than for (111), which is consistent with our observation of interfacial alloying in (100), but not (111) Cu/Pb solid-liquid interfaces.

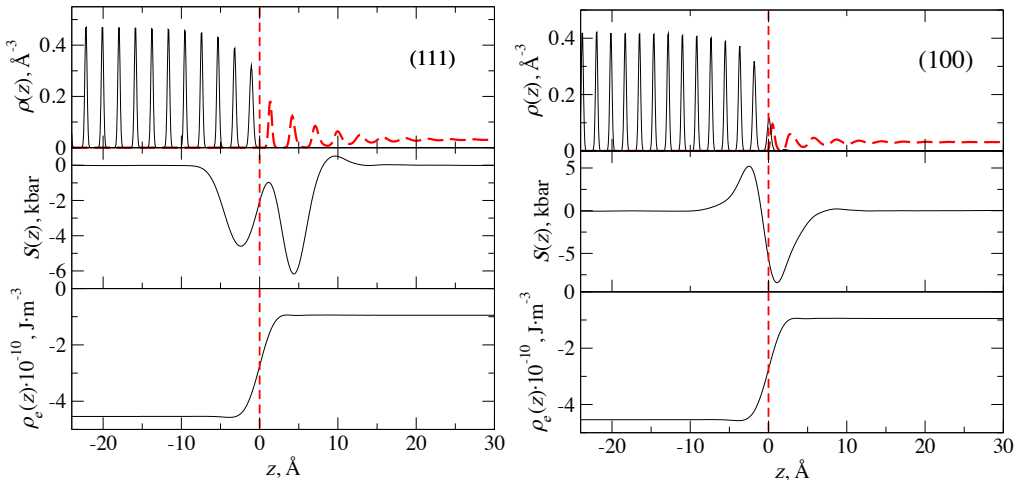

Figure 8.8: Density, stress ad potential energy profiles at 625 K, for the (111) and (100) interfaces. The position of the dividing surface ($z = 0$) is chosen such that the interfacial excess of Cu atoms is zero.

Although no interfacial alloying is seen in the Cu (111)/Pb interface, this interface exhibits significantly more pronounced structure in the Pb density profile extending into the bulk liquid than is seen on Cu (100). Figs. 8.9 and 8.10 show that this en-

hanced structure is due to the formation of a well-defined "wetting" layer of a (111) oriented Pb crystal approximately 2 lattice planes in thickness. As we are above the melting point of Pb, this is evidence of "prefreezing" in this system, similar to that observed in simulations of hard-spheres at a hard wall [18, 20] and recent experiments on Al_2O_3/Al solid-liquid interfaces [29]. Fig. 8.9 shows 2-dimensional densities and Fourier structure factors for a lattice plane deep within the bulk Cu crystal and for the last two layers of the Cu crystal at the interface. Fig. 8.10 shows the same plots for the first two Pb peaks after the interface and for a 2-d cut deep within the bulk liquid region of Pb .These plots, together with the density profiles, show no significant deformations in the Cu crystal structure as the interface is approached, aside from an increase in the mean-squared displacements (Debye-Waller factor) evident in the Cu density peaks. From the density profiles, we observe a slight increase in the Cu interplane spacing in both interfacial orientations, changing for (111) from 2.11Å to 2.14Å for the last two Cu peaks and from 1.89Å to 1.91Å in (100).

The 2-d structure factors for the first two Pb layers (Fig. 8.10) indicate a 2-d hexagonal ordering in these planes that is rotated slightly relative to the underlying Cu lattice - by an angle of about 6°. Fig. 8.11 shows a snapshot of the adjacent Cu and Pb layers at the Cu (111) interface. The ordered Pb "prefreezing" layers form a 6×6 R6° structure [113] relative to the underlying (111) Cu surface. We have analyzed such snapshots for systems with a wide range of cross-sectional areas and the 6×6 structure is seen in all but the very smallest of systems, indicating that it is a robust structure and not an artifact of the simulation size. This structure is in contrast to the (4×4) structure seen in experiments [113] and simulations [114] on expitaxially deposited Pb on Cu below the melting point of Pb. The prefreezing layers of Pb have a nearest neighbor distance of 3.43Å, which represents a 1.9% compression with respect to that of the (superheated) Pb lattice at 625 K. In their study of the spreading kinetics of liquid Pb droplets on (111)

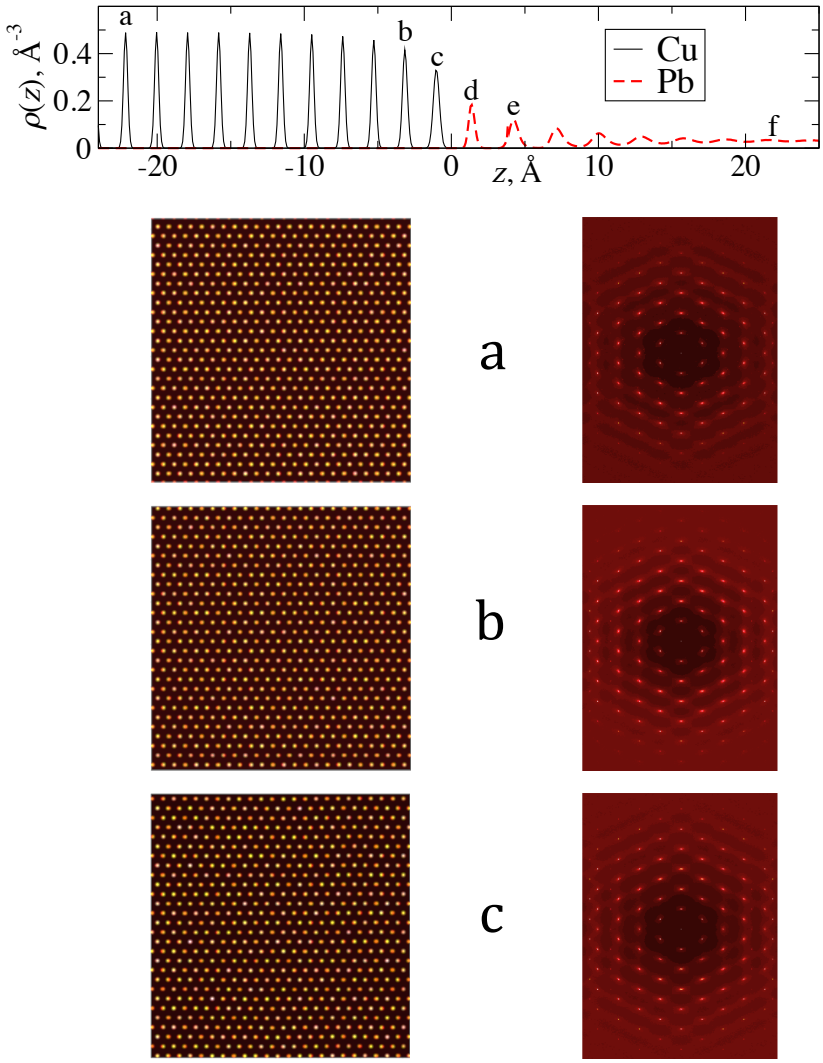

Figure 8.9: 2-D density (left) and Fourier structure factor (right) plots for three planes perpendicular to the Cu(111)/Pb interfacial plane at 625 K: (a) a plane deep into the bulk Cu crystal, (b and c) the two planes closest to the interface –the position of these planes is illustrated in the density profile reproduced at the top of the figure.

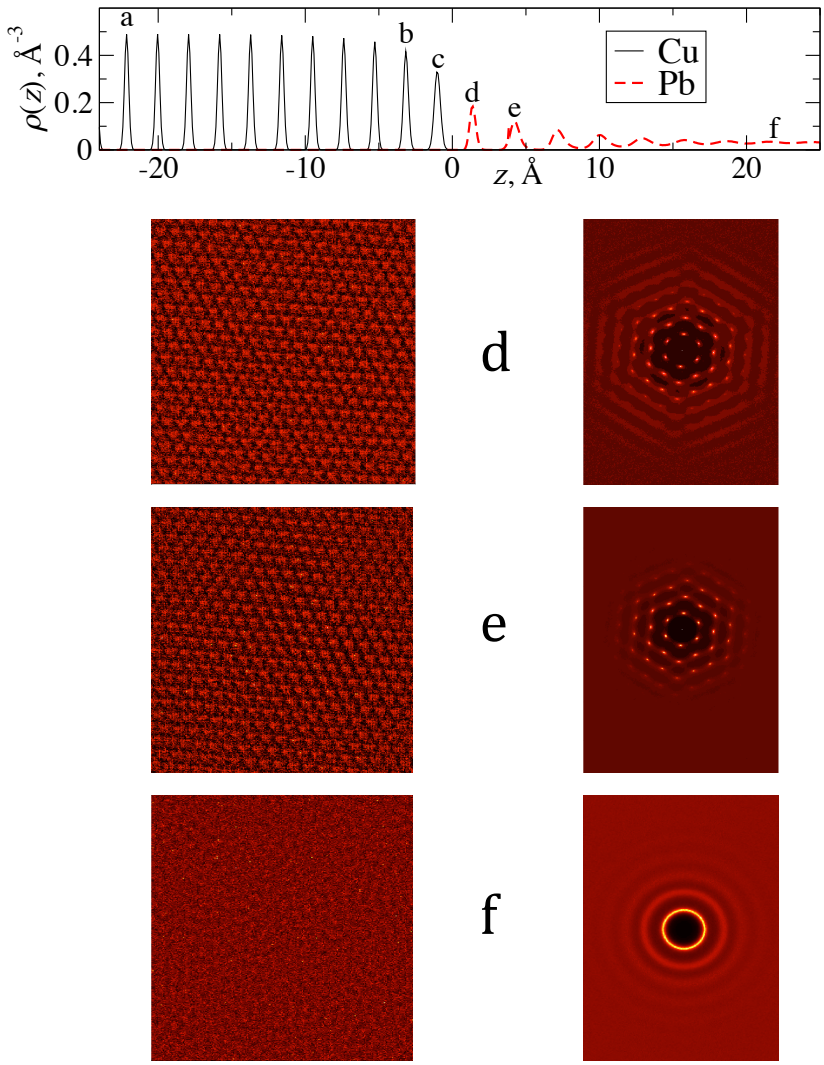

Figure 8.10: 2-D densities (left) and Fourier structure factors (right) plots for three planes perpendicular to the Cu(111)/Pb interfacial plane at 625K K: (d and e) the first two planes Pb planes adjacent to the interface, (f) a plane deep into the Pb liquid bulk –the position of these planes is illustrated in the density profiles reproduced at the top of the figure.

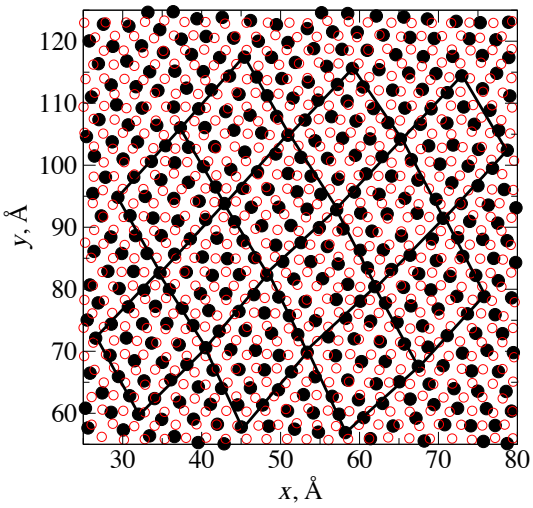

Figure 8.11: A snapshot from the simulation of the Cu(111)/Pb solid-liquid interface showing the first Cu (open circles) and Pb (filled circles) planes adjacent to the interfacial dividing surface. The lines illustrate the (6×6)R6° structure of the Pb prefreezing layer.

and (100) substrates, [30] Webb, *et al* also observed significant structural enhancement of the Pb density profile peaks on the Cu (111) surface over that seen on Cu (100), although they did not analyze the structural origin of these peaks. They also observe an early emerging thin precursor film (or foot) about 2 atomic planes in thickness that advances quickly in front of the main body of the spreading liquid Pb droplet on the (111) Cu surface. Although not discussed in Ref. [30], this precursor film was observed to be crystal-like in structure, [31] which, combined with our results, gives a three phase picture of the Pb/Cu(111) interface. That is, the bulk liquid Pb wets a thin prefreezing film of crystalline Pb, which in turn wets the Cu(111) substrate. From the droplet experiments we can conclude that the spreading kinetics of the crystalline Pb film on Cu(111) is considerably faster than that for liquid Pb on the crystalline Pb prewetting film.

The stress profiles in Figs. 8.8(a) and 8.8(b) show zero stress in both the bulk liquid

and solid. The absence of stress in the bulk solid is an important indicator that the interface has been properly equilibrated under hydrostatic conditions. The interfacial stress in the Cu (111) interface (Fig. 8.8(a)) has an unusual double peak structure that has not been seen in previous structural studies on model one- and two-component interfaces [107, 115, 116], where a single negative peak is typically observed for (111) orientations. This is likely explained by the fact that this interface should be thought of as two interfaces - a solid-solid interface between the Cu(111) and Pb(111) prefreezing layer and a solid-liquid interface between the prefreezing layer and liquid Pb. The excess stresses, τ, for the (111) and (100) interfaces are –0.44(3) and –0.135(2) J m^{-2}, respectively, indicating that both interfaces are under compression. (Recall, that, unlike for liquid-vapor interfaces, excess interfacial free energy for a solid-liquid interface is not the same as the surface tension, so that compression does not imply a negative interfacial free energy.) For the excess interfacial energy, e, we obtain –0.250(2) and 0.363(5) J m^{-2} for the (111) and (100) interfaces, respectively. We observe that the excess stresses and energies determined here are highly anisotropic, a property that has also been recently reported for these quantities for solid-liquid interfaces in single-component Cu [109] and Lennard-Jones systems [85]. The excess stress, τ, and energy, e, can be used to determine changes in the interfacial free energy, γ, as a function of temperature using Gibbs-Cahn integration [84, 85]

$$\frac{1}{A}\,\frac{d(\gamma A/T)}{dT} = -\frac{e}{T^2} + \frac{\tau}{AT}\,\frac{dA}{dT} \tag{8.9}$$

Finally, to understand the transport properties in the interfacial region we have calculated the diffusion constant profiles for both the Cu (100) and (111) orientations. To determine the diffusion profile we calculate the MSD (see previous section for details) out to 10 ps, which is sufficiently long to be within the diffusive regime, but short

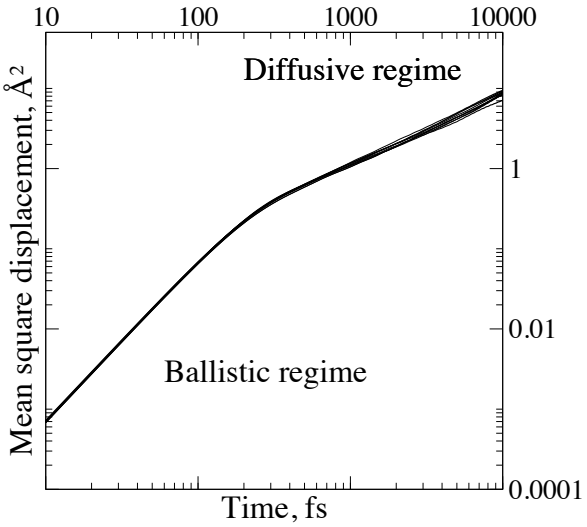

Figure 8.12: Mean squared displacements calculated for several time origins for a bin corresponding to the fifth Pb density peak from the Cu(111)/Pb solid liquid interface.

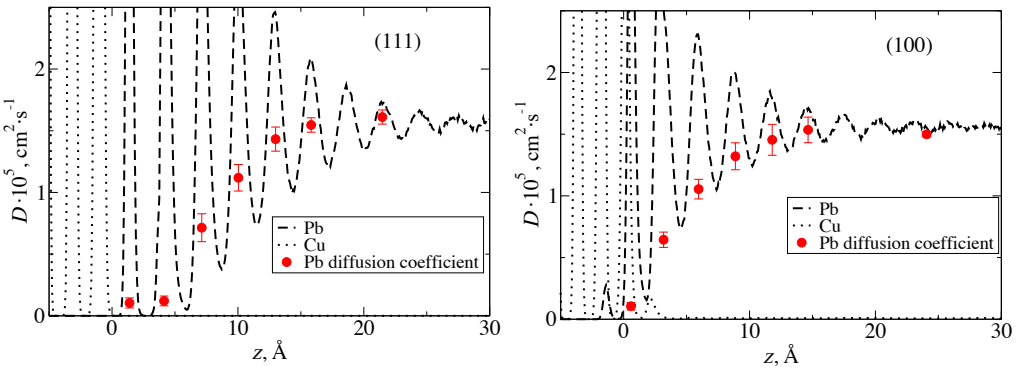

(a) 111 (b) 100

Figure 8.13: Diffusion coefficient profiles for the (111) and (100) Cu-Pb interface at 625 K. For clarity, the corresponding Cu and Pb density profiles are shown.

enough that the atoms do not travel more than one bin spacing in the z direction. As an example, we plot in Fig. 8.12 the MSD for several time origins for a bin corresponding to the 5th peak of the liquid Pb density profile (about 13Å from the interfacial plane). From these MSD plots, the diffusion coefficients were calculated for the first six layers of the Pb liquid adjacent to the interface as well as for the bulk Pb liquid using Eq. 7.7. Figs. 8.13(a) and 8.13(b) show the diffusion constant profiles for the (111) and (100) crystal orientation, respectively. In the (100) profiles we observe the diffusion constant is essentially zero in the first Pb layer (which corresponds to the surface-alloyed crystalline layer) followed by a monotonic increase to the bulk value over a distance of about 10Å. However, for the (111) Cu orientation, the diffusion coefficients for the first two prefreezing layers adjacent to the interface are very close to zero, which is consistent with the observed crystalline structure. Starting with the third layer the diffusion constant increases monotonically to the bulk value over about 10Å. In both the (111) and (100) interfaces, the diffusion constant reaches its bulk value after about 5 layers from the final crystalline plane.

8.3 Interface characterization at 750 K

Following the protocol introduced in the previous section, the results of characterization at 750 K for the (111) and (100) interface are presented. Here, the density, stress and potential energy profiles are shown in Fig. 8.14(a) and Fig. 8.14(b) respectively. The profiles for (100) showed no qualitative changes, but for the (111) profile, significant difference were seen. For the (111) interface, the density profile showed Cu atoms in the liquid closed to the interface, and the double peak observed at 625 K in teh stress profile has disappeared. For the excess interfacial energy, e, we obtain –0.360(3) and –0.261(4) J m^{-2} for the (111) and (100) interfaces, respectively. The excess stresses, τ, for the

(111) and (100) interfaces are -0.47(3) and -0.17(1) J m^{-2}, respectively, indicating that both interfaces are under compression as well as the ones at 625 K.

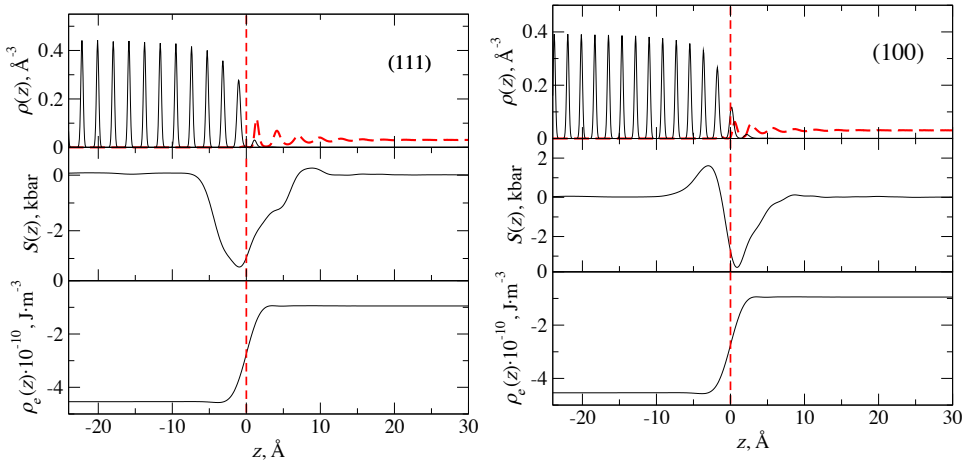

Figure 8.14: Density, stress ad potential energy profiles at 750 K, for the (111) and (100) interfaces. The position of the diving surface ($z = 0$) is chosen such that the interfacial excess of Cu atoms is zero

The variation in the stress profile was an indicator of the structural changes taking place at this temperature. While the (111) Cu the 2-d density profiles and structure factor showed no change, see Fig. 8.16, the liquid Pb layers at interface presented less in-plane structure, see Fig. 8.17. The 2-d density Pb profiles at the layers adjacent to the interface showed some hexagonal structure (the first Pb layer) but the arrangement showed considerable defects. These defects are correlated with the second layer that is, the vacancies in the first Pb layer are interstitials in the second layer. The FT analysis did not show the previous well-defined hexagonal arrangement in the first two Pb layers, Fig. 8.17, it presented a liquid like structure with some ordering. This ordering is only weakly detectable in the high intensity peak of the inner ring of the first Pb layer, and this feature almost disappeared in the second Pb layer. The lack of crystalline structure

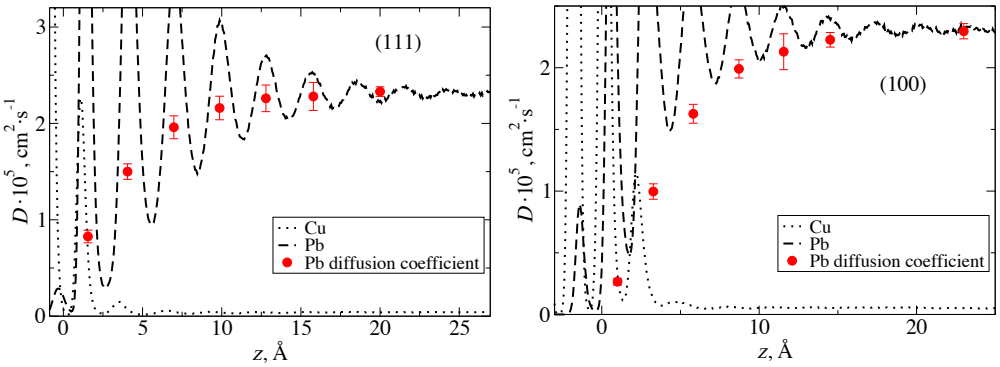

(a) (111) (b) (100)

Figure 8.15: Diffusion coefficient profiles for the (111) (left) and (100) (right) Cu-Pb interface at 750 K. For ease of comparison, the corresponding Cu and Pb density profiles are shown.

was an indicative of the highly dynamic behavior of layers, demonstrating a liquid-like nature.

The diffusion profiles, Fig. 8.15(a) and Fig. 8.15(b), illustrated this increment in the mobility. The values of the diffusion coefficient for the first two layers Pb on the Cu (111) interface were almost one order-of-magnitude higher than those reported at 625 K, this is an indicator that the Pb atoms adjacent to the interface are more liquid like. Also note that the values for the diffusion coefficient of Pb on Cu (111) in the adjacent layer to the interface are higher than those for the (100) interface. The (100) profile had the same qualitative behavior, the main difference is just the natural increase of the diffusion constant with increasing the temperature. All these observations are evidence that the wetting layer showed at 625 K is vanishing at higher temperatures. In the next section, cooling experiments are presented to investigate the consequences of the surface alloying and prefreezing in crystal formation.

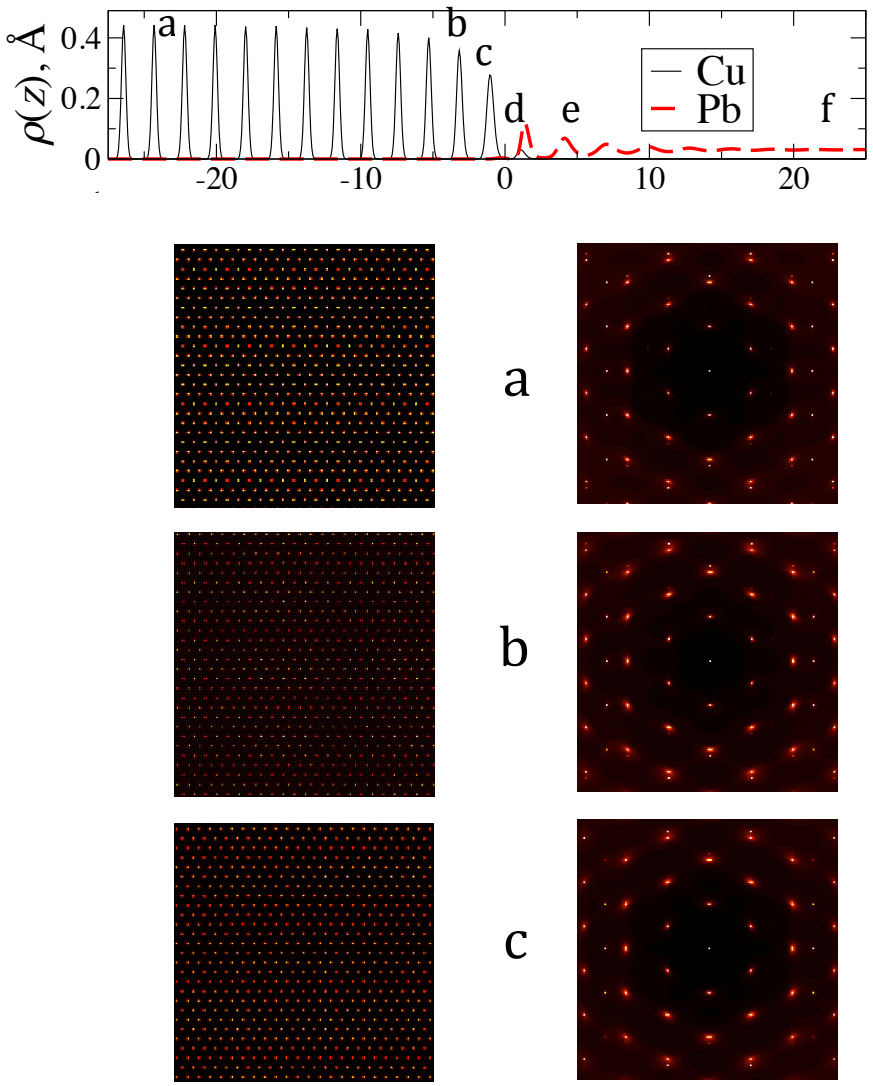

Figure 8.16: 2-D densities (left) and Fourier structure factors (right) for three planes perpendicular to the Cu(111)/Pb interfacial plane at 750 K: (a) a plane deep into the bulk Cu crystal, (b and c) the two planes closest to the interface the position of these planes is illustrated in the density profiles are reproduced at the top of the figure.

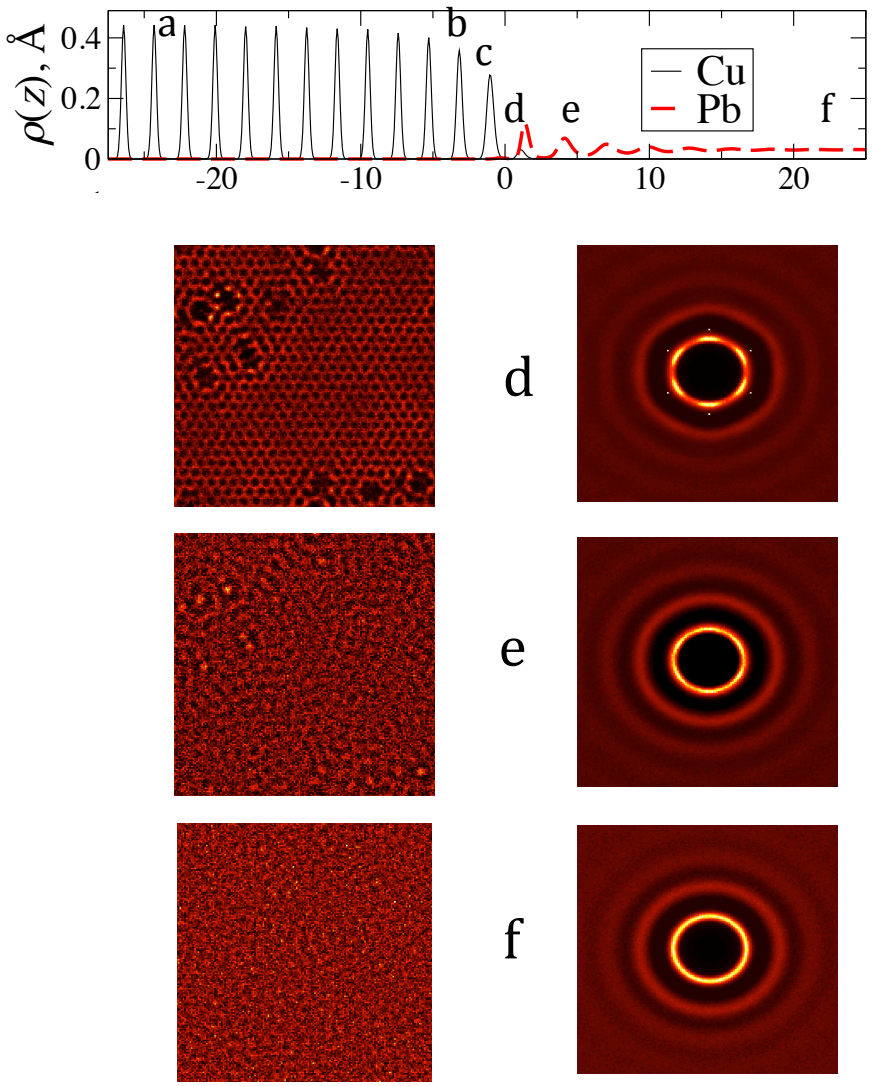

Figure 8.17: 2-D densities (left) and Fourier structure factors (right) for three planes perpendicular to the Cu(111)/Pb interfacial plane at 750 K: (d and e) the first two planes Pb planes adjacent to the interface, (f) a plane deep into the Pb liquid bulk the position of these planes is illustrated in the density profile reproduced at the top of the figure.

8.4 Effect of the structure on nucleation

As presented in Section 8.2, two types of interfacial structures were observed at 625 K: prefreezing and surface alloying for the (111) and (100) orientation, respectively. Prewetting phenomena, such as the prefreezing seen here, is generally associated with barrierless heterogeneous nucleation. This was observed in the hard-sphere/hard-wall system, where the thickness of the prefreezing layer diverged as the freezing density was approached from below [17,18]. The studies presented in this section gives a semi-quantitative analysis of the effect of the interfacial structures on nucleation orientation in Cu/Pb. In particular we examine the effect of prefreezing [Pb on Cu (111)] and surface alloying [Pb on Cu (100)] on heterogeneous nucleation. First the Cu (111) interface is studied using order parameters to determine the width of the Pb crystal layer with respect time. The section concludes with an examination of heterogeneous nucleation of Pb on Cu (100).

8.4.1 (111) prefreezing layer

Intensive simulations were performed to investigated the impact of the (6×6)R6° prefreezing on heterogeneous nucleation. A series of $NPA_{xy}T$ simulations taking a configuration equilibrated at 625 K as a starting point were cooled down in decrement of 5 K and run for 5 ns, and the configurations were recorded. Heterogeneous nucleation was observed between 595 K and 590 K. Within this range, further simulations were carried out in decrements of 1 K. It was found that at 592 K both interfaces (left and right) nucleated, see Fig. 8.18. In order to have a more quantitative idea of the extend of the structure, the 2-d order parameter described by Davidchack and Laird [107] was computed. Given that at 625 K the structure was hexagonal, a q_6 parameter was implemented:

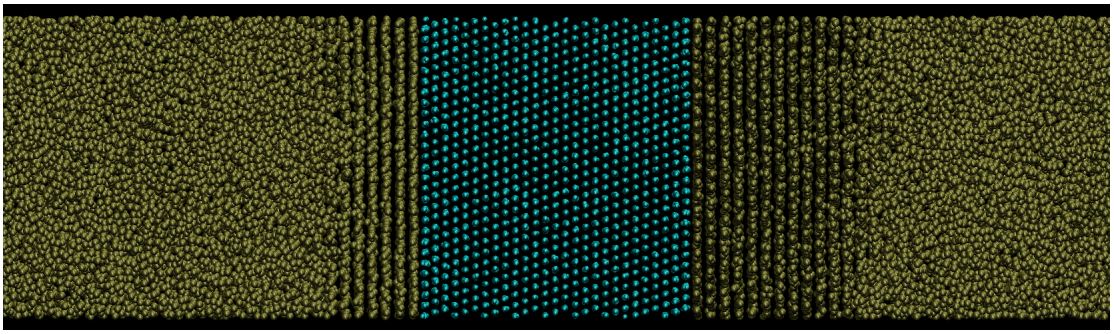

Figure 8.18: Cu(111)-Pb interface at 592 K after a 5ns simulation.

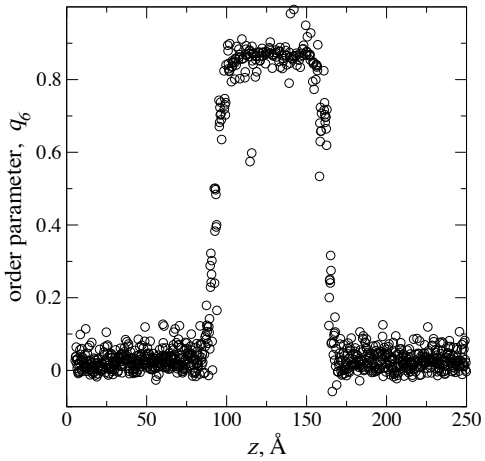

Figure 8.19: Order parameter taken from the starting configuration at 592 K.

$$q_6 = \left\langle \frac{1}{N} \sum_{i,j,k} \cos[6\theta_{xy}(i,j,k)] \right\rangle \tag{8.10}$$

here the sum over i, j, k represents the angle formed by the nearest neighbors in the same bin, θ_{xy} is the angle between r_{ij} and r_{ik} projected in the xy plane. This parameter varies from near 0 for a liquid and 1 for a perfect FCC crystal. A representative snapshot of this calculation is shown in Fig. 8.19. Once the order parameter was calculated for each of the recorded configurations, each interface was fitted to a hyperbolic tangent [117]:

$$f(z) = a + b \tanh(z - C_{pos})/d \tag{8.11}$$

here a, b, C_{pos} and d are fitting parameters, from these, the parameter describing the position of the interface is C_{pos}. In this way, the position of the interface was monitored for 10 simulations.

From configurations recorded at 600 K, 10 different staring points were used to monitor the cooling of the system; 0.5 ns were used to quench the system and 4.5 ns were used to follow the growth of the Pb crystal. From these simulations, the position of the interface is obtained and converted to Pb crystal thickness, then thickness of the Pb crystal is plot versus time, see Fig. 8.20. Once the thickness of the Pb crystal is found, a linear regression of the thickness versus time is performed to calculate the intial growth rate and nucleation time. The results of this analysis can be shown in Fig. 8.21(a) and Fig. 8.21(b). The growth rate ranged from 0.9 m s^{-1} to 2.2 m s^{-1}, and the nucleation times from 1 ns to 4.5 ns. These finding are in contrast with previous reports for hard spheres [17, 18], which indicated barrierless nucleation as discussed at the beginning of this section. The simulations performed here are below the Pb melting point (618 K), and full crystallizations did not occur until 592 K (over the time scale of the longest simulation). These findings suggest the existence of a nucleation barrier, that we believe that is due to fact the Pb prefreezing layer does not have the same lattice constant than regular bulk solid Pb, the prefreezing layer of Pb is compressed 1.9% with respect to a super heated Pb lattice at 625K. Further investigation is required to make more definitive statement, but qualitatively the existence of a nucleation barrier is predicted.

8.4.2 Cu(100)/Pb surface alloying and nucleation

Cooling experiments were performed on the Cu(100)/Pb interface. First, a $NPA_{xy}T$ simulation at 545 K showed no signs of crystallization over a run of 65.5 ns. Given

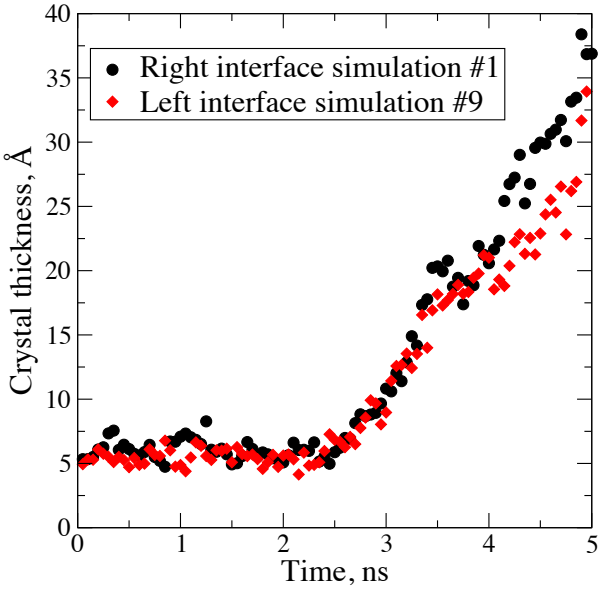

Figure 8.20: Pb crystal thickness over time for two starting points.

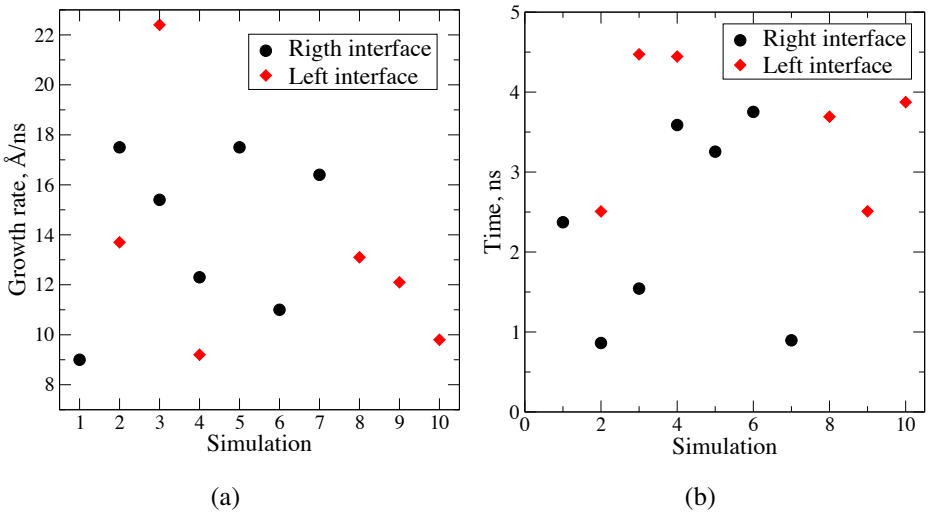

Figure 8.21: Linear regression results: (a) growth rates, (b) nucleation times.

this result a configuration from this simulation was taken and cooled down to 450 K and run at $NPA_{xy}T$. In this system, nucleation of a hexagonal lattice was observed at this temperature after 10.15 ns. A series of snapshots are presented in Fig. 8.22, from here it is illustrated how the crystal growth takes place. In this crystal orientation, a Pb semi-sphere (or cap) nucleated on the top of the Cu (100), which is evidence that the Pb crystal only partially wets the Cu (100) surface. The elapsed time from the nucleation of the cap until the crystal growth layer wise is approximately 0.15 ns. Meanwhile, the crystal growth observed in the (111) occurred by the formation of complete layers starting from the preefrezing layer. This finding show a clear difference in the mechanisms of heterogeneous nucleation. On one hand, the prefreezing Pb layer on (111) Cu promotes the crystal growth by layers, once a nucleation barrier is overcome, and on the other hand the formation of the hemispherical cap on Cu (100) is an indicator of partial wetting. The time scale of the crystal growth promoted from partial wetting is much larger (10ns) and requires a further decrease in the temperature (450K) in comparison to the crystal growth by layers observed on Cu (111); times as early as 5 ns and 595 K. We are aware of the qualitative nature of these statements, and further simulations are required to achieve quantitative ones. However, a clear difference was found in the crystal growth, showing that the prefreezing layers enhanced the heterogeneous nucleation, meanwhile the surface alloying had less impact on the crystal formation. In the next chapter a summary of the results and recommendations are presented.

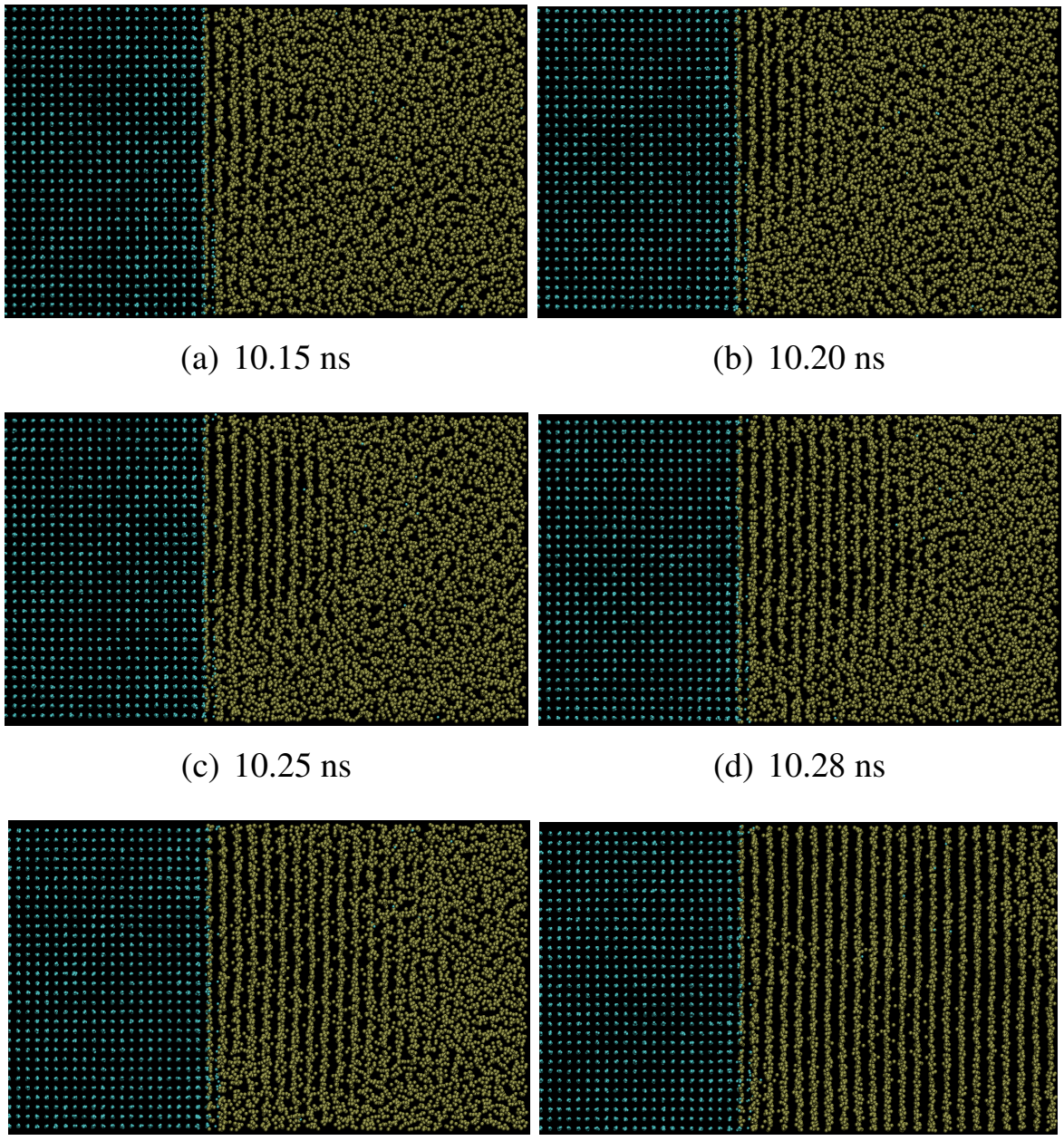

(a) 10.15 ns (b) 10.20 ns

(c) 10.25 ns (d) 10.28 ns

(e) 10.30 ns (f) 10.40 ns

Figure 8.22: Snapshot from the Cu(100)/Pb interface at 450 K illustrating the crystal formation

Chapter 9

Summary and conclusions

In this work we have examined the structure, thermodynamics and transport properties, using atomistic simulations, of two models of chemically heterogeneous solid-liquid interfaces: an idealized model (repulsive soft spheres against a potential wall), and a metal alloy interface (Cu-Pb). In both systems, interfacial prefreezing (crystal formation above the melting point of the fluid) was observed and this prefreezing was observed to promote heterogeneous nucleation.

In our study of inverse-power repulsive soft spheres, we found that the soft-sphere liquid showed prefreezing at the wall surface. Similar behavior was previously observed in hard spheres [17–20, 27, 28, 94], however, to our knowledge, this work is the first to report prefreezing for soft spheres, see Part II. The prediction of prefreezing is based on the calculation of interfacial free energies wall-crystal (γ_{wc}) and wall-fluid (γ_{wf}) using a variant of the cleaving wall method. Using the calculated γ_{wc} and γ_{wf}, together with γ_{cf}, previously computed [79], the tendency to prefreeze was quantified by the wetting angle formed between the metastable crystal phase on the wall and the soft-sphere fluid. We found that all closest-packing orientations [(111) FCC and (110) BCC]

developed a crystalline wetting layer, known as prefreezing because it occurs above the melting point of the material. The propensity of the system to develop preefrezing increased as the softness of the sphere increased (low n values). On the other hand, less packed densely orientations [(100) FCC and (100) BCC] showed partial wetting and no prefreezing, and the extent of the wetting was decreasing as the sphere softness increased.

In order to evaluate the accuracy of the results obtained with the CWM, the γ_{wf} was calculated for $n = 8$ using an independent method – Gibbs-Duhem (GD) integration. Both methods were shown to give identical results, this independent computation gives us confidence in our predictions regarding prefreezing.

In Part III of this dissertation, the Cu-Pb solid-liquid interface was modeled using an Embedded Atom Model (EAM) and molecular simulations. A detailed atomic-level simulation of the structure, energetics and transport properties of the planar Cu/Pb solid-liquid interface in equilibrium was performed at a several temperatures (625K and 750K) above the melting point of Pb and for two Cu crystal orientations [(111) and (100)]. Among the most relevant findings are that the Cu(100)/Pb interfaces presents surfaces alloying and the Cu(111)/Pb exhibits a prefreezing layer of Pb crystal at 625 K. It was also observed that both interfaces have a nucleation barrier to heterogeneous nucleation below the T_m for Pb, but this barrier is considerable smaller for the Cu(111) interface than for the Cu (100) interface. Also the detalied mechanism for heterogeneous nucleation is different for the two interfaces.

In determination of the equilibrium composition were determined, the Cu-Pb phase diagram showed significant non-ideal behavior. Because of this, the Gibbs-Duhem (GD) integration and common tangent construction (CTC) were insufficient to pre-

dict the equilibrium composition at 750 K, see Chapters 3 and 8. Both methods were adapted to cope with the necessities on a highly-non-ideal phase diagram, nevertheless, the non-ideality of the system was too high for the methods to be handled. Finally, the Cu-Pb equilibrium composition was determined, using long MD simulations to equilibrate the system, to be $x_{Cu}^{L} = 0.027(1)$ in the liquid phase at 750 K assuming pure Cu in the solid phase.

At 625 K, our analysis of the structure showed significant qualitative differences in the interfacial structure depending upon the Cu crystal orientation: (100) or (111). For the Cu (100) interface, the final crystalline layer exhibited alloying with a interfacial composition of about 47% Pb. This interfacial alloying is consistent with observations made in earlier simulations on the spreading kinetics of Pb droplets on (100) Cu surfaces. [30] In contrast, no interfacial alloying is observed in the Cu (111) interface. Instead, the first two peaks in the density profile of Pb are observed to be crystalline, indicating *prefreezing* - the formation of a thin layer of Pb crystal between the Cu surface and the liquid Pb bulk. These 2-d "prefreezing" layers are hexagonal with a lattice spacing that is 33% larger than the underlying Cu (111) planes and rotated by an angle of 6°. The existence of this prefreezing layer is evidence that the interfacial free energy between Cu(111) and liquid Pb is greater than the energy cost of forming a Cu(111)/compressed-Pb(111) *and* a compressed-Pb(111)/Pb(*l*) interface. This prefreezing layer is likely the origin of the thin flim (or "foot") observed to advance in front of the main droplet body in simulations of the spreading kinetics of Pb droplets on Cu(111) [30].

At 750K, the Pb layers adjacent to the Cu (111) interface presented reduced 2-d in-plane order compared with that at 625 K. This was shown in the FT profiles, which

presented a mostly a liquid-like structure with very little remaining of the crystalline layer observed at 625 K. The change towards a more liquid like behavior was also observed in the diffusion profile, which showed significant mobility, not observed at 625 K, of the Pb layers closer to the Cu (111) interface.

Finally, cooling simulations were performed to further elucidate the connection between the observed interfacial structures and the solidification kinetics of this system when cooled below the Pb melting point. We found that the surface alloying of the (100) interface nucleated at much lower temperatures and longer time scales than the Pb prefreezing layer in the (111) interface. Significant difference in the nucleation mechanisms of these two structures was observed, the crystal (111) grew layerwise as opposed to the semi-spherical cap formed at the (100) interface. This difference in nucleation mechanisms, to our knowledge, was never reported before. Despite enhanced nucleation at the Cu(111) interface, the heterogeneous nucleation differed from that reported previously for the hard-sphere fluid at a hard wall [18], in which the thickness of the prefreezing layer diverged as the melting point was approached indicating barrierless nucleation in the presense of the prefreezing layer. In the Cu (111)/ Pb system the thickness of the prefreezing layer remained constant as the system was cooled below the T_m for Pb abs nucleation only occurred on the time scale of the simulation below 592K, which was 26 K below T_m A possible cause of the barrier is that the Pb prefreezing layer at the interface is compressed relative to bulk Pb.

Both models, the inverse-power soft spheres and the EAM Cu-Pb, showed the connection between atomistic interfacial properties and prefreezing. The crystalline layer formed above the melting point of the fluids showed to be influential in heterogeneous nucleation in both cases. In this way, the study of basic properties shed new light on

the atomistic underlying nature of macroscopic events such as wetting and nucleation.

Appendix A

Compilation of the cleaving wall method results for the inverse-power soft sphere fluid at a wall

Results for the cleaving wall method (CWM) for $n = 20, 12, 8$ and all the system sizes used.

Table A.1: Results obtained; wall/(111) FCC crystal, $n = 12$, $T^* = 0.473(2)$

L_z^*	N	Step	Work, $\frac{\epsilon}{\sigma^2}$ (forward direction)	Work, $\frac{\epsilon}{\sigma^2}$ (backward direction)
23.81	4860	1	0.188(1)	0.186(1)
47.62	9720	1	0.187(1)	0.189(1)
71.43	14580	1	0.186(1)	0.187(1)
23.81	4860	2	-0.523(1)	-0.523(1)
47.62	9720	2	-0.525(1)	-0.526(1)
71.43	14580	2	-0.528(1)	-0.528(1)

Table A.2: Results obtained; wall/(100) FCC crystal, $n = 12$, $T^* = 0.473(2)$

L_z^*	N	Step	Work, $\frac{\epsilon}{\sigma^2}$ (forward direction)	Work, $\frac{\epsilon}{\sigma^2}$ (backward direction)
23.81	4860	1	0.392(1)	0.392(1)
47.62	9720	1	0.390(1)	0.392(1)
71.43	14580	1	0.390(1)	0.390(1)
23.81	4860	2	-0.430(1)	-0.429(1)
47.62	9720	2	-0.328(1)	-0.329(1)
71.43	14580	2	-0.325(1)	-0.325(1)

Table A.3: Results obtained; wall/fluid, $n = 12$, $T^* = 0.473(2)$

L_z^*	N	Step	Work, $\frac{\epsilon}{\sigma^2}$ (forward direction)	Work, $\frac{\epsilon}{\sigma^2}$ (backward direction)
47.62	9720	1	0.503(2)	0.501(2)
71.43	14580	1	0.493(2)	0.408(2)
47.62	9720	2	-0.573(1)	-0.576(1)
71.43	14580	2	-0.570(1)	-0.575(1)

Table A.4: Results obtained; wall/(111) FCC crystal, $n = 20$, $T^* = 0.713(5)$

L_z^*	N	Step	Work, $\frac{\epsilon}{\sigma^2}$ (forward direction)	Work, $\frac{\epsilon}{\sigma^2}$ (backward direction)
47.62	9720	1	0.207(1)	0.208(1)
71.43	14580	1	0.206(1)	0.207(1)
47.62	9720	2	-0.421(1)	-0.422(1)
71.43	14580	2	-0.424(1)	-0.423(1)

Table A.5: Results obtained; wall/(100) FCC crystal, $n = 20$, $T^* = 0.713(5)$

L_z^*	N	Step	Work, $\frac{\epsilon}{\sigma^2}$ (forward direction)	Work, $\frac{\epsilon}{\sigma^2}$ (backward direction)
47.62	9720	1	0.457(1)	0.458(1)
71.43	14580	1	0.456(1)	0.457(1)
47.62	9720	2	-0.305(1)	-0.303(1)
71.43	14580	2	-0.300(1)	-0.299(1)

Table A.6: Results obtained; wall/fluid, $n = 20$, $T^* = 0.713(5)$

L_z^*	N	Step	Work, $\frac{\epsilon}{\sigma^2}$ (forward direction)	Work, $\frac{\epsilon}{\sigma^2}$ (backward direction)
47.62	9720	1	0.648(2)	0.649(2)
71.43	14580	1	0.643(2)	0.640(2)
47.62	9720	2	-0.504(1)	-0.462(1)
71.43	14580	2	-0.461(1)	-0.464(1)

Table A.7: Results obtained; wall/(111) FCC crystal, $n = 8$, $T^* = 0.284(1)$

L_z^*	N	Step	Work, $\frac{\epsilon}{\sigma^2}$ (forward direction)	Work, $\frac{\epsilon}{\sigma^2}$ (backward direction)
48.00	9720	1	0.176(1)	0.175(1)
71.43	13104	1	0.174(1)	0.175(1)
48.00	9720	2	-0.688(1)	-0.688(1)
71.43	13104	2	-0.690(1)	-0.690(1)

Table A.8: Results obtained; wall/(100) FCC crystal, $n = 8$, $T^* = 0.284(1)$

L_z^*	N	Step	Work, $\frac{\epsilon}{\sigma^2}$ (forward direction)	Work, $\frac{\epsilon}{\sigma^2}$ (backward direction)
48.00	9720	1	0.318(1)	0.317(1)
71.43	13104	1	0.315(1)	0.316(1)
48.00	9720	2	-0.542(1)	-0.540(1)
71.43	13104	2	-0.542(1)	-0.548(1)

Table A.9: Results obtained; wall/(100) BCC crystal, $n = 8$, $T^* = 0.284(1)$

L_z^*	N	Step	Work, $\frac{\epsilon}{\sigma^2}$ (forward direction)	Work, $\frac{\epsilon}{\sigma^2}$ (backward direction)
48.00	9720	1	0.504(1)	0.503(1)
71.43	13104	1	0.501(1)	0.502(1)
48.00	9720	2	-0.861(1)	-0.869(1)
71.43	13104	2	-0.858(1)	-0.868(1)

Table A.10: Results obtained; wall/(110) BCC crystal, $n = 8$, $T^* = 0.284(1)$

L_z^*	N	Step	Work, $\frac{\epsilon}{\sigma^2}$ (forward direction)	Work, $\frac{\epsilon}{\sigma^2}$ (backward direction)
48.00	9720	1	0.221(1)	0.219(1)
71.43	13104	1	0.221(1)	0.219(1)
48.00	9720	2	-0.665(1)	-0.670(1)
71.43	13104	2	-0.668(1)	-0.666(1)

Table A.11: Results obtained; wall/fluid, $\rho = 0.95$, $n = 8$, $T^* = 0.284(1)$

L_z^*	N	Step	Work, $\frac{\epsilon}{\sigma^2}$ (forward direction)	Work, $\frac{\epsilon}{\sigma^2}$ (backward direction)
48.00	9720	1	0.347(1)	0.345(1)
71.43	13104	1	0.344(1)	0.338(1)
48.00	9720	2	-0.614(1)	-0.617(1)
71.43	13104	2	-0.611(1)	-0.652(1)

Table A.12: Results obtained; wall/fluid, $\rho = 0.92$, $n = 8$, $T^* = 0.284(1)$

L_z^*	N	Step	Work, $\frac{\epsilon}{\sigma^2}$ (forward direction)	Work, $\frac{\epsilon}{\sigma^2}$ (backward direction)
48.00	9720	1	0.330(1)	0.329(1)
71.43	13104	1	0.330(1)	0.329(1)
48.00	9720	2	-0.556(1)	-0.569(1)
71.43	13104	2	-0.560(1)	-0.569(1)

Table A.13: Results obtained; wall/fluid, $\rho = 0.89$, $n = 8$, $T^* = 0.284(1)$

L_z^*	N	Step	Work, $\frac{\epsilon}{\sigma^2}$ (forward direction)	Work, $\frac{\epsilon}{\sigma^2}$ (backward direction)
48.00	9720	1	0.317(1)	0.315(1)
71.43	13104	1	0.312(1)	0.312(1)
48.00	9720	2	-0.494(1)	-0.496(1)
71.43	13104	2	-0.497(1)	-0.498(1)

Table A.14: Results obtained; wall/fluid, $\rho = 0.86$, $n = 8$, $T^* = 0.284(1)$

L_z^*	N	Step	Work, $\frac{\epsilon}{\sigma^2}$ (forward direction)	Work, $\frac{\epsilon}{\sigma^2}$ (backward direction)
48.00	9720	1	0.300(1)	0.301(1)
71.43	13104	1	0.296(1)	0.296(1)
48.00	9720	2	-0.437(1)	-0.438(1)
71.43	13104	2	-0.440(1)	-0.441(1)

Bibliography

[1] D.P. Woodruff, *The Solid-Liquid Interface*, (Cambridge University Press, London, 1973).

[2] W.A. Tiller, *The Science of Crystallization: Microscopic Interfacial Phenomena*, (Cambridge University Press, New York, 1991).

[3] J.M. Howe, *Interfaces in Materials*, (John Wiley & Sons, New York, 1997).

[4] W.D. Kaplan and Y. Kauffman, Annu. Rev. Mater. Res. **36**, 1 (2006).

[5] A.W. Adamson and A.P. Gast, *Physical Chemistry of Surfaces*, (Wiley-Interscience, New York, 1997).

[6] U.Bardi, Rep. Prog. Phys. **57**, 939 (1994).

[7] W.J. Huisman, J.F. Peters, M.J. Zwanenburg, S.A. deVries, T.E. Derry, D. Abernathy, and J.F. vanderVeen, Nature **390**, 379 (1997).

[8] H. Gabrisch, U. Dahmen, and E. Johnson., Microsc. Microanal. **4**, 286 (1998).

[9] H. Reichert, O. Klein, H. Dosch, M. Denk, V. Honkimaki, T. Lippmann, and G. Reiter, Nature **408**, 839 (2000).

[10] U. Landman, W.D. Luedtke, R.N. Barnett, C.L. Cleveland, M.W. Ribarsky, E. Arnold, S. Ramesh, H. Baumgart, A. Martinez, and B. Khan, Phys. Rev. Lett. **56**, 155 (1986).

[11] F.F. Abraham and J.Q. Broughton, Phys. Rev. Lett. **56**, 734 (1986).

[12] B.J. Jesson and P.A. Madden, J. Chem. Phys. **113**, 5935 (2001).

[13] J.J. Hoyt, M. Asta, and A. Karma, Phys. Rev. Lett **86**, 5530 (2001).

[14] R.L. Davidchack and B.B. Laird, Phys. Rev. E **54**, R5905 (1996).

[15] J.Q. Broughton and G.H. Gilmer, J. Chem. Phys. **84**, 5759 (1986).

[16] B.B. Laird and R.L. Davidchack, J. Phys. Chem. B **109**, 17802 (2005).

[17] D.J. Courtemanche and F. van Swol, Phys. Rev. Lett. **69**, 2078 (1992).

[18] M. Dijkstra, Phys. Rev. Lett. **93**, 108303 (2004).

[19] A. Fortini and M. Dijkstra, J. Phys.: Condens. Matter **18**, L371 (2006).

[20] B.B. Laird and R.L. Davidchack, J. Phys. Chem. C **111**, 15952 (2007).

[21] R.L. Davidchack and B.B. Laird, Mol. Phys. **97**, 833 (1999).

[22] M. Amini and B.B. Laird, Phys. Rev. B **78**, 144112 (2008).

[23] C.A. Becker, M. Asta, J.J. Hoyt, and S.M., J. Chem. Phys. **124**, 164708 (2006).

[24] C.A. Becker, D. Olmsted, M. Asta, J.J. Hoyt, and S.M. Foiles, Phys. Rev. Lett **98**, 125701 (2007).

[25] M. Asta, J.J. Hoyt, and A. Karma, Phys. Rev. B **66**, 100101 (2002).

[26] A. Van de Walle H. Ramalingam, M. Asta and J.J. Hoyt, Interface Sci. **10**, 149 (2002).

[27] D.J. Courtemanche and F. van Swol, Mol. Phys. **80**, 861 (1993).

[28] M. Heni and H. Løwen, Phys. Rev. E **60**, 7057 (1999).

[29] Y. Kauffmann, S.H. Oh, C.T. Koch, A. Hashibon, C. Scheu, M. Rhle, and W.D. Kaplan, Acta Materialia **59**, 4378 (2011).

[30] E. B.Webb III, G. S. Grest, and D. R. Heine, Phys. Rev. Lett. **91**, 236102 (2003).

[31] E. B.Webb III, Private communication; (2010)

[32] A. Ziemys, A. Grattoni, D. Fine, F. Hussain, and M. Ferrari, J. Phys. Chem. B **114**, 11117 (2010).

[33] J.A van Meel, D. Frenkel, and P. Charbonneau, Phys. Rev. E **79**, 030201 (2009).

[34] D. A. McQuarrie, *Statistical Mechanics*, (Harper and Row, New York, 1976).

[35] H.B. Callen, *Thermodynamics and an introduction to thermostatistics*, (John Wiley Sons, New York, 1987).

[36] D. Chandler, *Introduction to modern statistical Mechanics*, (Oxford University Press, New York, 1987).

[37] M.A. Allen and D.J. Tildesley, *Computer Simulation of Liquids*, (Oxford Science Press, Oxford, 1987).

[38] D. Frenkel and B. Smit, *Understanding Molecular Simulation, 2nd Ed.*, (Academic Press, New York, 2002).

[39] D. C. Rapaport, *The Art of Molecular Dynamics Simulation*, (Cambridge University Press, New York, 2nd edition, 2004).

[40] B.J. Alder and T.E. Wainwright, J. Chem. Phys. **27**, 1208 (1957).

[41] H. Goldstein, *Classical Mechanics*, (Addison-Wesley, Reading, Massachussetts, 1980).

[42] M.S. Daw and M.I. Baskes, Phys. Rev. Lett. **50**, 1285 (1983).

[43] Murray S. Daw, Stephen M. Foiles, and Michael I. Baskes, Materials Science Reports **9**, 251 (1993).

[44] M Asta and S. M. Foiles, Phys. Rev. B **53**, 2389 (1996).

[45] J.J. Hoyt, J.W. Garvin, E.B Webb III, and M. Asta, Modelling Simul. Mater. Sci. Eng. **11**, 287ł299 (2003).

[46] L.V. Woodcock and K. Singer, Trans. Faraday Soc. **67**, 12 (1971).

[47] H.C. Andersen, J. Chem. Phys **72**, 2384 (1980).

[48] S. Nose, Mol. Phys. **52**, 255 (1984).

[49] S. Nose, J. Chem. Phys. **81**, 511 (1984).

[50] W.G. Hoover, Phys. Rev. A **31**, 1695 (1985).

[51] J.B. Sturgeon and B.B. Laird, J. Chem. Phys. **112**, 3474 (2000).

[52] S.D. Bond, B.J. Leimkuhler, and B.B. Laird, J. Comp. Phys. **151**, 114 (1999).

[53] N. Metropolis, A.W. Rosenbluth, M.N. Rosenbluth, A.H. Teller, and E. Teller, J. Chem. Phys. **21**, 1087 (1953).

[54] D.A. Kofke and E.D. Glandt, Mol. Phys. **64**, 1105 (1988).

[55] A.Z. Panagiotopoulos, Mol. Phys. **61**, 813 (1987).

[56] D.A. Kofke, Mol. Phys. **78**, 1331 (1993).

[57] D.A. Kofke, J. Chem. Phys. **98**, 4149 (1993).

[58] M. Mehta and D.A. Kofke, Chem. Eng. Sci. **49**, 2633 (1994).

[59] M. R. Hitchcock and C. K. Hall, J. Chem. Phys. **110**, 11433 (1999).

[60] M. I. Mendelev H. Nam and D.J. Srolovitz, Phys Rev. B. **75**, 14204 (2007).

[61] J.R. Morris, C.Z. Wang, K.M. Ho, and C.T. Chan, Phys. Rev. B **49**, 3109 (1994).

[62] J.J. Hoyt, B. Sadiqh, M. Asta, and S.M. Foiles, Acta Mater. **47**, 3181 (1999).

[63] J.J. Hoyt and M. Asta, Phys. Rev. B **65**, 214106 (2002).

[64] J.R Morris and X. Song, J.Chem.Phys. **116**, 9352 (2002).

[65] M. J. Gillan D. Alfe and G. D. Price, J. Chem. Phys. **116**, 6170 (2002).

[66] C.K. Hall B.C. Attwood, AIChE J. **50**, 1948 (2004).

[67] C.K. Hall B.C. Attwood, AIChE J. **54**, 1886 (2008).

[68] E. De Miguel and G. Jackson, Mol. Phys. **104**, 3717 (2006).

[69] R.B. Griffiths and J.C. Wheeler, Phys. Rev. A **2**, 1047 (1970).

[70] K.F. Kelton, Solid State Phys. **45**, 75 (1991).

[71] L. Granasy and T. Pusztai, J. Chem. Phys. **117**, 11121 (2002).

[72] A. Karma and W.-J. Rappel, Phys. Rev. E **57**, 4323 (1997).

[73] W.J. Boettinger, S.R. Coriell, A.L. Greer, A. Karma, W. Kurz, M. Rappaz, and R. Trivedi, Acta. Mater. **48**, 43 (2000).

[74] M.E. Glicksman and N.B. Singh, J. Cryst. Growth **98**, 277 (1989).

[75] M. Muschol, D. Liu, and H.Z. Cummins, Phys. Rev. A **46**, 1038 (1992).

[76] J.Q. Broughton and G.H. Gilmer, J. Chem. Phys. **84**, 5749 (1986).

[77] J. Morris, Phys. Rev. B **66**, 144104 (2002).

[78] R.L. Davidchack and B.B. Laird, Phys. Rev. Lett. **85**, 4751 (2000).

[79] R.L. Davidchack and B.B. Laird, Phys. Rev. Lett. **94**, 086102 (2005).

[80] R.L. Davidchack and B.B. Laird, J. Chem. Phys. **118**, 7657 (2003).

[81] J.R Morris and X. Song, J.Chem.Phys. **119**, 3920 (2003).

[82] J.Q. Broughton and G.H. Gilmer, Acta metall. **31**, 845 (1983).

[83] T. Frolov and Y. Mishin, Phys. Rev. B **79**, 045430 (2009).

[84] T. Frolov and Y. Mishin, J. Chem. Phys **131**, 054702 (2009).

[85] B.B. Laird, R.L. Davidchack, Y. Yang, and M. Asta, J. Chem. Phys. 114110 (2009).

[86] Brian B. Laird and Ruslan L. Davidchack, J. Chem. Phys. **132**, 204101 (2010).

[87] J.D. Weeks, D. Chandler, and H.C. Anderson, J. Chem. Phys. **54**, 5237 (1971).

[88] J.P. Hansen and I.R. McDonald, *Theory of Simple Liquids*, (Academic Press, New York, 3rd edition, 2006).

[89] J.W. Gibbs, *The Collected Works*, volume 1, (Yale University Press, New Haven, 1957).

[90] J.W. Cahn. Thermodynamics of solid and fluid surfaces. In W.C. Johnson and J.M. Blakely, editors, *Interfacial Segregation*, 3, ASM International, International Materials Park, OH, 1979.

[91] J. R. Henderson and F. van Swol, Mol. Phys. **51**, 991 (1984).

[92] W.K. Kegel, J. Chem. Phys. **115**, 6538 (2001).

[93] S. Auer and D. Frenkel, Phys. Rev. Lett **91**, 015703 (2003).

[94] M. Heni and H. Loøwen, Phys. Rev. Lett. **85**, 3668 (2000).

[95] W.G. Hoover, M. Ross, K.W. Johnson, D. Henderson, J.A. Barker, and B.C. Brown, J. Chem. Phys. **52**, 4931 (1970).

[96] W.G. Hoover, S.G. Gray, and K.W. Johnson, J. Chem. Phys. **55**, 1128 (1971).

[97] S. Dietrich. Wetting phenomena. In C. Domb and J.L. Liebowitz, editors, *Phase Transitions and Critical Phenomena*, 1, Academic Press, New York, 1988.

[98] J.P. Hansen, Phys. Rev. A **2**, 221 (1970).

[99] J.P. Hansen and I.R. McDonald, *Theory of Simple Liquids*, (Academic Press, New York, 1st edition, 1976).

[100] E. Pereiro-Lopez, W. Ludwig, D. Bellet, P. Cloetens, and C. Lemaigan, Phys. Rev. Lett. **95**, 215501 (2005).

[101] R.L. Davidchack and B.B. Laird, Phys. Rev. E **60**, 3417 (1999).

[102] P. Geysermans, D. Gorse, and V. Pontikis, J. Chem. Phys. **113**, 6382 (2000).

[103] J.J. Hoyt, Phys. Rev. B **76**, 094102 (2007).

[104] G. Bilalbegovic, F. Ercolessi, and E. Tosatti, Europhys. Lett. **17**, 333 (1992).

[105] Steve Plimpton, J. Comput. Phys. **117**, 1 (1995).

[106] W.H. Press, S.A. Teukolsky, W.T. Vetterling, and B.P. Flannery, *Numerical Recipies in Fortran*, (Cambridge University Press,, New York, 1992).

[107] R.L. Davidchack and B.B. Laird, J. Chem. Phys. **108**, 9452 (1998).

[108] D. Buta, M. Asta, and J.J. Hoyt, Phys. Rev. E **78**, 031605 (2008).

[109] T. Frolov and Y. Mishin, Phys. Rev. B. **79**, 045430 (2009).

[110] N.W. Ashcroft and N.D. Mermin, *Solid State Physics*, (CBS Publishing, Hong Kong, 1976).

[111] A. Bolcavage, C.R. Kao, S.-L. Chen, and Y.A. Chang, *Thermodynamic Calculation of Phase Stability Between Copper and Lead-Indium Solder, Applications of Thermodynamics in Synthesis and Processing of Materials*, (Eds. P. Nash and B. Sundman, TMS, Warrendale, PA, 1995).

[112] S. Robert, S. Gauthier, F. Bocquet, S. Rousset, J.L. Duvault, and J. Klein, Surf. Sci. **350**, 136 (1996).

[113] Ch. de Beauvias, Y. Girard, C Perad, B Croset, and B. Mutafschiev, Surf. Sci. **367**, 129 (1996).

[114] E. Vamvakopoulos, D.G. Papageogios, and G.A., Thin Solid Films **485**, 290 (2005) .

[115] R. Sibug-Aga and B.B. Laird, J. Chem. Phys. **116**, 3410 (2002).

[116] R. Sibug-Aga and B.B. Laird, Phys. Rev. B **66**, 410 (2002).

[117] Y. Yang, H. Humadi, D. Buta, B.B. Laird, D. Sun, J. Hoyt and M. Asta Phys. Rev. Lett. accepted (2011).